Abstract

Title of Thesis: A Physics-Based Approach to Characterizing Helicopter
External Noise Radiation from Ground-Based Noise
Measurements

Eric Greenwood, Master of Science, 2008

Thesis Directed by: Senior Research Professor Fredric H. Schmitz
Department of Aerospace Engineering

This thesis describes a new method of characterizing the external noise radiation of a
helicopter suitable for use in the generation of ground noise contours for community land
use planning and assessing the acoustic observability of helicopter flight plans. This work
is an extension of the semi-empirical Rotorcraft Noise Model / Quasi-Static Acoustic
Mapping (RNM/Q-SAM) methodology of characterizing helicopter externally radiated
noise using acoustic radiation hemispheres.   Current methods of interpolation of data on
RNM acoustic radiation spheres are found to lead to high levels of inaccuracy when using
sparse microphone arrays. A new method of interpolation based on the theory of radial

basis functions is developed in this thesis and shown to lead to significantly improved accuracy.

This thesis also extends the RNM/Q-SAM methodology to turning flight conditions. New test procedures are developed for steady turning flight conditions and then used in the acoustic flight testing of the Bell 206B helicopter. The extended RNM/Q-SAM method is applied to the resulting data set in order to generate the first acoustic radiation hemispheres for a helicopter in steady turning flight across a range of flight path angles. The results indicate that the extended Quasi-Static Acoustic Mapping technique is valid for steady turning flight Blade-Vortex Interaction noise. Furthermore, steady turning flight alone is shown not to lead to large increases in externally radiated noise compared to similar straight-line flight conditions. This indicates that high BVI noise levels reported during turns in prior research were most likely caused by transient maneuvers and not turning flight alone.

A Physics-Based Approach to Characterizing Helicopter External Noise Radiation from Ground-Based Noise Measurements

by

Eric Greenwood

Thesis submitted to the Faculty of the Graduate School of the
University of Maryland, College Park in partial fulfillment
of the requirements for the degree of
Master of Science
2008

Advisory Committee:

Senior Research Professor, Fredric H. Schmitz, Chairman/Advisor
Professor, Alison Flatau
Associate Professor, James Baeder

Table of Contents

Contents

List of Symbols

A	area, ft^2
a	speed of sound, ft/s
a_x	longitudinal acceleration, ft/s^2
$a(f)$	atmospheric absorption coefficient, dB/m
C_H	hub force coefficient, $H / \rho A \Omega^2 R^2$
C_T	rotor thrust coefficient, $T / \rho A \Omega^2 R^2$
c_i	radial basis function center location
c_k	weighting coefficient
D_f	fuselage drag force, lbf
F	force, lbf
F_x, F_y, F_z	applied forces along body axes, lbf
f	frequency, Hz
f_{eff}	effective flat plate drag area, ft^2
f_o	observed (Doppler shifted) frequency, Hz
$f_{r,N}$	relaxation frequency of nitrogen, Hz
$f_{r,O}$	relaxation frequency of oxygen, Hz
f_s	sampling frequency, Hz
f_s	source noise frequency, Hz
$f(x)$	target function
Δf	frequency bandwidth, Hz
G	moment, ft-lbf
g	gravitational acceleration, ft/s^2
g_m	m^{th} spherical spline basis

H	hub drag force, lbf
h	angular momentum, lbf-ft-s
h	absolute humidity, kg/m^3
h_r	relative humidity
I	sound intensity, W/m^2
$\mathbb{I}$	identity matrix
i_s, i_r	longitudinal and lateral shaft tilt angles, radians
l	length, ft
M	Mach number, v/a
$M_{s,r}$	Mach number of source along propagation direction
m	particle mass, lbm
M, L, N	pitch, roll, and yaw moments, ft-lbf
N	number of data points
ΔN_i	ground reflection interference correction for ith frequency bin, dB
n_s	surface normal direction
P_m	mth Legendre polynomial
P_{sat}	partial pressure of saturated water, Pa
P_0, P_{01}	reference pressures, Pa
p	acoustic pressure, Pa
p_i	incident wave acoustic pressure, Pa
p_o	acoustic pressure at observer, Pa
p_r	reflected wave acoustic pressure, Pa
p_s	acoustic pressure on hemisphere, Pa
$p(x)$	interpolating polynomial function
p, q, r	rotational rates about body axes, rad/s

Q	rotor torque, ft-lbf
Q	reflection coefficient
Q_i	reflection coefficient of ith frequency bin
R	rotor radius, ft
R	ground resistance, Pa-s/m
r	propagation path, ft
r_o	propagation path to observer, ft
r_r	reflected propagation path to observer, ft
r_s	propagation path to hemisphere, ft
s	turn radius, ft
s_i	incident wave propagation direction
s_r	reflected wave propagation direction
t	time, s
t_o	time of observer, s
t_s	time of noise source, s
T	rotor thrust, lbf
T	atmospheric temperature, K
T_0, T_{01}	reference temperatures, K
V_∞	airspeed, kts or ft/s
v	particle velocity, m/s
v_{CM}	velocity of the center of mass, ft/s
v_h	hover induced velocity, ft/s
v_i	induced velocity, ft/s
v_x, v_y, v_z	drifting frame relative velocities, ft/s
W	weight, lbf

W	preconditioning matrix
$w_{i,j}$	j^{th} weighting factor of the ith cardinal basis
w_x, w_y, w_z	wind velocities, ft/s
x	location of data site, ft
x, y, z	body coordinate axes, ft
X, Y, Z	inertial coordinate axes, ft
X, Y, Z	net longitudinal, lateral, and vertical forces, lbf
Z	complex impedance, Pa-s/m
α_{TPP}	tip-path plane angle of attack, radians
α, β	fuselage angle of attack and sideforce angles, radians
β	number of local interpolating points
β_{1c}, β_{1s}	longitudinal and lateral blade flapping angles, radians
β, μ	random noise correction factors
δ_i	phase of ith frequency bin
ϵ	downwash angle, radians
η	sidewash angle, radians
γ	flight path angle with respect to horizon, radians
γ	spherical reciprocal multi-quadratic shape factor
λ	rotor inflow, ft/s
μ	advance ratio, $v/\Omega R$
σ	flow resistivity, rayls (CGS)
θ_i	incident wave angle relative to surface normal, radians
θ_r	reflected wave angle relative to surface normal, radians

θ, ϕ, ψ	Euler pitch, roll, and yaw angles, radians
θ, ψ	hemisphere elevation and azimuth angles, radians
v_i	radial basis function weighting coefficient
Ω	rotor angular velocity, rad/s
ω_b	body angular velocity, rad/s
ρ	air density, slug/ft^3
$\psi_i(x)$	cardinal basis function
Φ	radial basis function matrix
$\phi(r(\cdot))$	radial basis function
χ	ground reactance, Pa-s/m

Chapter One: Introduction

1.1 Problem Statement

External noise radiation imposes significant limitations on helicopter flight operations. The noise radiated by military helicopters decreases crew survivability by alerting enemies to the presence of military helicopter operations before they are detected visually. Civilian helicopter operations are limited by strict regulation of the allowable noise levels in residential areas designed to reduce community annoyance. Effective mission planning for both civilian and military operations requires knowledge of helicopter noise levels radiated to the ground; however, to date there is no methodology which can accurately predict helicopter noise radiation for the entire range of typical mission profiles.

Aircraft noise levels observed on the ground are predicted through the use of software programs which simulate the noise radiated by the aircraft and its propagation from the aircraft to the ground. These tools can be used to generate ground noise contours (Fig.1) for single or multiple

Figure 1: Typical Ground Noise Contour, RNM [13]

flights following prescribed trajectories across known terrain. The simulated ground noise contours can be used in order to assess the impact of helicopter noise on communities or the acoustic observability of noise over a selected region, and to develop helicopter flight paths which minimize annoyance or the chance of aural detection.
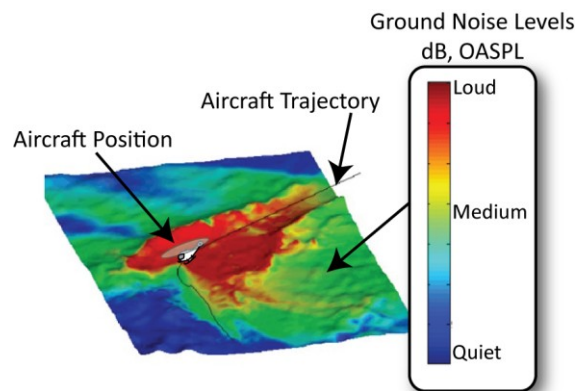
The development of noise contour generation tools requires the construction of two distinct physical models: a noise source characterization model and an atmospheric propagation model. Noise source characterization modeling captures the magnitude and directivity of far-field external noise radiation from the source as a function of the key design and operating parameters of the flight vehicle. This model can be based on theory, experimental measurements, or a combination of both. The resulting noise contours can only be as accurate as the theory or measurements which characterize the source. This thesis focuses on the development of methods which accurately describe the far-field noise radiation of helicopters.

After the noise radiated from the source is described, its propagation from the source to the ground must be modeled in order to generate ground noise contours. In general, the physics of noise propagation through the atmosphere have been closely studied and are well known, especially for typical mid-to-high frequency fixed wing noise sources. However, helicopter noise is somewhat unique in character, containing both lower frequency harmonics as well as mid to high frequency harmonics – moreover, the phasing of some of these harmonics is often tied to the sources of impulsive noise for the rotor, when they occur. In general, low frequency sounds between 20 and 200 Hz are subject to diffraction effects and are affected by the atmosphere, winds, and the terrain – making the propagation of these sounds quite difficult to accurately predict. Mid-to-high-frequency sounds, between 20 and 2000 Hz, are less subject to diffraction and follow well known propagation laws developed for fixed-wing noise sources. While atmospheric propagation modeling is a critical component in the generation of ground noise contours, it is not the focus of this thesis.

1.2 Helicopter Noise Sources

The comprehensive characterization of helicopter noise radiation is quite difficult. Helicopter noise is generated by many different aerodynamic sources, many of which are difficult to estimate. Both the main and tail rotors generate steady loading noise and thickness noise at all times. Other noise sources, such as Blade Vortex Interaction (BVI) noise and High Speed Impulsive (HSI) noise occur only in certain flight conditions, but can be the dominant source of noise where they are present. A chart showing the general pulse shapes, relative frequencies, and magnitudes of the different helicopter noise sources is shown in Figure 2.

Loading noise is generated by periodic application of aerodynamic forces applied by the rotor to the fluid medium – the resulting noise occurs at the blade passing frequency and its higher integer harmonics. Typically the first two harmonics will occur at sub-audible frequencies (below 20 Hz), observed only by electronic detection equipment. Higher harmonics are of lesser magnitude and are generally significant only in the absence of more powerful noise sources. Thickness noise is generated by the displacement of the air by the periodic passage of the rotor blade sections through space. This effect is dominant near the tips of the blades, where the section free-stream velocity is greatest. The resultant noise is observed as a series of strong low-frequency pulses occurring at the blade passage frequency of the rotor. As the tip Mach number is increased, the intensity of thickness noise increases rapidly. The behavior of the pulse changes significantly as the tip Mach number enters the transonic regime – at this point it becomes a dominant source of noise and is termed High Speed Impulsive (HSI) harmonic

noise. HSI noise is dependant not only on the shape of the blade section but also on the

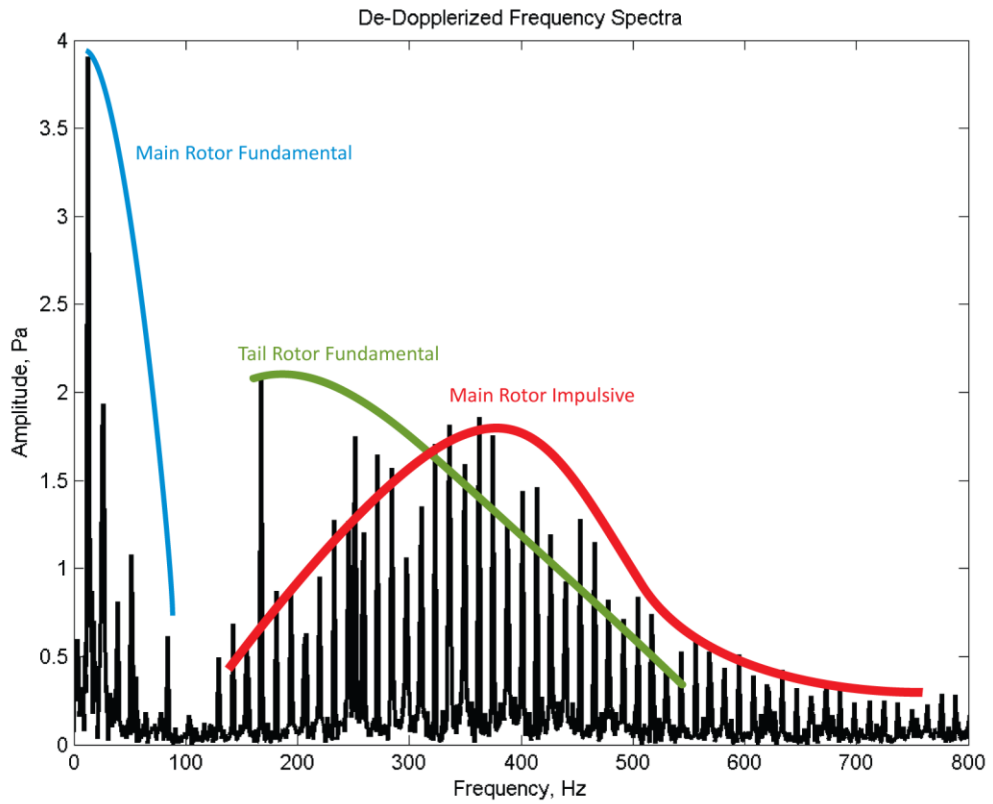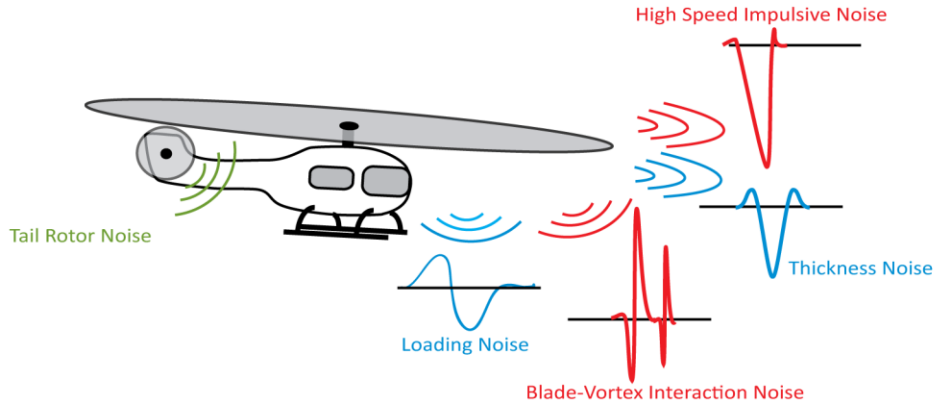transonic flow field surrounding the surface of the airfoil near the blade tip.

Figure 2: Relative Frequencies and Magnitudes of Helicopter Noise Sources

Another important noise source, termed Blade Vortex Interaction (BVI) noise, occurs when the rotor blades pass nearby vortices created and shed from the tip of preceding blades. (Fig. 3) These vortices induce rapid changes in the local angle of attack of the following blades causing rapid changes in rotor airloads.

Figure 3: Isometric View of Helicopter Wake Geometry in Forward Flight, CFD Generated Vorticity Isosurfaces, ONERA elsA [5]

Since loading noise is related to the time-rate-of-change of the forces exerted by the blade on to the medium, a highly impulsive noise results. [2] This condition commonly occurs during moderate speed shallow descents. [3] BVI noise is a particularly important consideration for community land use planning purposes because typical landing approach trajectories incorporate the same shallow descents which lead to high levels of BVI noise.

The final aerodynamic noise source is rotor broadband noise. Broadband noise is produced by the rotor over the mid- to high-frequency range. Such noise is caused by random aerodynamic interactions with the rotor blades generally caused when the rotor blade passes through highly turbulent flow. This turbulence can be caused by boundary layer effects, flow separation, reingestion of the rotor wake, and atmospheric turbulence. This source of noise always exists on the rotor, but is usually only noticeable in operating
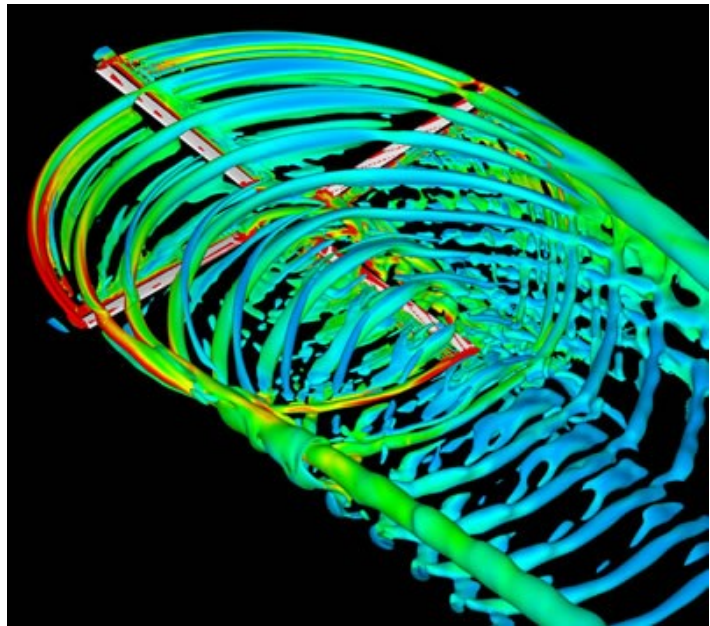
regions where the other rotor noise sources are not dominant – generally, low speed level flight at low rotor Mach numbers.

In addition to the aerodynamic noise sources of the helicopter rotors, noise is generated by the gearbox and engine of the helicopter. However, this noise tends to be of much high frequency than the other helicopter noise sources, and is much more readily absorbed by the atmosphere. As such, mechanical noise has little effect on ground noise contours except at very low altitudes where the distances between source and observer are small.

1.3 Prior Research

Due to the complexity of modeling all of the noise sources of the helicopter, to date there is no comprehensive model of helicopter external noise radiation which is applicable to all flight conditions commonly flown by helicopter pilots during typical operations, for both the civilian and military communities. As a result, accurate noise contours cannot be generated for rotary wing aircraft flying realistic trajectories.
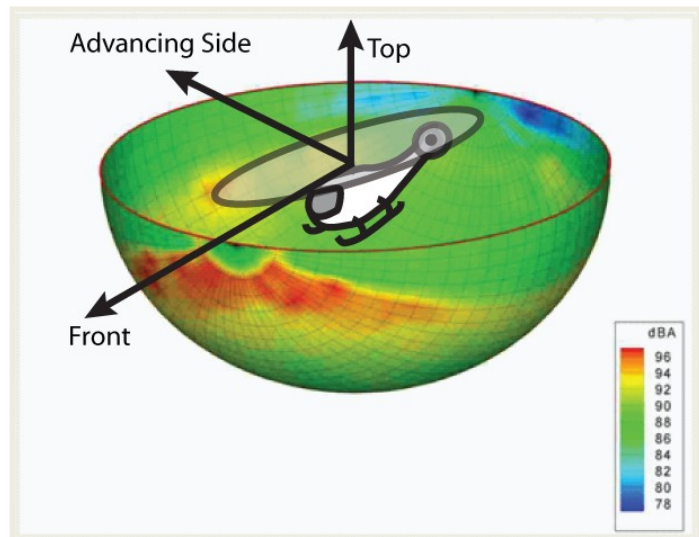
Figure 4: Typical Noise Hemisphere Displaying the Magnitude and Directivity of Emitted Noise

Existing methods of constructing comprehensive source noise models for helicopter can be broadly divided into three categories: theoretical, empirical, and semi-empirical methods. A representative source noise model must capture both the magnitude and directivity of noise radiated from the helicopter. Since the noise propagation will be simulated to the far-field, it is commonly assumed that all noise radiated from the helicopter originates from a single point in space, often fixed to the hub of the moving helicopter. One way to represent the noise radiated from this point source is to present the magnitude and directivity information on the surface of a noise hemisphere affixed to the helicopter but aligned with the local horizon. A typical noise hemisphere is shown in Figure 4. In this figure, noise directed towards the front of the helicopter is shown by the peak levels facing the viewer. Likewise, noise radiating behind the helicopter is illustrated by the low levels facing away from the viewer. Moderate noise levels are observed on the left and right sides of the radiation sphere, as well as underneath, representing noise radiated below the helicopter.

1.3.1 Theoretical Methods

Theoretical methods generally construct this representation of radiated noise by solving the Ffowcs Williams-Hawkins equation to evaluate the noise generated by the rotor as it moves through the medium. Both harmonic and broadband noise sources from the main rotor, tail rotor, and engine must be modeled depending on the helicopter configuration and flight condition. Basic aerodynamic methods, such as blade element theory, are often sufficient to estimate steady harmonic loading noise as well as the thickness noise produced by the main and tail rotor. [1] As discussed previously, in certain flight conditions more complex noise sources may dominate. HSI noise occurs

during high speed flight and is dependent on the transonic flow field near and on the surface of the blades. BVI occurs over a range of flight condition, particularly shallow descents, and requires detailed knowledge of the rotor wake to correctly evaluate both the magnitude and directivity of the resulting noise. Correctly estimating HSI and BVI noise sources is critical, because when they occur they are often the dominant noise source; however, estimating the noise requires the accurate prediction of the aerodynamics on and/or off the surface of the blades.

Computational Fluid Dynamics is often used in Theoretical methods to calculate the flow field about the rotor for analysis of BVI and HSI noise sources; however, due to the complexity of these flow fields such calculations are currently time consuming and inaccurate. Since typical helicopter flight trajectories will pass through a wide range of performance states, these calculations must be repeated many times in order to develop source noise models suitable for the complete range of helicopter maneuvers. Both the DARPA Helicopter Quieting program [4] and ONERA's ARHIS-PARIS method [5] have followed this approach. While such computational models hold promise for predicting helicopter noise without the expense of flight testing full-scale helicopters, they have yet to be realized in practical form for accurate acoustic assessment.

1.3.2 Empirical Methods

Empirical methods employ measurements of the helicopter's radiated noise in order to develop a model of the helicopter as a single noise source. Empirical methods may be thought of as a means of populating the noise hemisphere with measured noise data from ground-based microphones. One of the oldest and most commonly used methods is the Federal Aviation Administration's (FAA) Integrated Noise Model (INM). The INM

method is based on the SAE-AIR-1845 standard for aircraft noise measurement, using a single microphone mounted 1.2 meters above the ground to characterize the aircraft as a noise source. [6] This single microphone flyover method is sketched in Figure 5. This approach is attractive because of its simplicity.
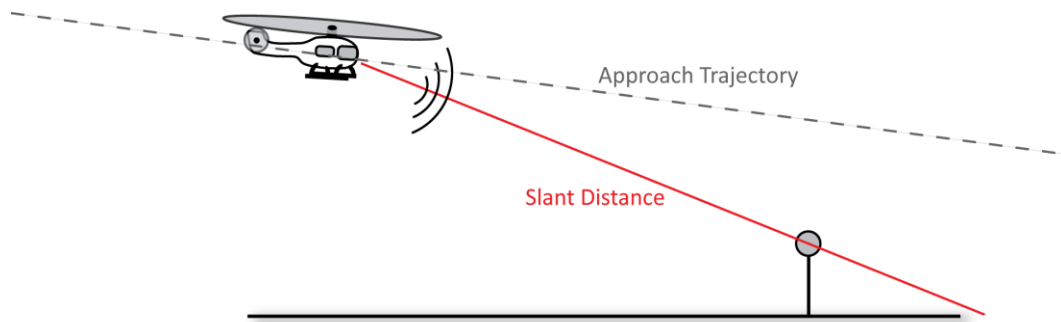

Figure 5: INM Data Collection by SAE-AIR-1845

The aircraft is flown over the microphone along three standardized trajectories representing take-offs, approaches, and cruising flight at a variety of power settings. The recorded acoustic data is combined with tracking data on the aircraft to build a representation of the source. INM models the source as a 1/3 octave frequency spectra that varies as the straight-line propagation, or slant, distance between the source and the receiver changes throughout the flyover. INM does not model the directivity of fixed-wing aircraft explicitly; however the propagation distance implicitly contains information about the variation of noise as a function of elevation angle. For example, at the nearest propagation distance the aircraft is directly above the microphone and at far propagation distances the angle observed at the microphone between the horizon and the aircraft is small. This is sometimes referred to as the Noise-Power-Distance (NPD) representation of the noise source. A chart displaying typical single-microphone NPD data for a fixed-wing turboprop aircraft is shown below, in Figure 6. The observed noise level measured

on the ground is plotted against the slant distance for a variety of power levels. This data is provided using two metrics – the instantaneous peak level measured during each "segment" of the flyover (L_{Amax}, in black) and the averaged Sound Exposure Level (SEL, in blue) for each segment.
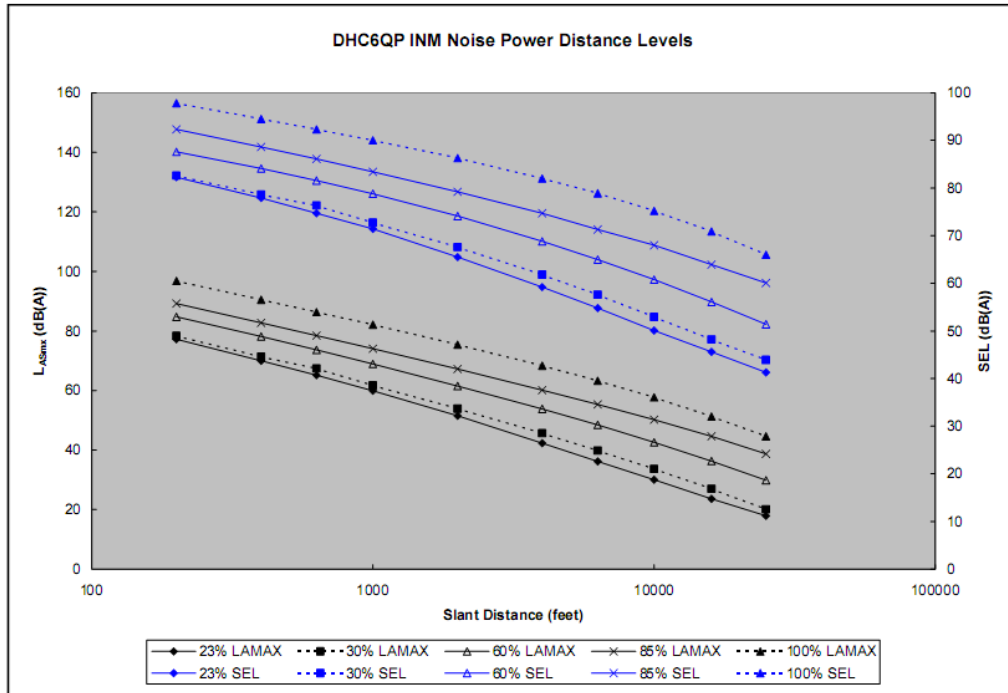
Figure 6: Sample NPD Data for DeHaviland DHC-6 [7]

Recognizing that helicopter noise typically has a strong directivity pattern, the FAA has developed a three microphone testing standard for helicopters, FAA FAR Part 36. This standard adds left and right microphones 150 meters off the flight path in addition to the center microphone. This is analogous to generating an acoustic radiation sphere with three distinct traces of microphone measurements varying by elevation, each representing a different set of azimuths about the source. Newer versions of INM can now accept helicopter noise data which contains directivity data coarsely defined for observers to the

10

left, right, and forward of the helicopter. [7] INM is compatible with ground noise data collected in accordance with current noise certification testing procedures, and therefore a large body of data is available for most aircraft. However, the NPD approach has significant limitations. Three measurement points are insufficient to adequately capture the directivity of helicopter noise. For example, during flight conditions with high BVI noise levels, this noise may be focused over a relatively narrow range of directivity angles and is unlikely to be captured by the three microphone array. Also, the NPD approach broadly classifies helicopter flight conditions into three categories; however, it is known that helicopter BVI and HSI noise is strongly dependant on advancing tip Mach number, advance ratio, main rotor inflow, and main rotor thrust. [8,9,10]   Likewise, INM contains no provisions for assessing the influence of maneuvering flight on the externally radiated noise. Also turning flight cannot be assessed using the INM method because the NPD model links longitudinal directivity to propagation distance – this relation is no longer maintained if the helicopter does not follow a straight-line path over the microphone array.
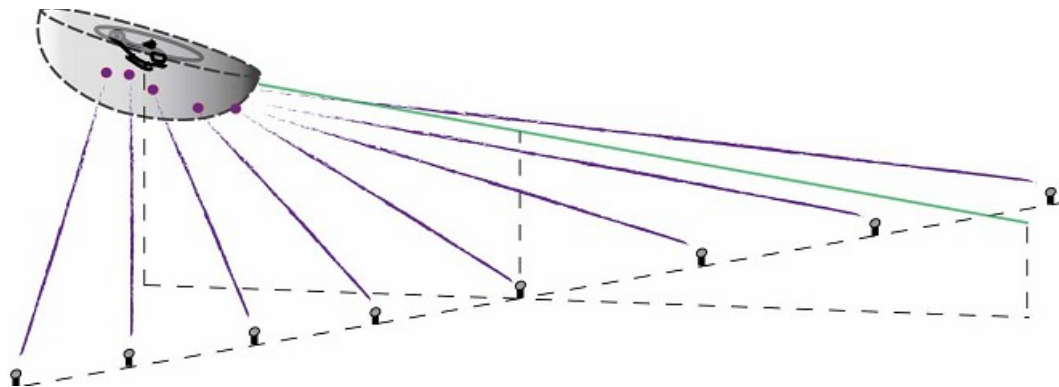

Figure 7: RNM Linear Ground Board Microphone Array

The Rotorcraft Noise Model (RNM) is another, more advanced, methodology for modeling the helicopter using a noise source constructed from empirical flight test data [11]. Ground noise data is collected from a linear array of ground board microphones perpendicular to the flight path. (Fig. 7) If additional data near the horizon is desired (as is useful for long range detection) towers may be set up on both sides of the ground array to make measurements near the plane of the rotor [12]. As the helicopter flies along a steady straight-line trajectory through the array, the directivity angles measured by the individual microphones in the array change from the front of the helicopter to the sides and bottom and finally to the rear. A simple propagation model, including the effects of spherical spreading and atmospheric absorption, is then applied to the measured data in order to calculate the equivalent noise levels at some common distance from the source (typically assumed to be at the helicopter main rotor hub). The result is a set of frequency spectra representing the noise levels that would be measured on the surface of a hemisphere fixed to the helicopter with a scattered distribution of directivity angles. Each microphone in the array will trace an arc of measurements across the hemispherical surface, from the front of the hemisphere towards the rear. This scattered data must then be interpolated to a regular grid of directivity angles on the surface of the hemisphere for visual display of the hemisphere and for use in noise propagation simulation for the generation of ground noise contours [13].

Accurately interpolating scattered data across the surface of a hemisphere is a significant challenge – conventional techniques, including those used by RNM, are developed from planar interpolation schemes for scattered data and result in distortions of the directivity pattern described by the hemisphere. As the number of microphones

composing the array is reduced, the distribution of data points on the sphere becomes

sparser and interpolation inaccuracy increases. (Fig. 8)

Modern interpolation techniques have been developed for accurate interpolation of

scattered data on spherical surfaces [14]; however due to stability problems with large

datasets practical application has largely been restricted to the field of geodesy, where

sparse measurements taken by satellites in orbit are interpolated over the surface of the

earth. [15] RNM requires many more data points on the surface of the sphere than the

geodesy problem – in order to accurately
construct a helicopter noise source from
measured data, an improved interpolation
technique must be introduced which can
reliably converge to produce an
accurate approximation of the radiated
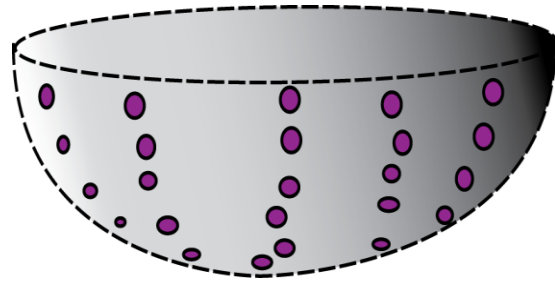noise across the entire sphere.

Figure 8: Scattered Data on Hemispherical Surface

In general, several measurements are made for each helicopter through a range of

flight conditions in order to construct a set of acoustic hemispheres. RNM classifies the

acoustic hemispheres in this set by weight, airspeed, and flight path angle. For straight-

line steady flight conditions, it is known that these parameters are related to the thrust, tip

Mach number, advance ratio, and inflow for a helicopter flying in known atmospheric

conditions. Although Rotorcraft Noise Model provides a more sophisticated method of

characterizing the externally radiated noise of helicopters than INM it is still only

applicable to steady straight-line flight. Turning flight directivity patterns can be

mimicked by tilting the acoustic hemisphere of the helicopter flying the same airspeed

13

and flight path angle by the bank angle of the turn – however, this geometric rotation fails to account for the effect of the turn on the performance and acoustic state of the vehicle and has not been proven to be an accurate representation of the helicopter noise source during turning flight.

Qinetiq's Helicopter Acoustic Measurement System for Trials and Experimental Reduction (HAMSTER) method is very similar to the RNM methodology. [16] However, the microphone towers are constructed as vertical beamforming arrays, containing 40-50 microphones with several different vertical spacings. An autocorrelation routine is performed on the microphones composing the beamforming arrays in order to identify the noise radiated directly from the helicopter, but reject uncorrelated noise reflected off the ground and measured by the array. Ground reflections can interfere significantly with microphones mounted above the ground, especially those mounted at higher points on the tower. [17] The beamforming technique only works on a limited range of pre-selected frequencies governed by the spacing of the microphones composing the vertical arrays. The beamforming approach also imposes an additional limitation on propagation distance – only measurements between 200 m and 450 m are considered valid.
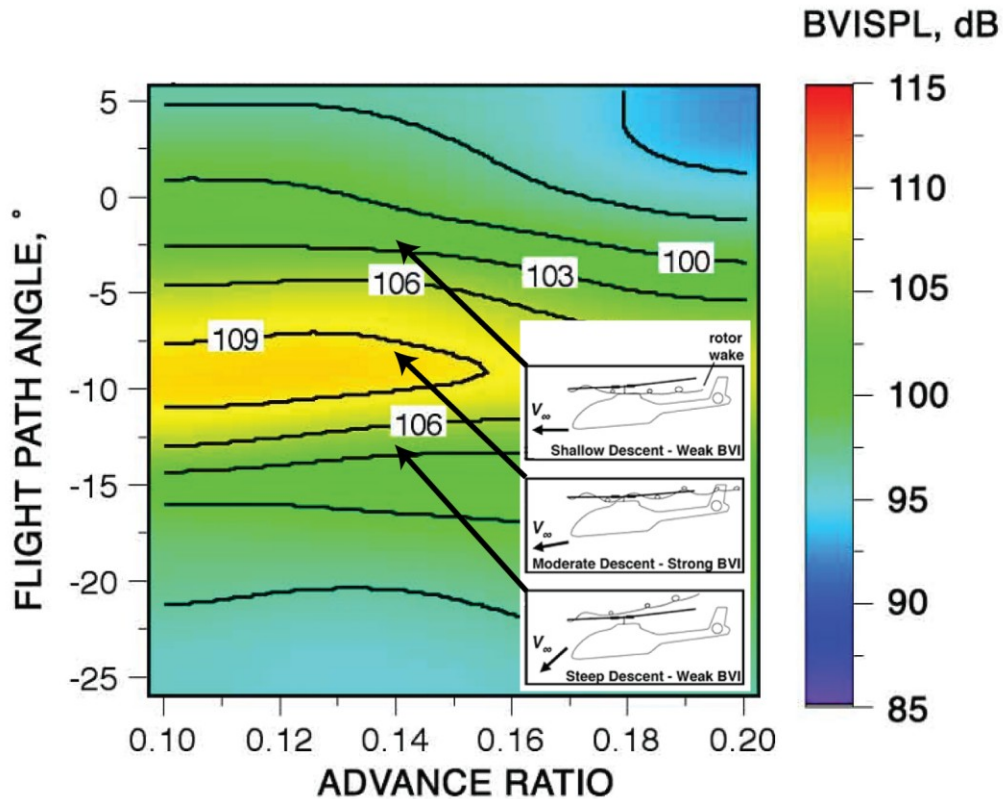
Figure 9: Variation in BVI Noise Levels Measured from an In-Flight Microphone Array Attached to Bell 206B by Flight Path Angle and Advance Ratio. Microphone on Array is Located Underneath Rotor Advancing Tip, as in Section 4.1.1 [57]

1.3.3 Semi-Empirical Methods

A third approach is to expand the RNM concept by combining it with theoretical analysis in order to describe how noise radiation will change in response to changes in flight condition. The Rotorcraft Noise Model has been successfully combined with the Quasi-Static Acoustic Mapping (Q-SAM) method [18,19] to produce the hybrid RNM/Q-SAM methodology for BVI noise – which is typically dominant during approach. The Q-SAM method applies momentum theory to estimate the overall inflow of the rotor based on knowledge of the helicopter drag, flight path angle, and longitudinal acceleration. The overall inflow can be related to the BVI noise state – when inflow is

near zero the wake stays near the rotor and BVI noise will be high, when the inflow is highly positive or negative the wake will move far from the rotor and BVI will not occur. (Fig. 9) The RNM/Q-SAM method allows RNM to classify hemispheres using the Q-SAM relation, allowing RNM/Q-SAM to use a limited set of flight test data to characterize a range of flight conditions with similar acoustic states. This extends the applicability of RNM to include moderate accelerations and decelerations along a straight-line path. RNM/Q-SAM is the most sophisticated semi-empirical approach to comprehensively modeling helicopter externally radiated noise; However in its current state of development it is still lacking the capability to analyze general maneuvering flight.

Other research has reported increased noise during turning flight [20]. However, the key parameters which affect turning flight noise have not been isolated and quantified. Some recent analytical studies of aggressive turning maneuvers have indicated very large increases (as much as 40 dB) in noise levels. [21] However, these studies have treated the entire turn as a single dynamic maneuver – moderate steady turns have not been thoroughly investigated. As such, turning flight noise is not yet well understood and has not been rigorously incorporated into any rotorcraft noise estimation models. In other turning flight noise research [22], turning flight noise was captured in high winds and unsteady conditions – gross trends were recorded, but a cause and effect relationship could not be established. A stronger understanding of the effects turning flight has on helicopter noise must be developed in order to provide accurate helicopter noise radiation models for practical applications.

1.4 Thesis Objectives

This thesis seeks to develop a more accurate and useful characterization of helicopter source noise for the generation of ground noise contours. The RNM/Q-SAM methodology is currently the most sophisticated approach; however, the accuracy of the method is limited by difficulties in interpolating noise data over the acoustic radiation spheres. In addition, the RNM/Q-SAM methodology is only applicable to straight-line flight whereas real-world helicopter flight operations include turning flight maneuvers. The main objectives of this thesis are therefore to develop an improved method of interpolating acoustic data over radiation spheres and to extend the RNM/Q-SAM methodology to turning flight.

In Chapter Two, the existing RNM/Q-SAM approach is described for straight-line flight. Following in Chapter Three, the interpolation problem is addressed by reviewing existing interpolation schemes and then developing a new interpolation method to minimize interpolation error. This new method is shown to provide a significant improvement to the smoothness of acoustic hemispheres for straight-line flight. Chapter Four describes the acoustic flight testing of the Bell 206B helicopter using the method described in Chapter Two, and presents ground noise hemispheres produced using the new interpolation scheme. Chapter Five extends the RNM/Q-SAM method with enhanced interpolation to steady turning flight, and presents the results of flight testing the Bell 206B helicopter following the procedures introduced in this chapter. Chapter Six summarizes the conclusions of this thesis and Chapter Seven provides recommendations for future work.

Chapter Two: RNM Noise Hemispheres

2.1 General Methodology

The Rotorcraft Noise Model (RNM) methodology provides a means to produce a representation of the external noise radiation of a helicopter during a steady flight condition, in terms of both magnitude and directivity, from ground-based acoustic measurements of the noise observed during a steady-state flyover the helicopter. [24] The magnitude and directivity information of the external noise of the helicopter can then be utilized to characterize the noise emitted by various sources on the helicopter or can be used in sequence with data for a range of flight conditions to simulate the noise propagated to the ground for more complex trajectories.
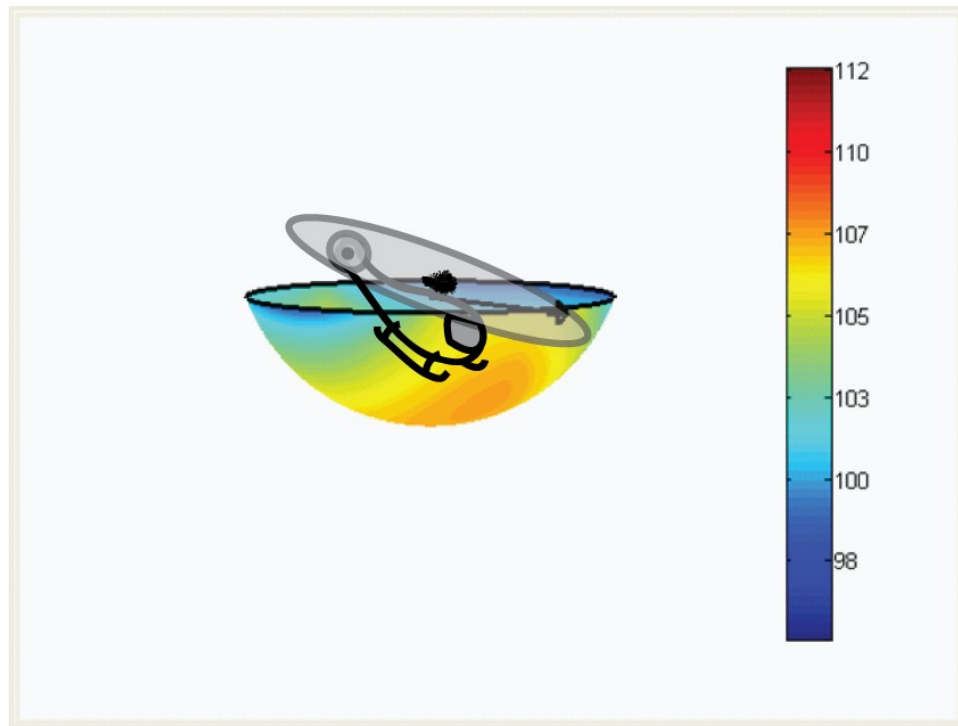

Figure 10: Isometric View of an Acoustic Radiation Sphere, Bell 206B @ 60 kts, 6 Degree Descent, BVISPL

RNM represents the magnitude and directivity of the noise emitted by the helicopter as sound pressure levels (SPL) which are mapped to a hemispherical surface an arbitrary radius away from the helicopter position. (Figure 10) In this thesis, the Blade-Vortex Interaction Sound Pressure Level (BVISPL) metric will be used, which includes only the noise radiated at frequencies between the 6th and 40th harmonics of the main rotor blade passing frequency and does not apply any frequency weighted correction to the noise levels. This metric assess the mid-frequency range associated with BVI noise, but also includes strong contributions from the tail rotor blade passing frequency and its harmonics in most conventional helicopters. The acoustic hemisphere concept makes the assumption that the helicopter may be represented as a compact source, occupying a single point in space but distinct from an omnidirectional point source in that the magnitude of radiated noise varies with direction. Since the propagation distances in both the measurement and simulation of the spheres are much larger than the distance between individual acoustic sources on the helicopter, the error in directivity due to the compact source assumption is small. Additionally, since the noise measurements used to compose the sphere are made from distances much larger than the diameters of the main and tail rotors, no near-field pressure data is captured by the microphones and therefore the hemispheres are only valid for far-field noise, no matter how small of a radius is chosen for the arbitrary hemisphere.

2.2 Hemisphere Selection
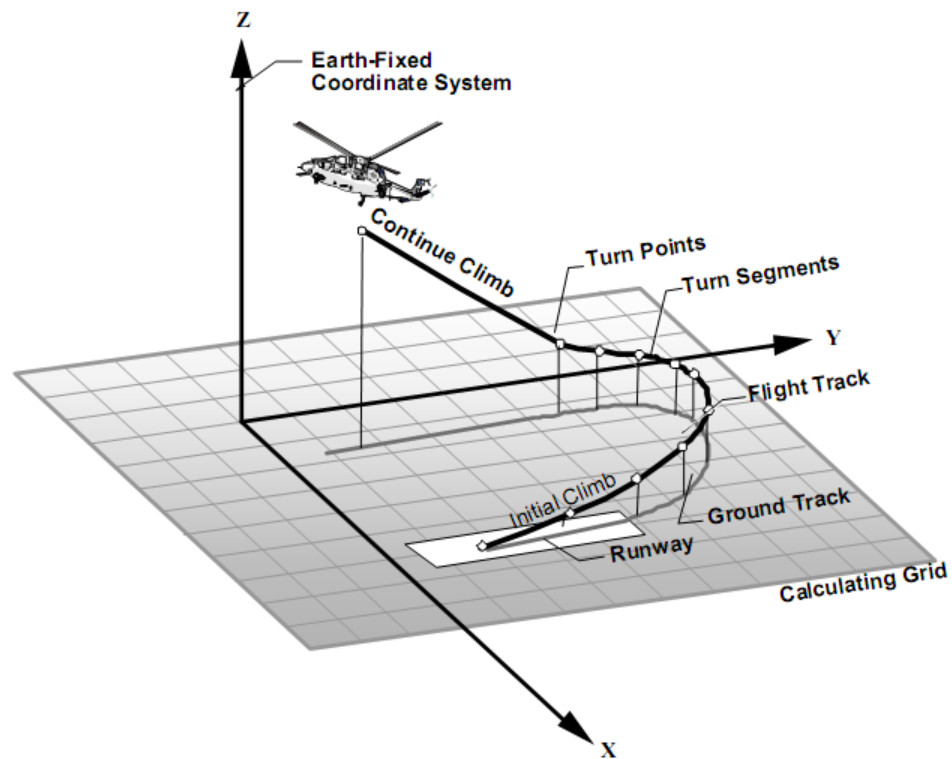
2.2.1 Hemisphere Selection in RNM

Figure 11: Division of Flight Trajectory into Straight-Line Segments in RNM [13]

Each acoustic radiation hemisphere describes the external noise radiation of the helicopter for a single steady-state flight condition. In order to accurately simulate the noise radiation of a helicopter as it flies through an arbitrary trajectory multiple hemispheres, each representing a different flight condition, must be employed. The simulated trajectory is segmented into steady straight-line flight segments, each of which is then associated with a corresponding acoustic hemisphere. (Fig. 11) Ground noise levels are calculated by simulating the propagation of noise from the acoustic radiation sphere to the ground as the source travels along each straight-line flight segment. The

additional noise that might be radiated by the helicopter due to transitions between straight-line flight segments is neglected.

Blade-Vortex Interaction noise is particularly sensitive to the flight condition and dominates in the moderate speed descending flight regime. As the helicopter descent angle increases from level flight at a moderate airspeed, BVI noise increases dramatically then reduces as illustrated in Figure 12. As discussed previously, descending flight first causes the wake of the main rotor system to pass in close proximity to the tip-path-plane of the helicopter, causing increases in high frequency blade air-loads and resulting in strong BVI noise. Further increases in descent angle eventually increase the separation distance between the wake and the rotor tip-path-plane causing the BVI noise to be reduced.
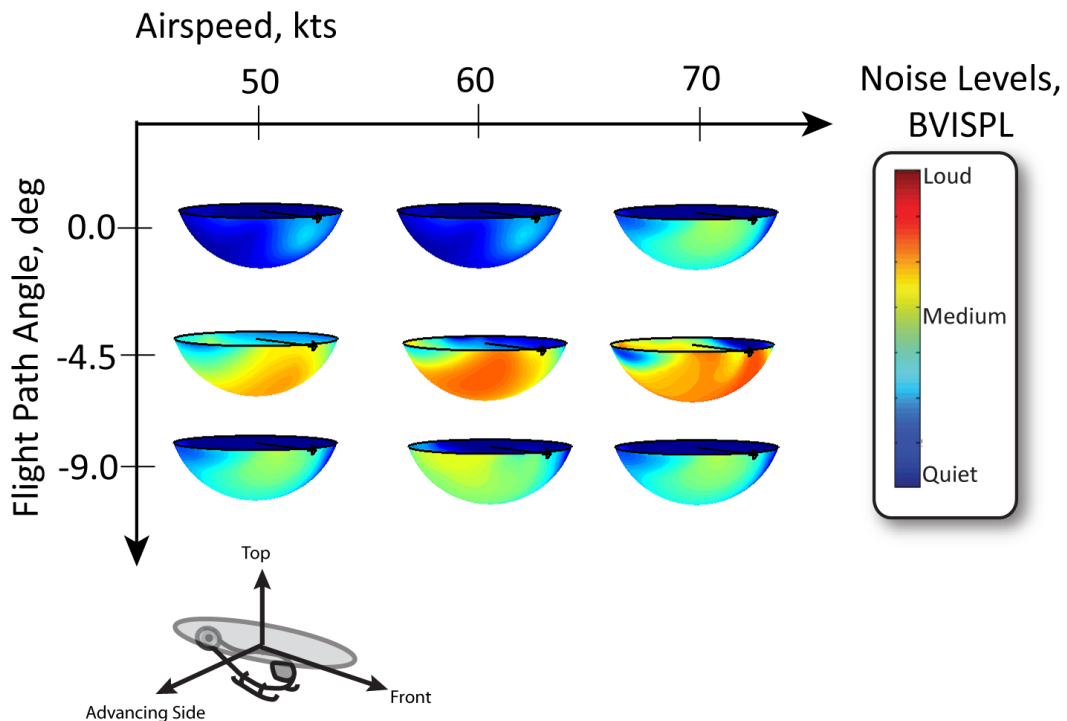

Figure 12: RNM Hemisphere Selection by Dimensional Parameters (Representative Noise Spheres)

Acoustic hemispheres in RNM are captured and classified by discrete values of two parameters, descent angle and airspeed, as shown in Figure 12. As a result there exist only a finite number of acoustic hemispheres for any particular helicopter. In a case where no acoustic hemisphere matches closely with the flight segment being simulated, a new hemisphere may be generated by first linearly interpolating noise levels on the sphere between the two acoustic hemispheres associated with the most similar airspeeds and if necessary this is followed by interpolating between spheres with the most similar flight path angles. For straight-line segments representing portions of a turn, RNM simply rotates the directivity of the acoustic hemisphere by the helicopter bank angle.

2.2.2 Governing Non-Dimensional Parameters for BVI Noise

Theoretical and experimental studies have shown that BVI is controlled by four non-dimensional factors: rotor hover tip Mach number, rotor thrust coefficient, rotor inflow, and rotor advance ratio. For quasi-steady flight conditions with constant rotor RPM and atmospheric conditions, hover tip Mach number and rotor thrust coefficient will often remain constant leaving BVI noise dependant on the distance between the main rotor shed wake system and the rotor blades and the main rotor advance ratio. With constant rotor RPM, the advance ratio will vary directly with airspeed. However,
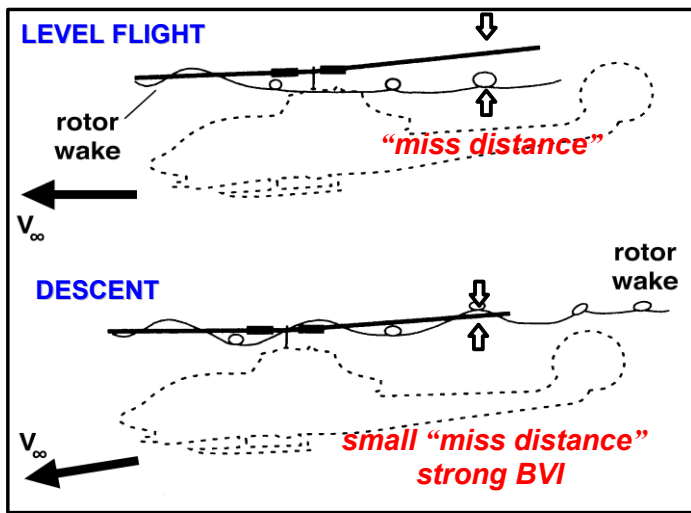
Figure 13: Longitudinal BVI Geometry - Rotor/Wake "Miss Distance"

evaluation of the rotor inflow is dependent on more than just the flight path angle.

A straightforward and simple way to express this dependence is through the use of rotor momentum theory. It is assumed that the distance between the rotor wake system and the following rotor blades is proportional to the inflow through the rotor. (Fig. 13)

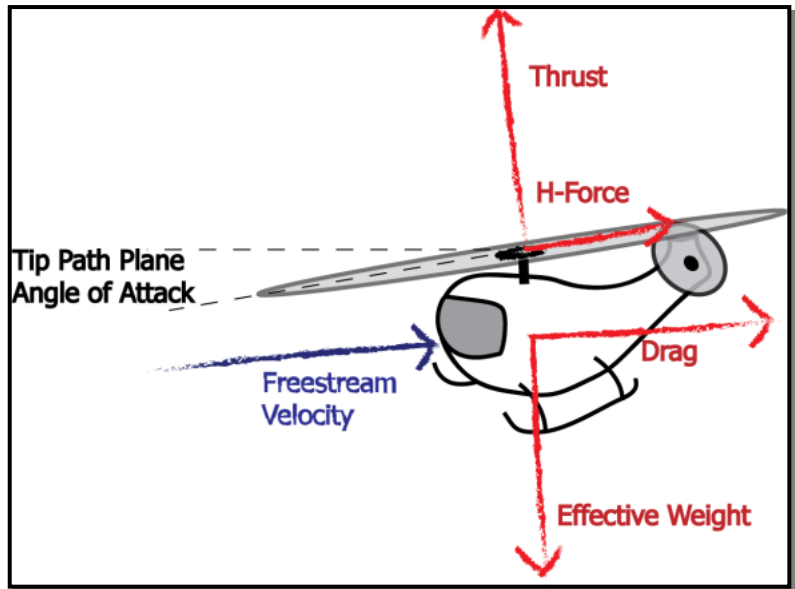During straight and level flight, inflow through the rotor system is high, and the wake is expected to be far below the rotor. The large

Figure 14: Longitudinal Force Balance

distance between the wake and the rotor yields weak blade-vortex interactions and thereby low BVI noise. As the helicopter enters moderate descent rates, the inflow through the rotor system decreases and the wake moves closes to the rotor tip-path-plane leading to increased BVI noise. When the descent rate becomes high enough, the net inflow approaches zero and the wake no longer convects out of the plane of the rotor leading to a maximum BVI noise condition. If the descent rate is increased further still, the inflow state becomes negative, and the wake lies above the rotor, increasing the "miss distance", and reducing noise. This relation can be seen analytically by considering the results of a simple momentum theory analysis of the helicopter in forward flight. The

simple momentum theory quartic, non-dimensionalized by the hover induced velocity can be expressed as:

$$\bar{v}_i^4 - 2\bar{V}_\infty \bar{v}_i^3 \sin \alpha_{TPP} + \bar{V}_\infty^2 \bar{v}_i^2 + 1 = 0 \qquad (1)$$

The quartic expression for induced velocity may be solved numerically, as a bi-quadratic expression by making the "high speed" assumption (valid only for $\bar{v}_i > 2$) that the tip-path-plane angle of attack equal to zero, or as a Taylor series expansion in tip-path-plane angle of attack about the bi-quadratic solution, as shown in Appendix A.

An expression for the tip-path-plane angle of attack can be found by solving a longitudinal force balance for the helicopter. (Fig. 14) When main rotor thrust is set equal to gross weight, this results in the following simplified expression for no-wind conditions:

$$\alpha_{TPP} = \frac{-D_f}{W} - \gamma \qquad (2)$$

Figure 15 shows the results of this inflow calculation for the Bell 206B helicopter evaluated in this thesis as a function of forward flight speed for a range of flight path angles.
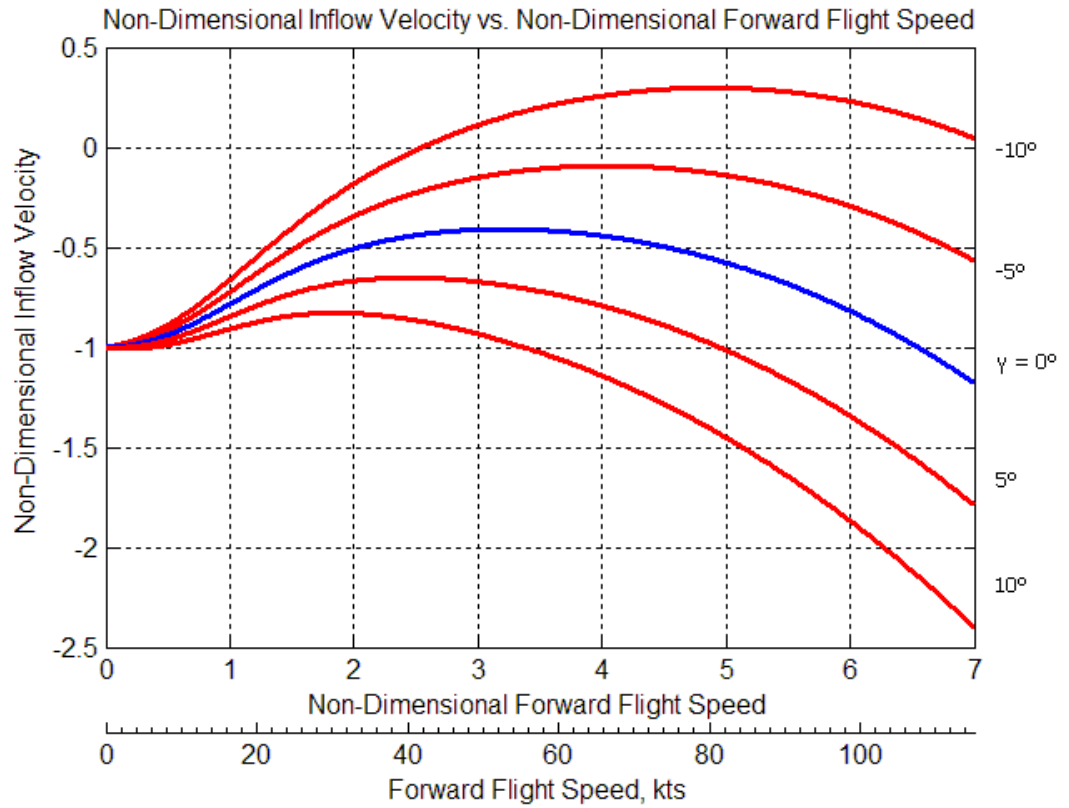
Figure 15: Variation in Non-Dimensional Inflow by Airspeed for Bell 206B as Configured in 2007 Flight Test, See Section 4.1.2 for Configuration Details

A more detailed derivation of these equations may be found in Appendix A.

2.2.3 RNM/Q-SAM

The Quasi-Static Acoustic Mapping (Q-SAM) method, developed at the University of Maryland, extends the momentum theory inflow estimate to quasi-static longitudinal accelerations and relates the inflow state of the main rotor to its acoustic state to form equivalences between steady state flight and moderate straight-line flight maneuvers. Currently Q-SAM is applicable to accelerating and decelerating, descending and level flight BVI noise. [56]

Consider again the longitudinal force balance of the helicopter, however this time a steady longitudinal acceleration is included. This results in a new expression for the tip-path-plane angle of attack:

$$\alpha_{TPP} = \frac{-D_f}{W} - \gamma - \frac{1}{g}a_x \qquad (3)$$

The expression for tip-path-plane angle of attack is again used to calculate the overall inflow through the main rotor in forward flight. From the tip-path-plane angle of attack expression, it is readily apparent that various combinations of descent angle, drag force, and longitudinal acceleration/deceleration may yield the same tip-path-plane angle of attack and thereby inflow. It is therefore possible to make equivalences between different flight conditions which result in the same overall inflow, in addition to advance ratio, rotor tip Mach number, and thrust coefficient.
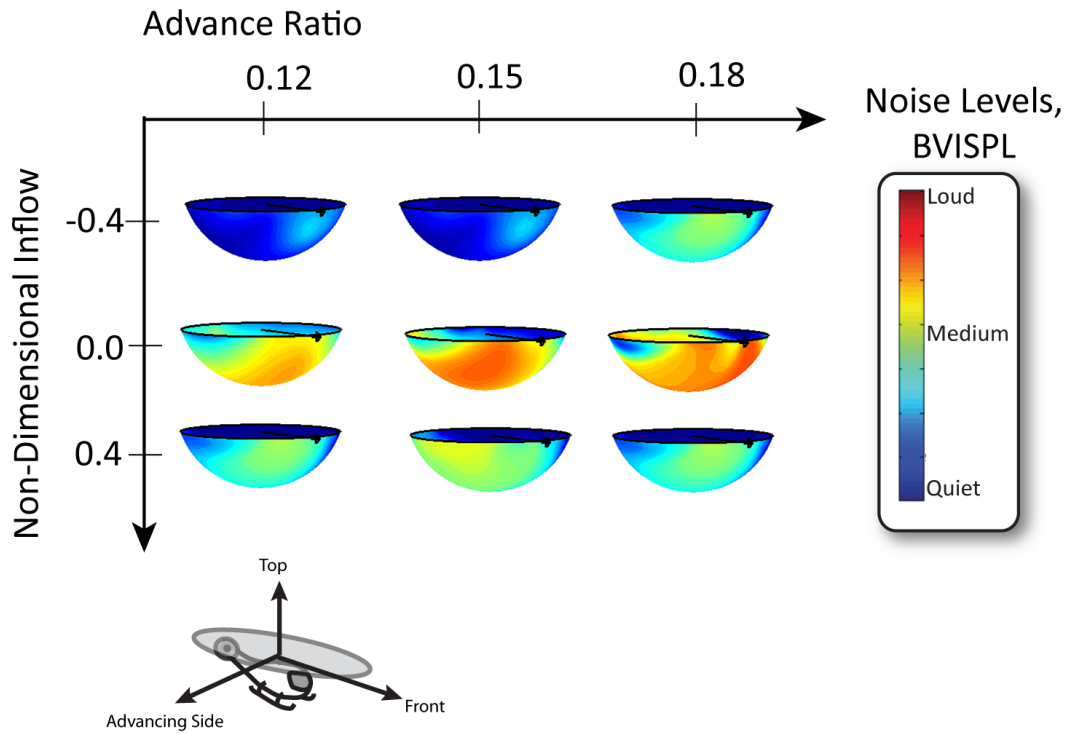
Figure 16: Hemisphere Selection by Non-Dimensional Parameters, RNM/Q-SAM

The Q-SAM method provides a theory for selecting acoustic radiation spheres for use in RNM. Instead of selecting hemispheres by the dimensional parameters of airspeed and flight path angle, acoustic hemisphere selection is determined by two of the non-dimensional parameters which govern BVI noise, inflow and advance ratio. (Figure 16) For each simulated straight-line flight segment, these two non-dimensional parameters are calculated and a matching acoustic hemisphere selected. Straight-line flight trajectory segments must keep these parameters steady, however may now include quasi-static maneuvers, such as constant accelerations or decelerations, or the use of drag-modifying devices like spoilers, flaps, or retractable landing gear in addition to descending or ascending flight. By associating the BVI noise with the non-dimensional governing parameters, the same matrix of hemispheres of different airspeeds and flight path angles

normally used by RNM may be applied to an expanded range of straight-line flight maneuvers maintaining steady inflow and advance ratios.

2.3 Presentation of Acoustic Radiation Hemispheres

2.3.1 Coordinate Systems

The local coordinate system of the noise hemisphere can be defined in two ways, horizon-fixed and rotor tip-path-plane fixed.   In the rotor tip-path-plane fixed method, the hemisphere coordinates are aligned with the plane of the main rotor. This is a physically meaningful way of defining the acoustic hemispheres because the magnitude of noise generated by all of the rotor noise sources varies by the orientation of the observer with respect to the rotor plane. However, defining a hemisphere using this coordinate system requires knowledge of the tip-path-plane orientation with respect to the ground while constructing the hemisphere from ground based microphone measurement and while simulating the propagation of noise from the helicopter to the ground for construction of ground noise contours. Doing so requires either direct measurement of tip-path-plane orientation or applying the force balance relations in order to estimate the orientation of the tip-path-plane from knowledge of the helicopter performance state, gross weight, and drag.

Horizon-fixed acoustic hemispheres are currently used by RNM.   In this case the orientation of the helicopter's main rotor is ignored, and measurements are mapped to a hemisphere fixed to the horizon. The advantage of this method is that the orientation of the helicopter need not be measured nor calculated. In addition, since the microphone array is located on the ground, all noise measurements are made relative to the horizon.

28

Likewise, simulated noise propagation from the hemisphere will involve only data which lies below the plane of the horizon.

In either case, a hemisphere constructed in one coordinate system may be transformed to the other through a simple rotation. In this thesis, hemispheres will be displayed using horizon-fixed coordinates for simplicity and consistency with the existing RNM method. Since in this thesis only the flight path and bank angles are varied between the tested straight-line and turning-flight flight conditions, each flight test condition represents a distinct combination of the non-dimensional governing parameters for BVI noise and no acoustic equivalences may be made. However, for use in generating noise contours with the RNM/Q-SAM methodology, these hemispheres must be associated with the tip-path-plane orientation of the rotor because it is possible for two states with equivalent BVI noise to have different orientations of the tip-path-plane with respect to the horizon, and hence a different orientation of the radiated noise directivity. Figure 17 illustrates one such case, where the helicopter will have the same tip-path-plane angle of attack (and thereby main rotor inflow) while undergoing a moderate forward acceleration in level flight as when in a non-accelerating moderate climbing flight condition; yet the two Q-SAM equivalent flight conditions have a different orientation of the tip-path-plane with respect to the horizon.
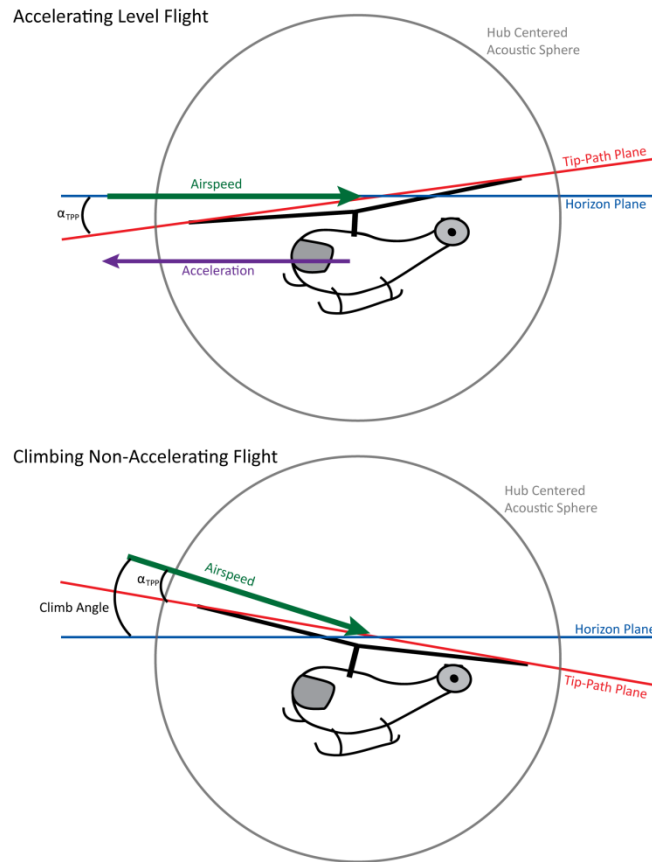
Figure 17: Change in Tip-Path Plane Orientation with Respect to the Horizon for Two Cases with the Same Tip-Path Plane Angle of Attack, Accelerating Flight (Top) and Climbing Flight (Below)

2.3.2 Hemispherical Projections

Three-dimensional images of hemispheres are unable to show the noise levels across the entire surface of the sphere without employing multiple views. In order to display the hemisphere in its entirety on a single plot, it is necessary to project the hemisphere onto a 2D planar surface. There is no standard method of projecting RNM hemispheres since RNM is most frequently applied to generate ground noise contours without close examination of the intermediate acoustic radiation spheres.

No 2D projection of a spherical surface can be free of distortion, as Euler proved in 1777. [25] Such a projection can either be conformal or equal-area, but never both. A

conformal projection preserves the shape of features, since at each point the angles between the spherical surface coordinates are locally preserved in the flat coordinate system. However, the relative size of features will be changed globally during the transformation.   An equal-area projection ensures that each region of the map will retain the same area in the flat coordinate system as it had on the spherical surface – however, the orientation of points with respect to each other within any region will be changed, distorting the shape of each feature. In order to effectively display all of the information captured by a hemisphere, some sort of projection to a flat 2D figure must be employed.

In this paper, hemispheres are displayed mapped to a 2D image using a Lambert Conformal Conic projection, developed and used commonly by cartographers to accurately display maps of polar regions. [26]   The Lambert projection is perfectly conformal, but is also fairly close to being equal-area when no more than one half of a sphere is transformed at once.   This is achieved by "splitting" the back end of the hemisphere along the 0 degree azimuth angle, and "unrolling" the resulting cone to a 2D projection. (Figure 18)   The top of the projection represents the angle directly in front of the helicopter, the split seam the angle directly behind, the right side the advancing side of the helicopter, and the left the retreating side. The center of the projection, at 90 degrees elevation, represents the bottom of the hemisphere. The radial lines thus represent the azimuth angles, and the concentric lines the elevation angles. This projection allows for an intuitive understanding of the directivity patterns of externally radiated noise.
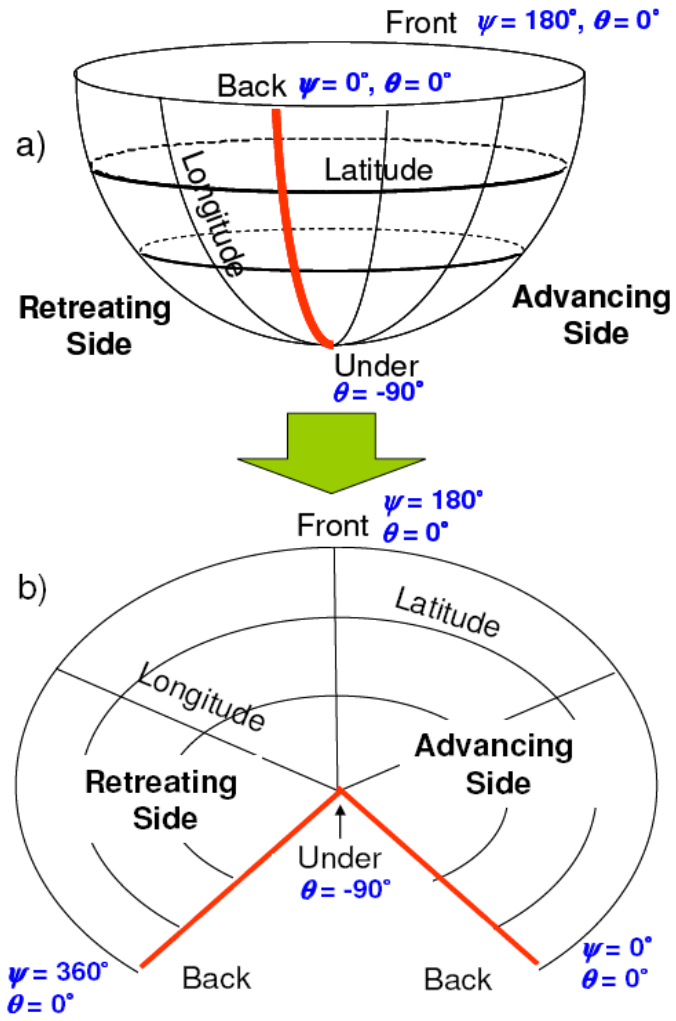
Figure 18: Lambert Conformal Conic Projection
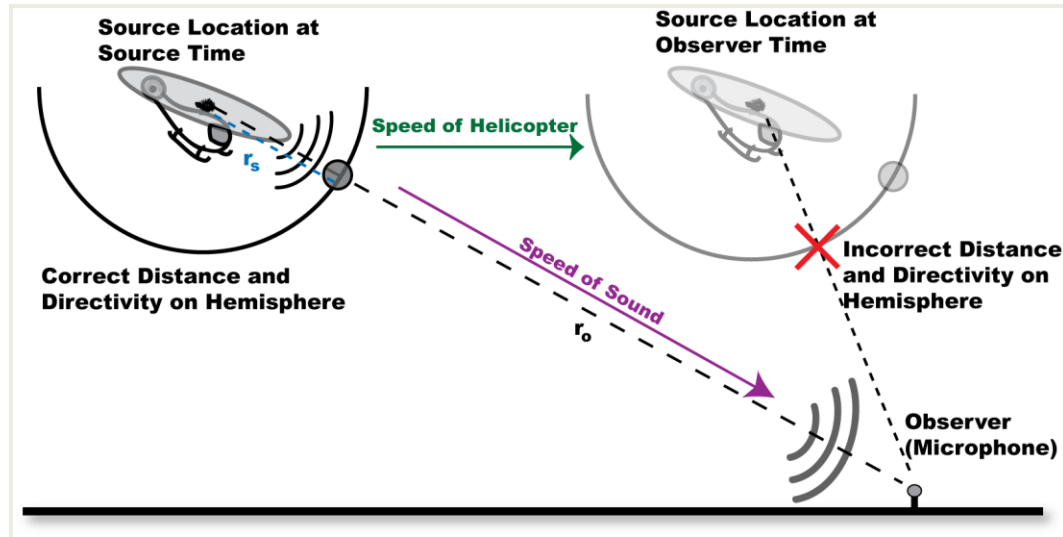
2.4 Construction of a Hemisphere

Figure 19: Evaluation of Retarded Time, r_s is propagation distance from source to sphere, and r_o from source to observer

In this thesis, a source time reference is used in mapping the acoustics measured at the ground onto the arbitrary hemisphere formed about the helicopter. For each known position of the helicopter on its flight trajectory, the geometric relationships between the helicopter and each microphone on the array are calculated to provide the angular location on the hemisphere from which the emitted noise is being measured, as well as the distance between the helicopter and the microphone at that instant in time. In this thesis, the main rotor hub is taken as the center of the hemisphere and is assumed to be the point from which all far-field noise is radiated. The surface of this hemisphere is chosen to be 30 ft from this point, or approximately twice the rotor radius, and represents a measurement of the far-field noise emitted from the assumed hub point source relatively close to the helicopter. The measurement of the distance between the point source at the hub and the microphone is then used, along with the atmospheric speed of

sound calculated from local humidity and temperature data, to compute the time at which the noise emitted by the conceptual point source at each position on the flight track is received by each microphone on the array using the standard retarded time formulation:

$$t_o = t_s + \frac{r_o}{a} \qquad (4)$$

Now knowing the correct time of observation for each microphone associated with a known directivity from the compact source, it is possible to supply a short window of pressure time history data associated with every measured point on the hemisphere. (Figure 19)

The data in this time window can then be processed with a Fast Fourier Transform (FFT) in order to extract information about the radiated noise in the frequency domain. Since the FFT process assumes periodicity of the signal, the time window should be selected to be approximately a multiple of the blade passage frequency of the helicopter main rotor, in order to minimize "leakage" across the narrowband frequency spectra. The tail rotor is always operated at a non-integer multiple of the main rotor frequency, however since there are many more blade passages of the tail rotor in a given time window than there are for the main rotor, the frequency leakage will not be as significant in the higher frequency range of the tail rotor. Additionally, total length of the time window is important to consider. A long time window, containing many blade passages, will lead to better frequency resolution as the number of acoustic pressure samples is increased. The width of each frequency bin is given by:

$$\Delta f = \frac{f_s}{N} = \frac{1}{t} \qquad (5)$$

However, the ground based microphones measure noise which is varying in directivity over time. When the helicopter is far away from the array, this variation in angle happens slowly. However, as the helicopter passes over the array, the variation occurs quickly. As the length of the window is increased, the assumption that the pressure data in that window corresponds to a single point on the sphere becomes less valid. In this case, a typical one second time window centered about the calculated observer time has been selected, corresponding to 1 Hz bandwidth. At a minimum height above ground of 492 ft, this yields an angular window of approximately ten degrees for a helicopter traveling at 60 kts passing directly over the array.

The next step in the process is to correct the amplitudes of each of the acoustic spectra associated with the known directivities on the sphere so that they reflect the noise levels that would be measured on the constant radius spherical surface instead of those levels measured at varying distances from the helicopter on the ground. There are two primary mechanisms through which the amplitude of noise is reduced as it propagates through the medium – spherical spreading and atmospheric absorption. Spherical spreading losses are caused during three-dimensional propagation as the sound waves radiated uniformly from the sound source at the speed of sound. The wave front can then be viewed as an expanding sphere with area increasing in proportion to the square of the radius. Since the overall sound power must be preserved, the sound power per unit area, or sound intensity, must decrease with the overall change in area. The intensity is proportional to the square of sound pressure amplitude. Therefore,

$$I \sim \frac{1}{r^2} \sim p^2 \implies p \sim \frac{1}{r} \qquad (6)$$

The pressure amplitude of the measured far-field noise at the observer can then be related to that on the sphere through a ratio of propagation distances:

$$p_s(t) = \frac{r_o}{r_s} p_o(t) \quad (7)$$

The effect of atmospheric absorption is more complex. As the sound waves travel through the medium, some of the energy is absorbed into the air through two primary mechanisms, viscosity which is termed classical absorption, and the rotational and vibrational relaxation of the molecules which form the medium. Both types of absorption depend on the wavelength of the sound waves – generally, the amount of absorption increases as the wavelength decreases. From 50 Hz to 10 kHz, the dominant form of absorption is due to the vibrational relaxation of oxygen and nitrogen, the amount of which is dependent on the temperature, pressure and humidity of the air. By assuming that each narrowband frequency bin can be modeled as a pure tone, semi-empirical atmospheric absorption models can be used to find a correction factor for each frequency bin. The Sutherland and Bass classical and molecular relaxation model has been standardized by the ISO and is used in this research – details of the implementation can be found in Appendix B. This model is considered valid within the 50Hz to 10 kHz frequency range, and for distances of up to several miles, and so is well suited for the purpose of constructing medium to high frequency acoustic hemispheres for rotorcraft. [27]

Having corrected the noise levels to an equidistant propagation distance of 30 ft on the surface of the hemisphere, the narrowband spectra may now be summed up into any desired configuration of broader bands or noise metrics; for instance, by applying

frequency weighting curves to mimic the response of the human ear. For this particular application, the BVISPL metric is used, which evaluates the unweighted sound pressure level of all bins between the 6th and the 40th harmonics of the blade passage frequency. This does not consider the main rotor fundamental noise, only main rotor BVI noise. However, the tail rotor thickness and loading noise are generally radiated in this frequency range. This SPL value is placed on the surface of the hemisphere at the associated angular position. The process is repeated for each microphone at all known positions of the helicopter along the flight track, forming an unstructured grid of sound directivity and magnitude information on the surface of the hemisphere. This data is then interpolated onto a structured grid of azimuth and elevation angles for use with propagation software, such as RNM.

In contrast, RNM's current Acoustic Repropagation Technique (ART) subroutine uses an observer time reference, calculating the SPL measured by each microphone at fixed observer time intervals. For each observer time step, the flight trajectory must be scanned in order to find the position in time and space from which the helicopter's emitted noise would have reached the microphone at the observed time. Not only is this approach more complicated, it also restricts the calculation of noise measurements on the surface of the hemisphere to those which correspond to the fixed observer time intervals chosen before processing the data.

Hemispheres created from ground acoustics data describe the far-field directivity and magnitude of radiated noise about the helicopter, but do so using measurements made at different emission times. A key assumption in the hemisphere generation process is that the magnitude and directivity of the externally radiated noise do not change during the

data collection process. In order to provide a means to assess the variability of the acoustic data from ground based measurements, multiple runs must be made for the same flight condition.

In-flight noise measurements may also be made by affixing an array of microphones to the helicopter, or by using a quiet aircraft in closely proximity to the helicopter to record noise at selected directivity angles. In contrast to ground based measurements, in-flight acoustic measurements describe the magnitude of noise emitted in a limited set of directivity angles, but this measurement can be made for all points in time.   For this reason, in-flight acoustics measurements provide a valuable measure of the variability of the acoustic state of the helicopter – allowing the quality of the measured data to be assessed in a single pass. [28] An in-flight array of microphones mounted to a modified crop dusting spray boom has been used to cross-check the ground noise levels and pulse shapes for the Bell 206B helicopter for which acoustic hemispheres are developed in this thesis, showing good agreement between in-flight measurements and ground based measurements when both are repropagated to the hemispherical surface. [29]   The incorporation of in-flight acoustic measurements into the hemisphere creation process allows for the real-time evaluation of the consistency of acoustic flight test data, allowing for increased confidence in the accuracy of the acoustic data without the expense of flight testing repeated cases.

2.5 Array Design

The choice of microphone locations on the ground will impact the distribution of datapoints on the surface of the hemisphere. Ideally, the datapoints would be uniformly distributed on the sphere, minimizing sparseness and therefore increasing the accuracy of interpolation schemes globally. However, as the helicopter passes over the linear array of microphones (Fig. 20), each microphone may make a measurement at any time that reasonably accurate knowledge of the helicopter's position is available. In effect, each microphone traces a dense line of measurements across the surface of the hemisphere as the helicopter flies over the array. Relatively large sparse regions will then lie between the microphone traces. (Fig. 21)
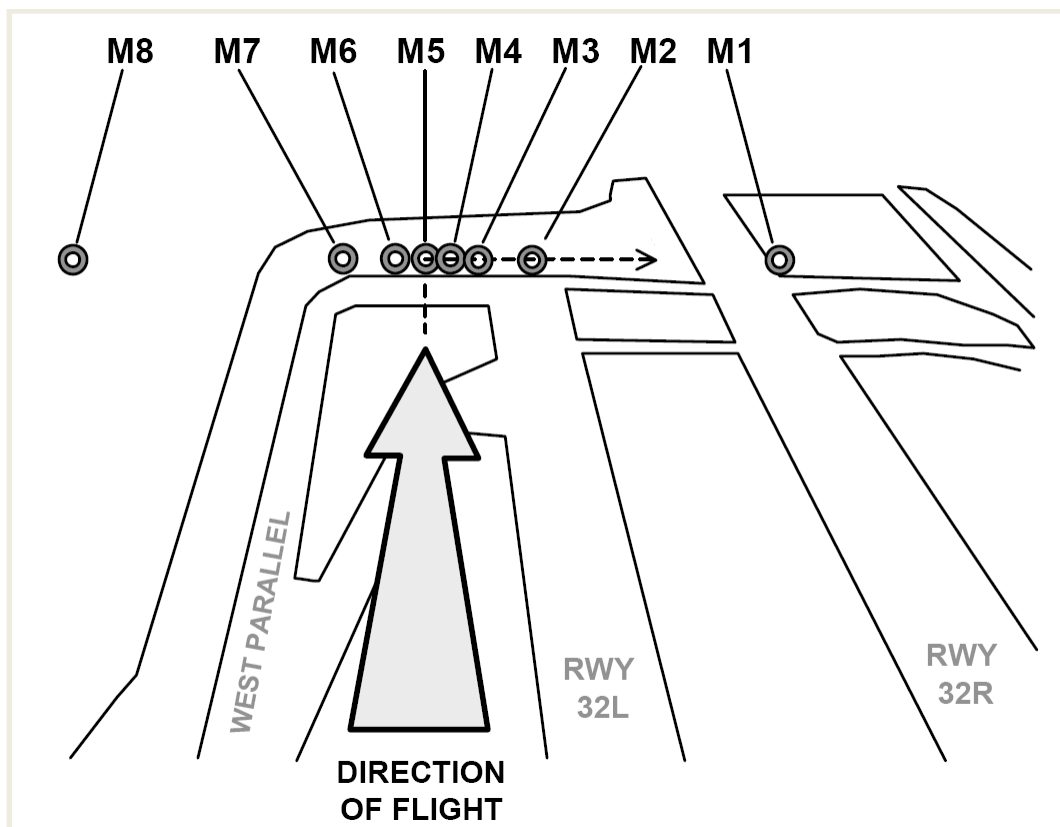

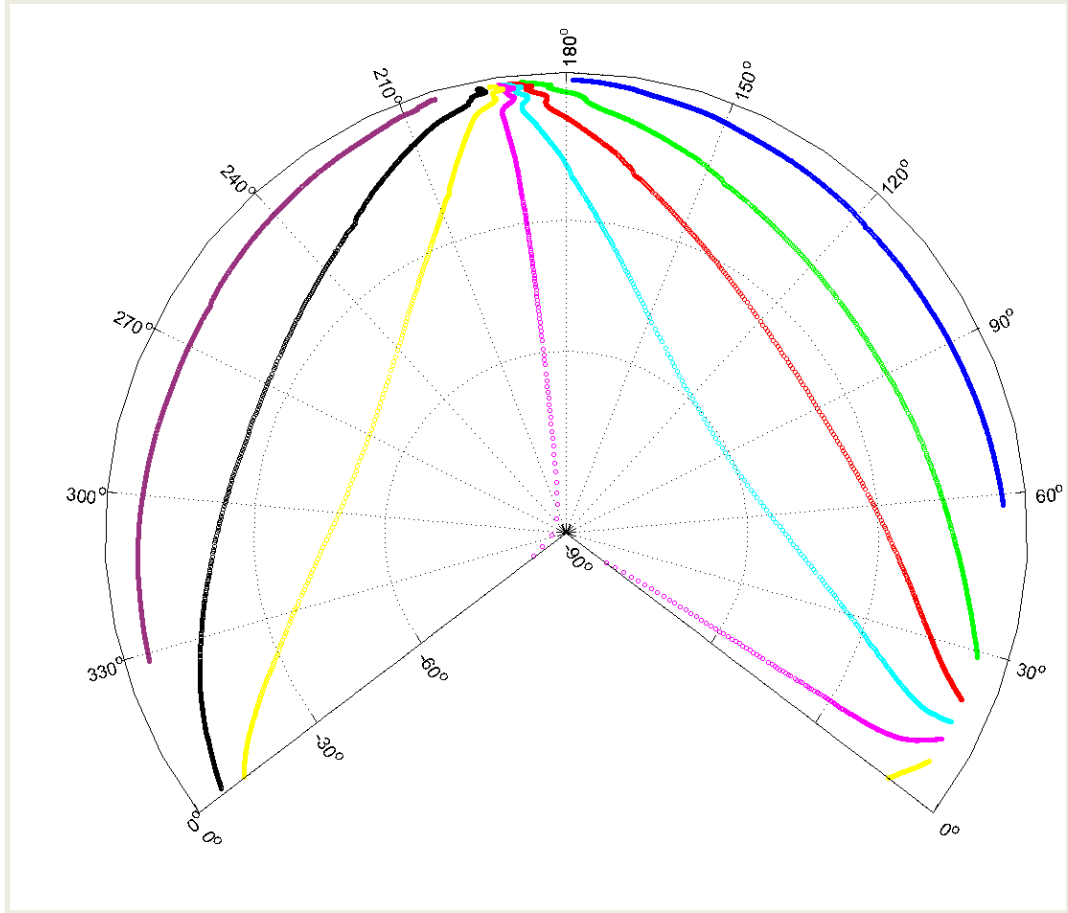**Figure 20: Linear Microphone Array**

Figure 21: Distribution of Measurements on Acoustic Radiation Sphere, Steady Straight-Line Flight

Capturing measurements on the underside of the acoustic hemisphere requires that the helicopter fly directly over a microphone in the array. For straight-line flight trajectories, additional microphones can then be placed linearly across the direction of the flight path in order to ensure an even angular spacing laterally across the sphere. In order to make measurements near the horizon, the microphones must either be placed very far away (degrading the signal-to-background-noise ratio of the measurement) or must be elevated on towers. Alternatively, the helicopter may pass over the array at a lower altitude – increasing the angular separation on the hemisphere between the microphones composing

the array and improving the microphone signal-to-background noise ratio, at the cost of reduced lateral hemisphere coverage near the horizon plane.

As the helicopter flies a straight-line trajectory orthogonal to the linear array, the microphones composing the array will make noise measurements sweeping across the hemisphere from front to back. Measurements near the horizon on the front and back of the acoustic hemisphere can be achieved by beginning and ending the data collection run farther away from the array. However, during climbing or descending runs, the trajectory must be carefully considered. Passing over the array at a low altitude will allow measurements to be made which are closer to the horizon on the left and right sides of the hemisphere, but will require the pilot start or end the run closer to the array to avoid collision with the ground. Likewise, crossing the array at a higher altitude enables a longer run and more in-plane data longitudinally but at the cost of less coverage laterally. For particularly steep ascent or descent angles, it may be desirable to combined measurements from two trajectories crossing at different altitudes, e.g. during a steep descent measurements from a run where the helicopter descends to a low altitude just before to the linear microphone array could be combined with measurements from a run where the helicopter descends to a low altitude just after the microphone array. Such an approach would ensure good coverage near the horizon plane in both the front and rear portions of the acoustic hemisphere. Similar considerations apply to the design of the array for turning flight trajectories, and one array design may be suitable for both purposes. Turning flight array design is explained further in section 6.1.3.

Chapter Three: Interpolation of Data on Acoustic Hemispheres

In order to provide easily used and understood information about the helicopter's external noise radiation, the ground noise data mapped onto the hemispherical surface must be interpolated so that noise levels may be displayed and identified across a range of angles on the surface. This interpolation problem is quite challenging for several reasons: the data sites are scattered across the surface and do not lie on any specific grid, data sites are non-uniformly distributed across the surface with both high density and sparse regions, and the interpolation occurs across a spherical surface in 3D space. Many methods have been used in the past which largely ignore these considerations, leading to distortions of the displayed data and inaccurate results within the sparse regions.

3.1 Traditional Interpolation Methods used in RNM

3.1.1 Triangulation-Based Interpolation

3.1.1.1 Two-Dimensional Triangulation

One of the most commonly used and simplest methods of handling the interpolation problem is to transform the spherical surface to a two-dimensional planar surface. This approach immediately reduces the problem to the interpolation of scattered data on a plane, for which there are many well-known solutions. After the data has been interpolated to a finer scale, it must be transformed back to the spherical surface so that the hemisphere may be used in RNM's ground noise propagation simulation. The most common approach for handling scattered data transformed to a planar surface which has been employed in earlier versions of RNM is to perform a Delaunay triangulation. [35] A Delaunay triangulation is defined as a network of triangles between points such that no

points lie inside the circumcircle of any triangle in the network. Delaunay defines the circumcircle as the circle which passes through all three vertices of the triangle. This approach is shown to maximize the minimum angle of each triangle in the network, discouraging the formation of long and slender triangles. This property is good for interpolation over these networks, because slender triangles favor one direction over others, with no accounting for the physics of the problem. Triangulation is performed using iterative schemes – typically an initial network is formed by connecting nearest neighbors, the network is tested to see if the Delaunay condition is met, and then it is modified in an attempt to meet the Delaunay condition. Various methods of modification and evaluation are used, such as simple flipping and more complex divide and conquer algorithms. In any case, the generation of such a triangulation is relatively inexpensive. Figure 22 illustrates a successful triangulation (A) and an unsuccessful triangulation (B) of the red vertices resulting in the blue circumcircles. The pink circumcircles in the failed triangulation contain the vertices in green, therefore not satisfying the Delaunay condition. By eliminating the network connection in orange and replacing it with a "flipped" connection between the two green vertices, the successful triangulation (A) can be generated.
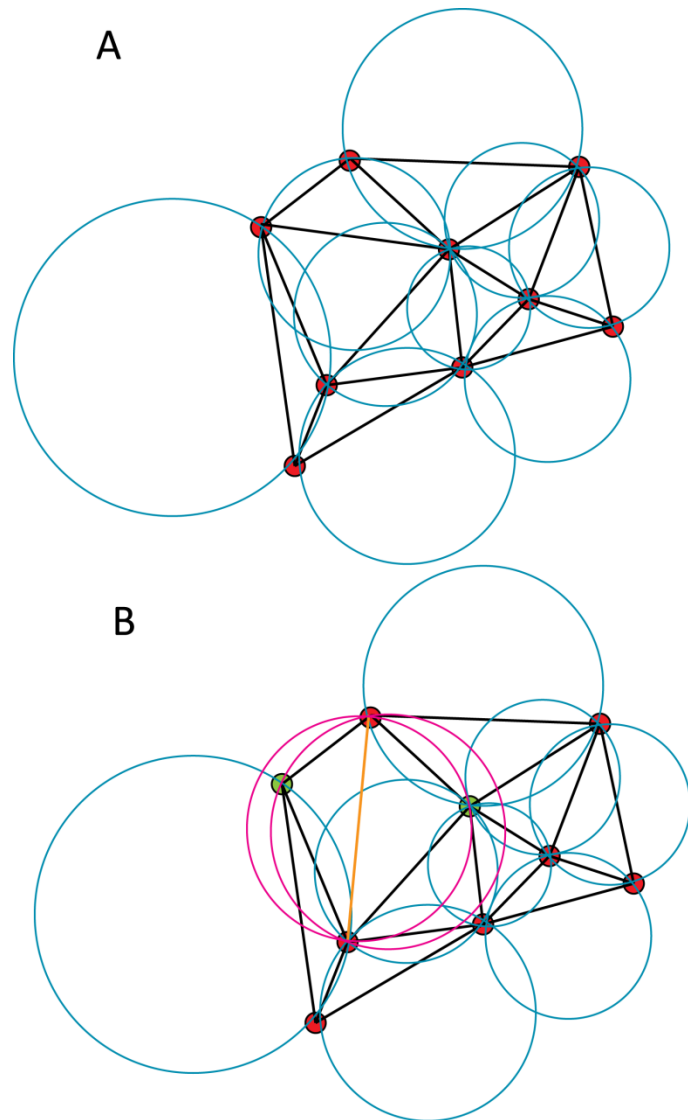
Figure 22: Selection of a Delaunay Triangulation. A is successful, B violates the Delaunay condition

After the triangulation is complete, the values of interpolants may be estimated by taking a 2D linear interpolation resulting from the values of the three verticies defining the triangle containing the interpolant; the values and locations of these three points effectively define a planar surface approximation to the noise contour over the sphere.

Significant problems results when applying this method to the hemispherical noise data set. The first problem is inherent in transforming any spherical surface to a planar

surface. As mentioned in Section 2.2 of this paper, Euler has proven that no projection of

a spherical surface onto a planar surface can be both conformal and equal area. This

property affects the interpolation process as well as the display of the hemisphere. Since

the relative distortion of the geometry increases as the distance between points on the

projected surface is increased, this distortion is greatest for interpolants located in the

sparse regions of the hemisphere.   A careful choice of the projection method can be used

to try to minimize distortion although distortion can never be eliminated. However,

frequently the angular coordinates of the sphere are simply transformed to a rectilinear

grid, providing significant distortions in both directional and distance relations between

points of the projection.   Sometimes attempts are made to reduce the distortion due to

this transformation by subdividing the problem into smaller planar projections – for

instance the hemisphere may be divided in half, separating the advancing and retreating

blade sides. Each half may they be transformed to planar coordinates, triangulated,

interpolants evaluated at structured locations, and then results projected back to the

spherical surface. These segments may then be blended back together at the seam in

order to generate a smooth surface. The blending process is aided in the case of a

straight-line flight trajectory passing over the centerline microphone in the array, since

data sites exist near the boundary of the two halves, guaranteeing that interpolants on the

boundary will be similar for both left and right halves of the sphere. While this technique

reduces some of the distortion inherent in projection, it does not eliminate it. Subdividing

the hemisphere further could reduce projection distortion, however it makes blending

more difficult and disruptive since it is difficult to find additional seam locations and

requires interpolation schemes be local, since they can only work over a single

subdivision.   Furthermore, most planar projections of spherical surfaces do not correctly reflect the periodic boundary conditions of spherical coordinate systems; i.e. interpolants calculated for zero degrees azimuth must be equivalent to those calculated for 360 degrees azimuth, since both points represent the same location on the sphere. Care must be taken to reflect these boundary conditions on the planar surface by choosing a suitable projection or through tiling the projection at the borders.

3.1.1.2 Three-Dimensional Triangulation

Techniques have been developed to produce triangulations in higher-dimensional space, eliminating the need for a projection of the spherical surface to a two-dimensional plane and thereby the associated distortions.[36] However, such a triangulation provides only a coarse approximation of a smooth sphere. Moreover, the distribution of data sites on the surface yielded by the hemisphere creation process is not well suited to any triangulation scheme. The resulting triangles will be very poorly selected since the data is distributed densely along the microphone traces with large sparse regions in between. Triangles which stretch across the densely populated microphone traces will be very slender – as previously mentioned, this unfairly weights on direction over another, distorting the resulting interpolants.   Even when the triangulation meets the Delaunay condition, yielding a maximum of the minimum angles of the triangles in the network, the triangulation in these sparse regions will be poorly conditioned. Finally triangulation, like any linear scheme, is ill-suited to extrapolation of the results.

3.1.2 Spherical Meshes of Spline or Polynomial Fits

A higher-order method commonly applied to spherical interpolation and used in later versions of RNM to develop noise contours on acoustic hemispheres is to fit a mesh of splines or polynomial functions across the sphere to the known values of the data sites.[37] Typically, the splines or polynomial functions composing these meshes are aligned with the coordinate grid on which the interpolants are placed –in this case along the azimuth and elevation of the hemisphere.   Often, the fitting of the spline or polynomial requires control points which must lie somewhere along the curve, however some more modern methods can use off-curve control points located at the data sites at the cost of considerable computational complexity.[38] The values of these on-curve control points must be interpolated using some local interpolation scheme, typically a triangulation similar to that mentioned in the previous section or a Laplace nearest-neighbor scheme. While these local schemes are adequate for interpolants near the dense regions, they are invalid in the sparse regions. The interpolants in the sparse regions must come from the curve fits.

In this higher-order interpolation scheme, polynomial functions are generally fitted using a least-squares method – typically the order of the polynomial fitted will match the number control points which lie along the fit. This will yield a well-posed least squares problem where a polynomial can be fitted which passes exactly through the value of each control point through the solution of a linear system of equations:

$$p(x) = c_0 + c_1 x + c_2 x^2 + \cdots + c_k x^k \quad (8)$$

47

$$\begin{bmatrix} 1 & x_1 & \cdots & x_1^k \\ 1 & x_2 & \cdots & x_2^k \\ \vdots & \vdots & \ddots & \vdots \\ 1 & x_n & \cdots & x_n^k \end{bmatrix} \begin{bmatrix} c_0 \\ c_1 \\ \vdots \\ c_k \end{bmatrix} = \begin{bmatrix} p(x_0) \\ p(x_1) \\ \vdots \\ p(x_n) \end{bmatrix} \qquad (9)$$

The most significant problem with polynomial fitting is Runge's phenomena. Runge's phenomena occurs when polynomials of high degree are fitted a sequence of control points. While the least-squares fit above guarantees that a polynomial of a degree equal to or higher than the number of control points will be fitted exactly to the known data at the control points, high degree polynomials tend to oscillate between control points, and may diverge substantially from the actual physical phenomena over spare regions.

The standard solution to this problem is the introduction of splines. Splines are piecewise-defined functions, composed of many low-order polynomials. Each low-order polynomial is defined with boundary conditions requiring smoothness and continuity between spline segments. The most common spline variant is the cubic spline, which uses polynomial segments of degree three. Each cubic spline segment then spans between two adjacent control points – this defines two degrees of freedom of the cublic polynomial. The other two degrees of freedom are established by boundary conditions at each control point ensuring that the slope of the segment at these control points is equal to the slope at the same control point defined by the neighboring segment. Various methods are used to choose the slopes at each control point – most commonly, the slopes are chosen from a moving average of the differences between control points, ensuring a smooth curve. The slopes at the endpoints of the spline are often chosen to be zero for the general case, however over a spherical surface, it is more appropriate to enforce periodicity. In the hemispherical case, splines which lie along constant elevation angles

will be periodic, but those which lie along constant azimuths will have to have clamped

boundaries; i.e. the derivative of the spline function at the endpoints is set to zero,

preventing any large departures in the spline fit at the horizon-plane of the hemisphere.

A simple method of evaluating a single interpolant on a spline mesh for the noise

hemisphere application is shown in Figure 23. This example shows a more complex

distribution of measurements, typical for a real-world measurements of a steady

descending turn maneuver (as shown later in Section 6.1.3) for pair of microphones. This

maneuver can cause the overlapping and looping microphone traces shown in Figure 23

for some array and trajectory designs. Local control points are generated on the dense

microphone traces from a spline interpolation scheme along the trace. These control

points are then used to fit spline curves along both the azimuth and elevation. The results

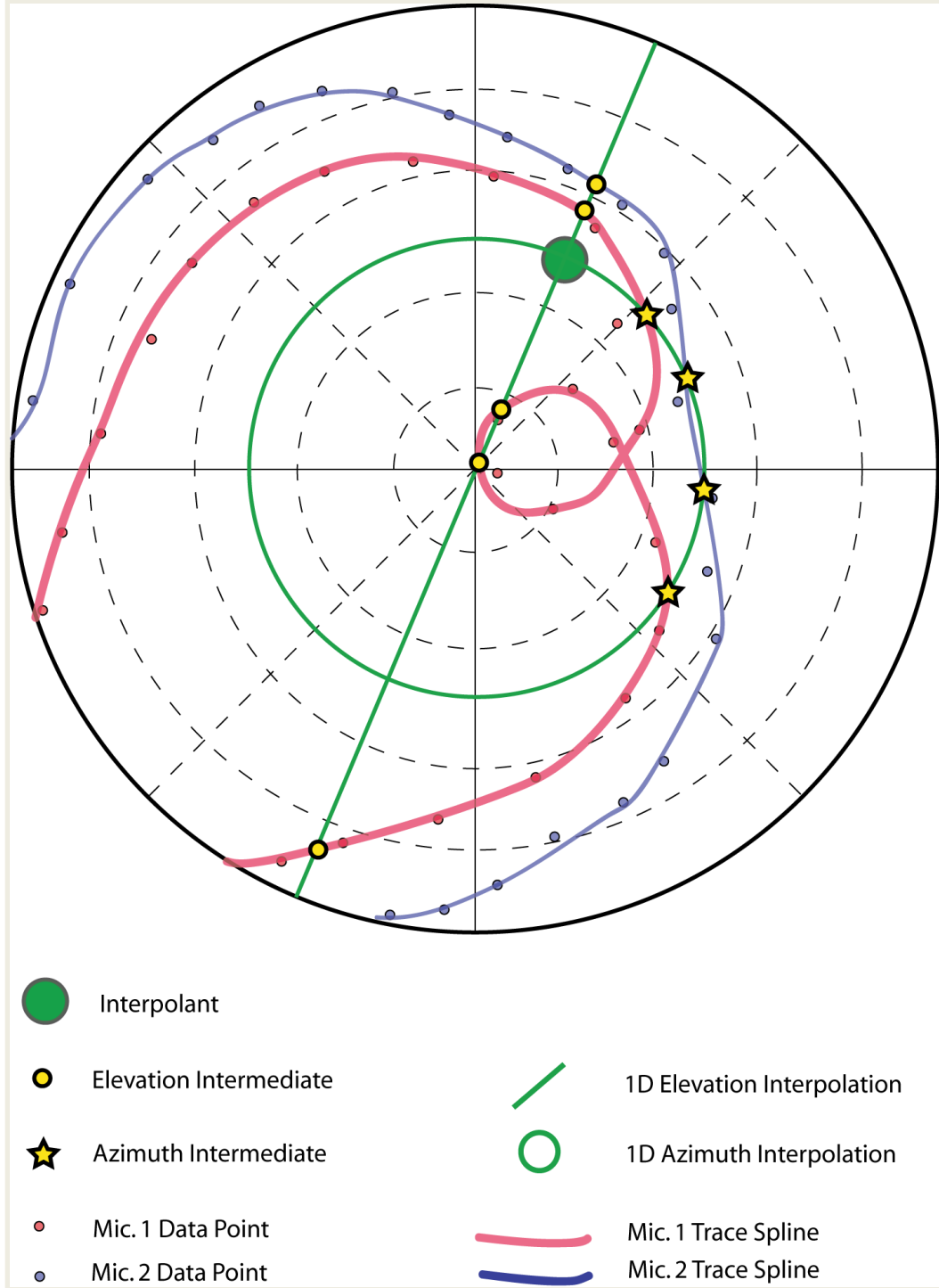from the azimuthal and elevation interpolation can then be blended.

Figure 23: Simple Spline Interpolation Scheme Applied to Typical Steady Turning Flight

50

There are several problems with the implementation of spline meshes for this application. The first problem is in the establishment of control points – in most methods, these control points are defined through triangulation, which due to the non-uniform distribution of data sites scattered on the sphere, is susceptible to distortion as noted previously.   Some methods have been developed in order to overcome this issue through alternative methods of computing control point values or by allowing off-grid control points – however, these methods suffer from much higher computational complexity and as of yet unresolved numerical stability issues.   Spline meshes have also been shown to become more inaccurate as the distribution of control points across the spherical surface is decreased.[39]   Selecting uniformly distributed control points requires applying inaccurate local interpolation schemes over large distances.   Moving the control points closer to the data sites, on the other hand, reduces uniformity in their distribution subsequently reducing the accuracy of the spline based scheme. Lastly, spline and other polynomial curves are not suitable for extrapolation.   In the extrapolated region, these curves tend to diverge rapidly from their values in the interpolated region. In sparse and unevenly distributed data sets, like in the noise hemisphere problem, spline mesh schemes can favor distant data points over local data points for interpolation. This occurs because distant data points may lie along the same spline as the interpolant when local data points are too far offset from the mesh.   This causes the spline method to utilize control points from far away, leading to distorted results.

3. 2 Radial Basis Functions

In order to overcome many accuracy issues inherent in the previous methods used to interpolate noise data on the surface acoustic hemispheres, a new approach to interpolating data on acoustic hemispheres is advanced and applied in this thesis. This approach is based on the theory of radial basis functions.

3.2.1 Prior Application

The radial basis function (RBF) approach was first developed in the 1950s for application in approximation theory.[40]   The suitability of this method for interpolation of scattered data was immediately recognized – however, when studying real-world problems, researchers quickly ran into unresolved problems with computational inefficiency and numerical stability. The method was put aside as developments to spline-based methods made them easier to use and applicable to a wider range of problems.

Research into RBF approaches began anew in the 1990s, as the RBF methodology was found to be closely related to the growing field of neural networks. A network of RBFs is a special case of a single-layer neural network. As more efficient and stable methods of solving neural networks were developed, the RBF scheme became practical for the solution to interpolation problems. Due to the flexible nature of RBF schemes, they have recently been adopted for interpolation problems in geodesy – where sparse measurements are made non-uniformly by satellites across the surface of the earth. The geodesy problem bears some similarity to the problem of interpolating ground-based acoustic measurements across the hemispherical surface – however, the distribution of

acoustic measurements across the hemispherical surface exacerbates the stability issues

of the method.

3.2.2 Theory

3.2.2.1 Rectilinear Coordinates

Any smooth function may be approximated as a linear combination of radial basis

functions. Each RBF is "centered" at some distinct point in space.   Each RBF is

weighted – these weights are selected to achieve the best known approximation of the

target function. The RBF approximation can be expressed in the following form:

$$f(x) \cong \sum_{i=1}^{N} v_i \phi\big(r(x, c_i)\big) \qquad (10)$$

The radial basis functions, ϕ, are weighted weighted by v_i. The argument, r, of the

radial basis function is some scalar representation of the distance between the

approximated point, x, and the center of the radial basis function, c_i. In rectilinear

coordinates, this distance is generally taken to be the Euclidean distance between the two

points, and may be evaluated in any number of dimensions.   Consequently, the value of

the radial basis function is not dependant on direction.

There are numerous radial basis functions in common use for a range of applications.

Some of the most common are Gaussian, multi-quaraditic, and exponential. These

functions are generally chosen to exhibit some smooth, continuously decreasing,

variation in value as the distance from the center increases.   For interpolation problems,

it is also desirable that the functions do not have a compact support, i.e. the radial basis

function should have a non-zero value across the entire interpolation region. When RBFs

have infinite support, all RBFs extend through all data sites and interpolants. The

weights of the RBFs can then be determined by solving a linear system, where the vector

of weights are solved for from a coefficient matrix of RBF values for each combination

of center and data site location and the vector of known function values, f:

$$
\begin{bmatrix}
\phi(r(x_1,c_1)) & \phi(r(x_1,c_2)) & \cdots & \phi(r(x_1,c_N)) \\
\phi(r(x_2,c_1)) & \phi(r(x_2,c_2)) & \cdots & \phi(r(x_2,c_N)) \\
\vdots & \vdots & \ddots & \vdots \\
\phi(r(x_N,c_1)) & \phi(r(x_N,c_2)) & \cdots & \phi(r(x_N,c_N))
\end{bmatrix}
\begin{bmatrix}
v_1 \\ v_2 \\ \vdots \\ v_N
\end{bmatrix}
=
\begin{bmatrix}
f(x_1) \\ f(x_2) \\ \vdots \\ f(x_N)
\end{bmatrix}
\qquad (11)
$$

This formulation produces a function approximation which is exact at all known data

points. If the RBF are chosen with compact support, some data sites may not lie within

some RBF and the resulting problem may be over or under constrained. Additionally,

approximation with compactly supported RBF limits the domain of the approximating

function since the RBF have non-zero values over a finite region.

The centers of the radial basis functions may be chosen arbitrarily – however, for

interpolation problems good results are generally achieved by collocating the RBF

centers with the data site locations. This collocation ensures that each data site is

strongly represented by at least one RBF. The formulation of the RBF-based

approximation does not depend on the distribution or uniformity of data sites. The RBF

approach is well suited to scattered data.

3.2.2.2 Spherical Radial Basis Functions

The radial basis function approach is readily adapted to interpolation on spheres or other curved surfaces. Recall that the argument of the RBFs is some scalar metric of distance. While in rectilinear coordinates, it is natural to use the Euclidean distance – in the spherical case it is desirable to have the interpolation scheme work across the surface of the sphere, not along the shortest straight-line path between the points. One representation of the distance between two points on the surface of the sphere is the geodesic distance. The geodesic distance is defined as the shortest path along a surface between two points on that surface. For a sphere, this is the Great Circle distance (Figure 24), which may be expressed between two points described by vectors A and B as:

$$r(A, B) = arccos(A \cdot B) \qquad (12)$$
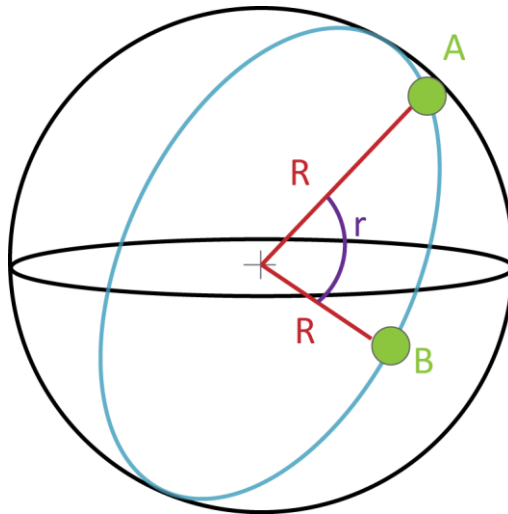
Figure 24: Great Circle or Geodesic Distance

By working along the geodesic distance the spherical geometry is inherently respected – there are no distortions introduced due to the projection or transformation of the coordinate system. Periodicity about the spherical coordinates is also guaranteed,

since all relations between points are made along the shortest distance along the Great

Circle between points on the sphere regardless of the location of elevation and azimuth

axes on the sphere.

A special radial basis function has been developed for use on spherical surfaces, the

Spherical Reciprocal Multiquadratic (SRMQ).[41] This function is defined as:

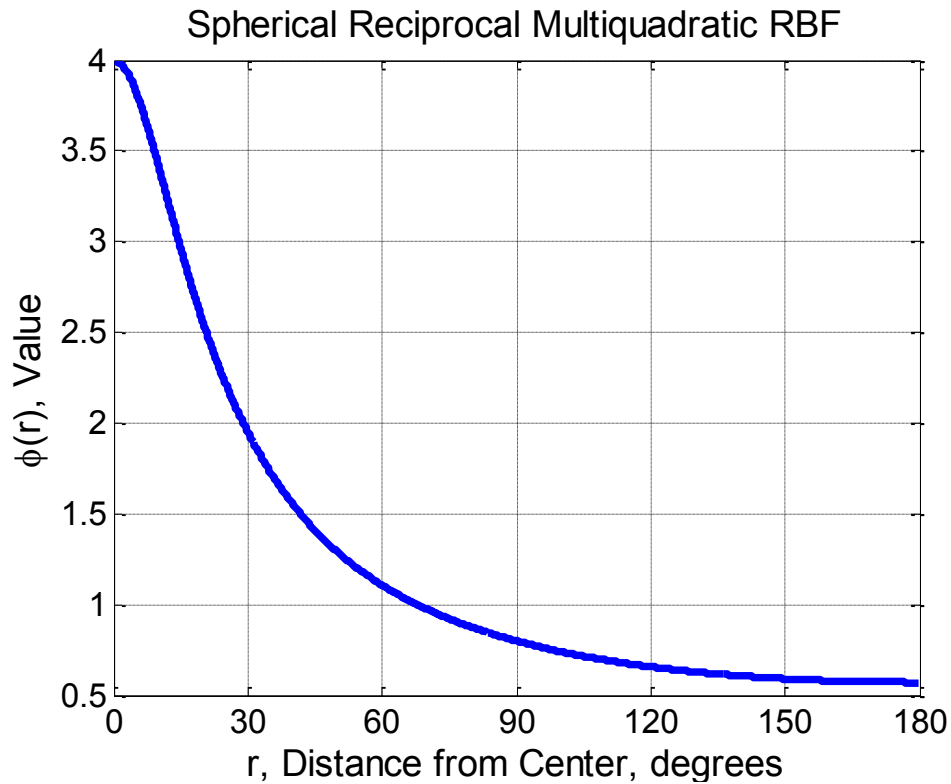$$\phi(r) = \frac{1}{\sqrt{1+\gamma^2-2\gamma\cos(r)}} \qquad (13)$$

Figure 25: SRMQ Radial Basis Function

γ is an arbitrary parameter chosen between zero and one which controls the steepness

of the SRMQ between the function center and a far away point. The SRMQ continuously

decreases from 0 to 180 degrees, which is the maximum possible geodesic distance

56

between two points on a sphere. (Figure 25) The SRMQ also has the special property

that is can be constructed from an infinite series of Legendre polynomials. It has been

shown that the coefficient matrix of RBF approximation problem will be positive definite

for combinations Legendre polynomials.[42] This guarantees that the RBF weights are

solvable for SRMQ bases. Furthermore, computational and theoretical studies have

shown SRMQs to provide more accurate approximations for scattered data on spherical

surfaces than other common RBF choices.

3.2.2.3 Radial Basis Function Stability Issues

Despite guarantees of positive definite coefficient matrices, the solution of practical

interpolation problems on spherical surfaces with radial basis functions remains

challenging. When data sites are clustered closely together (see Figure 21 for an

example), as they are along the traces of acoustic measurements, RBFs centered at these

locations become less distinct and produce similar values across the entire spherical

domain. The result is a coefficient matrix which is almost over-constrained, and thereby

nearly singular.   When numerical error is introduced during the computational solution

to a nearly-singular system of equations, the direct solution algorithms become unstable

and produce wildly inaccurate solutions for the weights required to fit the known data.

Compounding the problem is that RBF coefficient matrices are full – each entry is

associated with a RBF producing a non-zero value. Iterative solvers, like the various

Krylov subspace methods, converge more quickly and reliably when working on sparse

matrices.[43] When faced with full matrices with very large condition numbers (i.e. the

ratio of the highest Eigenvalue to the lowest Eigenvalue) and unclustered Eigenvalues, as

found in the acoustic hemisphere interpolation problem, these iterative methods become

very expensive and often fail to converge altogether. It is this problem which has halted the application of RBF to spherical scattered data interpolation until recently.

The problems of convergence and stability might be abated with a preconditioning scheme; the problem is transformed from a system which is difficult to solve to an equivalent expression which is easier to solve. This is achieved by pre-multiplying the system of equations with a preconditioning matrix, W, as below:

$$W \, \Phi \, \vec{v} = W \, \vec{f} \qquad (14)$$

Preconditioning requires some up-front computational cost in order to perform the transformation, but ideally improves the convergence of the preconditioned system enough to reduce the overall computation time.   As mentioned previously, fast iterative Krylov-subspace solvers work the best when the coefficient matrix exhibits several properties: sparseness, a low condition number, and clustered Eigenvalues. The ideal situation is a new coefficient matrix which is the identity matrix , i.e.:

$$W \, \Phi \, = \, \mathbb{I} \qquad (15)$$

In this circumstance the matrix is very sparse, has a condition number of one, and all Eigenvalues are the same. For most Krylov methods, this guarantees an exact solution in a single iteration. However, computing W to meet this condition requires finding the inverse of the original coefficient matrix – this is at least as difficult original problem! Instead, a preconditioning matrix which is easy to compute and still nearly the inverse of the original coefficient matrix is sought.

Beatson suggests a method for creating a system equivalent to the RBF interpolation problem with a well-conditioned coefficient matrix.[44] This is achieved by constructing a new basis function, the cardinal basis function, defined as:

$$\psi_i(x) = \sum_{j=1}^{N} w_{ij}\, \phi\left(r(x, c_j)\right) \qquad (16)$$

Where the cardinal weights form the preconditioning matrix,

$$\{W\}_{ij} = w_{ij}$$

The cardinal basis function is also defined to meet the cardinal condition:

$$\psi_i(x_j) = 0$$

$$\psi_i(x_i) = 1$$

$$i \neq j;\ i, j \in [1, 2, \dots, N]$$

The resulting preconditioning matrix becomes the inverse of the original coefficient matrix, and thereby the coefficient matrix of the preconditioned system is the identity. Solving for the preconditioning matrix in this fashion is very expensive. The weights of N cardinal basis functions must be solved for, each requiring the solution of an NxN system of equations. While using a pure cardinal basis proves to be more stable than most direct methods of computing the inverse of the original coefficient matrix, it is exceedingly slow.

Beatson suggests that the pure cardinal basis function can be approximated to reduce the computational costs, while still providing an excellent preconditioner. Beatson

59

defines an approximate cardinal basis function which considers only the β nearest points – all other weights are set to zero.

$$\psi_i(x) = \sum_{k=1}^{\beta} w_{is_{i(k)}} \phi\left(r\left(x, c_{s_{i(k)}}\right)\right) \qquad (17)$$

$$w_{ij} = 0, \quad j \notin s_i$$

Where s_i contains the indices of the β points nearest to x_i.

The problem has now been subdivided into two levels – a series of N local interpolation problems described by βxβ systems, and a global problem solving the NxN system resulting from the local solutions. The local problems may be solved efficiently through direct methods, such as LU-decomposition or as used in this paper, Successive Over-Relaxation (SOR). For β << N, the speed of computation is greatly increased – computation of the preconditioner is reduced to $O(\beta^2 N)$ operations. Beatson suggests that the Generalized Minimum Residual (GMRES) method be used to solve the global preconditioned system. Other common Krylov-subspace methods, such as conjugate gradient (CG) and stabilized biconjugant gradient (BiCGSTAB), were applied to the preconditioned systems developed for the acoustic radiation spheres in this thesis – it was found that GMRES converges best the most frequently on these real-world problems, often halting within a numerical tolerance of 10^{-6} after one or two iterations.

Brown, *et al*, suggest that instead of choosing the β nearest points, some commonly selected far away points should also be included in the formulation of the approximate cardinal basis functions.[45] This improves the accuracy of the approximation of the

60

basis functions in far away regions, therefore resulting in an interpolation scheme less biased to local points. This results in smoother interpolations.

Beatson's method can be readily adapted to the spherical domain. In this case, the RBF are chosen to be the well known SRMQ and are constructed to accept geodesic distance as the argument. The size of the problem may be effectively reduced by clustering points within dense traces of microphone data. This is performed by replacing small groups of points along the trace with a single point located at the average position of the group and having the average value – in effect, interpolating the traces to a coarser scale. In addition to further improving the convergence of the problem, this clustering helps in smoothing out some of the unwanted variations in acoustic levels measured over time. Such variations can be due to violations of the steady-state flight condition assumption or changing weather conditions – for example, pilot control inputs, atmospheric turbulence, or shifting wind conditions.

3.2.2.4 Radial Basis Function Properties

The radial basis function approach is well suited to the problem of interpolating scattered data on spherical surfaces. The smooth and non-oscillatory SRMQ basis function ensures the smoothness of the function approximation for noise levels over the entire hemisphere. This property is likewise desirable for extrapolation in the near-horizon elevation angles of the hemisphere, since the RBF tend to fall off gradually, mimicking the observed behavior of BVISPL noise levels in this region. The RBF scheme works on the surface of the hemisphere and does not favor any directions, resulting in an undistorted interpolation. RBF interpolation operates globally, but favors points nearby the interpolant avoiding the distortions often seen in spline or polynomial

mesh approaches. Using modern preconditioning schemes, RBF can be computed quickly and reliably for acoustic hemisphere data.

3.2.2.5 Spherical Splines

The spherical spline approach applies the concept of a spline curve in the framework of the radial basis function interpolation scheme. Instead of constructing splines along mesh grids, radial spline elements are used as basis functions for interpolation. Spherical spline formulations retain many of the strengths of RBF schemes, but evaluation of the basis functions is more complex. The advantage is a potentially more natural and subjectively visually pleasing interpolation. The spherical spline approximation function is constructed as follows:

$$f(x) \cong c_0 + \sum_{i=1}^{N} c_i g_m\big(r(x, c_i)\big) \qquad (18)$$

This construction of basis functions is very similar to that of the general RBF case, except a leading constant coefficient weight, c_0 must also be solved for. The spherical spline basis function is also composed of Legendre polynomials accepting an argument of geodesic distance; however, it is defined as a series:

$$g_m(r) = \frac{1}{4\pi} \sum_{n}^{\infty} \frac{2n+1}{(n(n+1))^m} P_n(x) \qquad (19)$$

Where $P_n(x)$ are the Legendre polynomials, which can be found using Rodrigues' Formula:

$$P_n(r) = \frac{1}{n!2^n} \frac{d^n}{dr^n} [(r^2 - 1)^n] \qquad (20)$$

m is often called the "order" of the interpolation – Perrin recommends m be chosen

greater than two. Obviously, it is impractical to evaluate the spherical spline basis for

infinite terms. Here Perrin suggests that for m = 4, only the first seven terms of the series

need be considered.[46]

There are some potential issues with this scheme, especially over sparse domains.

Higher-order Legendre polynomials are increasingly oscillatory. In the RBF case, the

infinite series of orthogonal Legendre polynomials composing the SRMQ basis is non-

oscillatory – however when terms are dropped, as in the finite spherical spline basis, this

oscillatory behavior is present in the basis functions. (Figure 26) This suggests that this

oscillatory behavior may become significant in sparse regions, where the interpolation is

relatively unconstrained. Likewise, this choice of basis may not be suitable for

extrapolation.
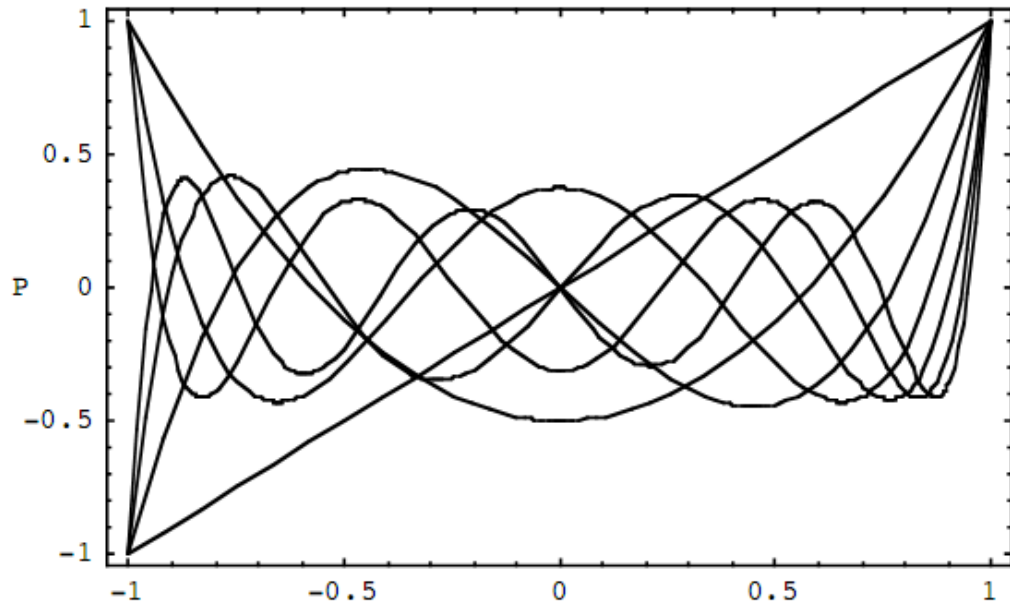
Figure 26: Plot of the First Seven Legendre Polynomials

3.2.3 Interpolation Accuracy

Before applying the newly developed interpolation scheme to measured Bell 206B

data, it is illustrative to evaluate the interpolation scheme on a representative set of

simulated data, for which noise levels are known across the entire range of directivity

angles. A simulated hemisphere of BVI noise previously developed in another study for

the AH-1 helicopter in descending flight was used to assess quantitatively the

performance of the interpolation schemes described in this chapter.[47] The AH-1 has

similar BVI noise radiation characteristics to the Bell 206B, both having two-bladed
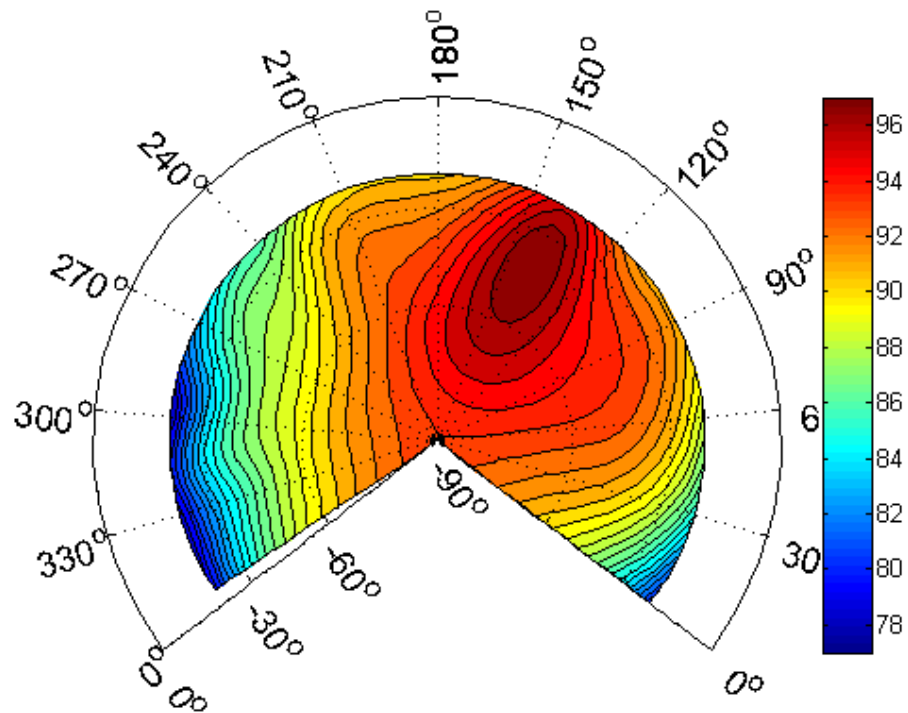
Figure 27: Simulated AH-1 BVI Hemisphere, dB effective BVISPL

rotors. This hemisphere is plotted in Figure 27. A group of points matching the geometry

of actual noise measurements made during a straight-line flight trajectory for the Bell

206B were selected from the simulated results and passed to the interpolation routine.

The results of the interpolation routine were then compared to all of the directivity angles

from the simulated noise levels predicted on the acoustic hemisphere to develop a map of

the error due to interpolation over the sparse regions.   The noise simulation considers

only the contribution of main rotor BVI noise, and does not include other main rotor

noise sources or the tail rotor noise. The output of the simulation is an overall unweight

SPL of the main rotor BVI noise – this is effectively the BVISPL metric for the main

rotor in isolation.

First, the 2D Delaunay triangulation is applied to a planar transformation of the
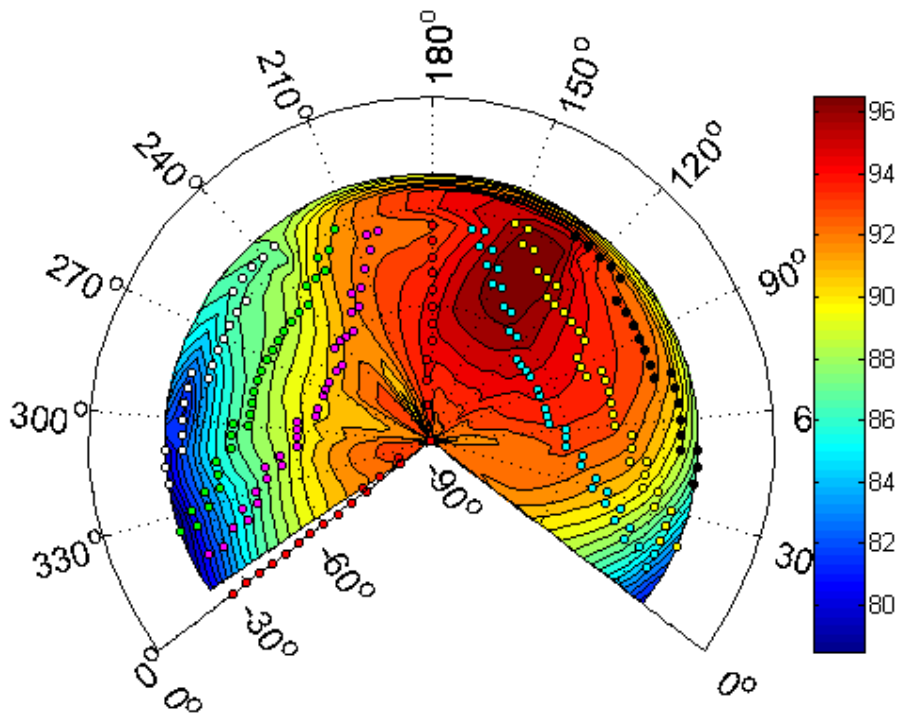
Figure 28: 2D Triangulation Interpolation Applied to Simulated AH-1 BVI Noise Data, dB effective BVISPL

hemisphere, shown in Figure 28.

The triangulation creates a coarse approximation of the noise contours on the surface of the sphere. In addition, on the underside of the sphere considerable distortion is observed due to the thin triangulation that occurs between the center microphone traces at a point on the sphere where the magnitude of noise is changing relatively quickly, yielding high distortion.

Figure 29 plots the difference between the SPL of the original simulated sphere and the levels approximated by the 2D Delaunay interpolation scheme.
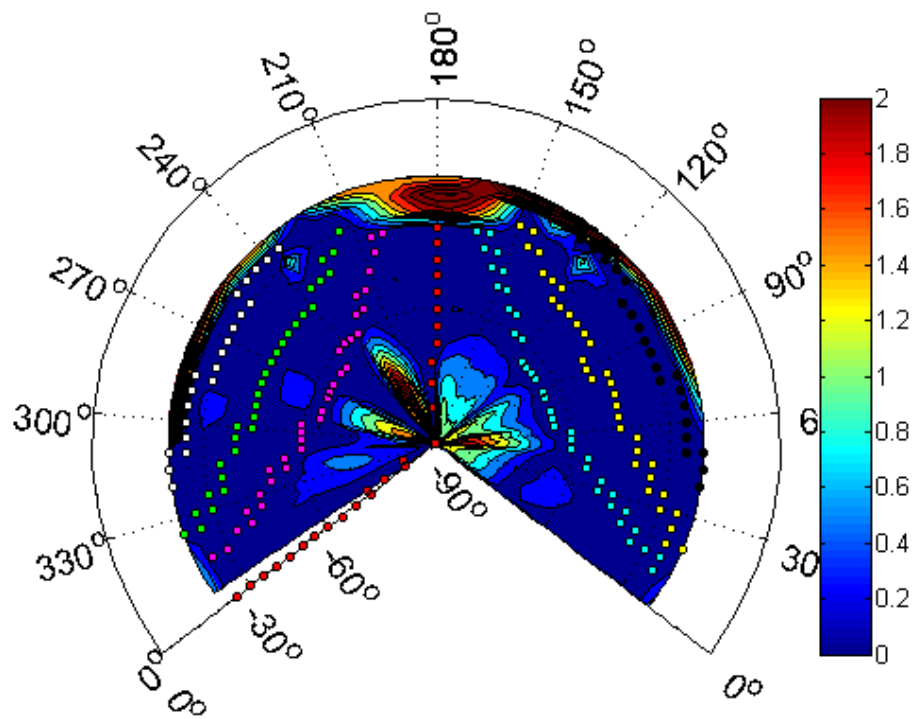
Figure 29: Map of the Absolute Error Values between Simulated and Interpolated Data for the 2D Delaunay Triangulation Scheme. Unweighted dB.

High error values of 5 dB and greater are observed on the underside of the

hemisphere, due to the poor scaling of the triangulation in this region. Additionally, at

the front of the hemisphere, near the horizon, high error values are also discovered. In

this region, triangulation scheme choose verticies for the triangles from points relatively

far away from the interpolant. While simple, this method does not provide an acceptable

level of accuracy across the acoustic hemisphere's surface.

Next, an implementation of a spline mesh is evaluated. (Figure 30).
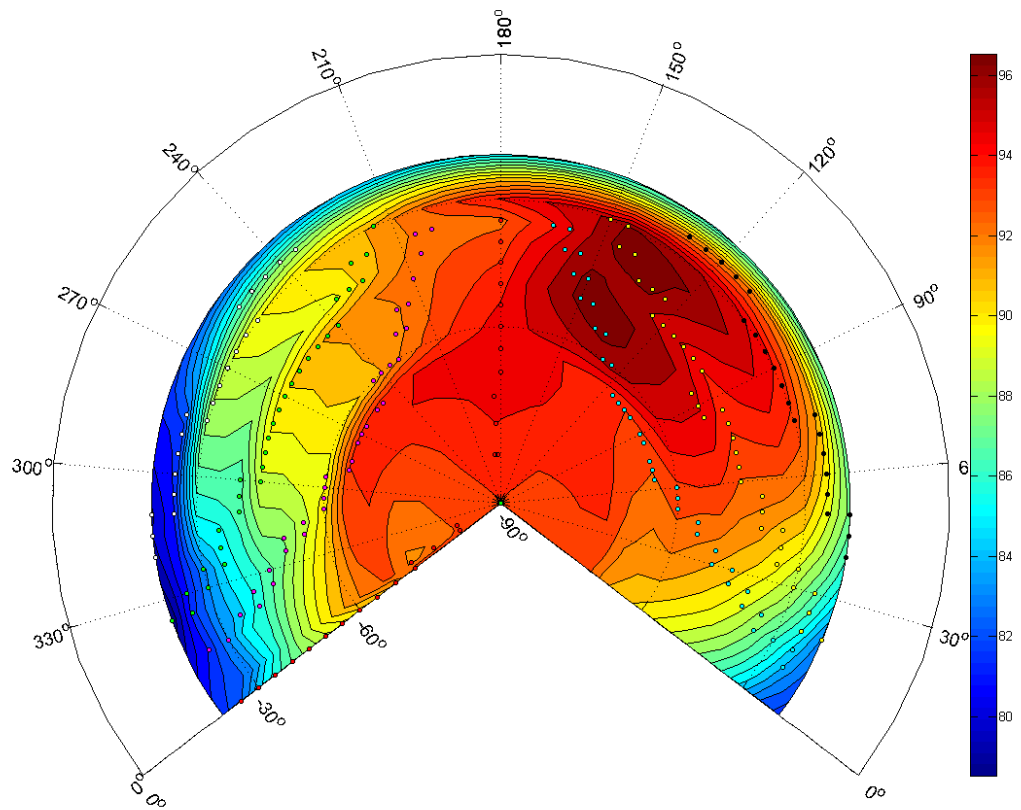
Figure 30: Spline Mesh Interpolation Applied to Simulated AH-1 BVI Noise Data, dB effective BVISPL

The BVI "hotspot" is ragged and poorly defined by this interpolation scheme, with significant distortion along the azimuthal direction.

These effects can be seen more clearly by examining the error between the true simulated values (Figure 27) and the interpolated sphere (Figure 30). Errors exceeding 3 dB are identified in the interpolated region (Figure 31) clearly show the inadequacy of this interpolation method.
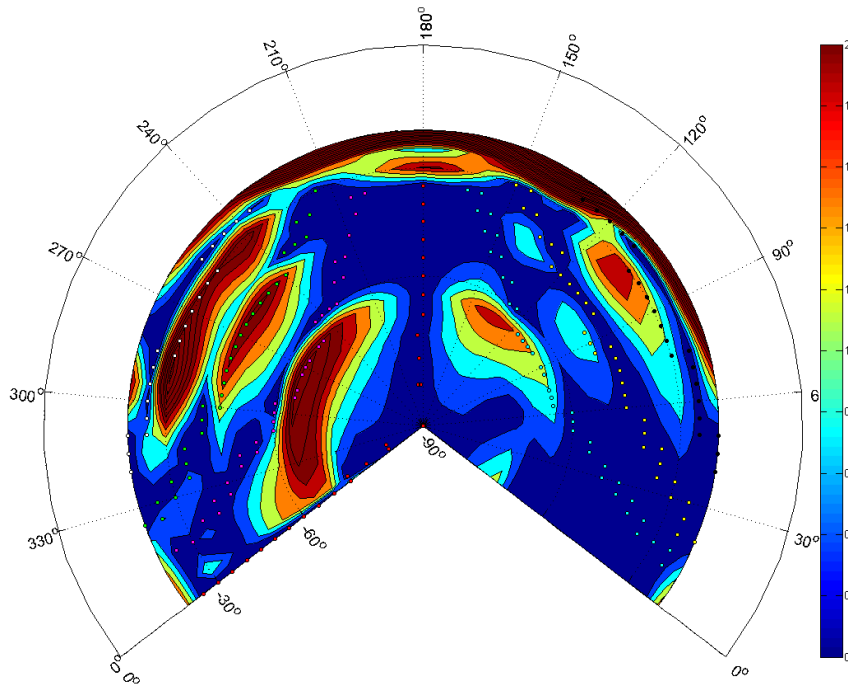
Figure 31: Map of the Absolute Error Values between Simulated and Interpolated Data for the Spline Mesh Scheme. Unweighted dB.

The new RBF interpolation method with the SRMQ basis function is applied to the
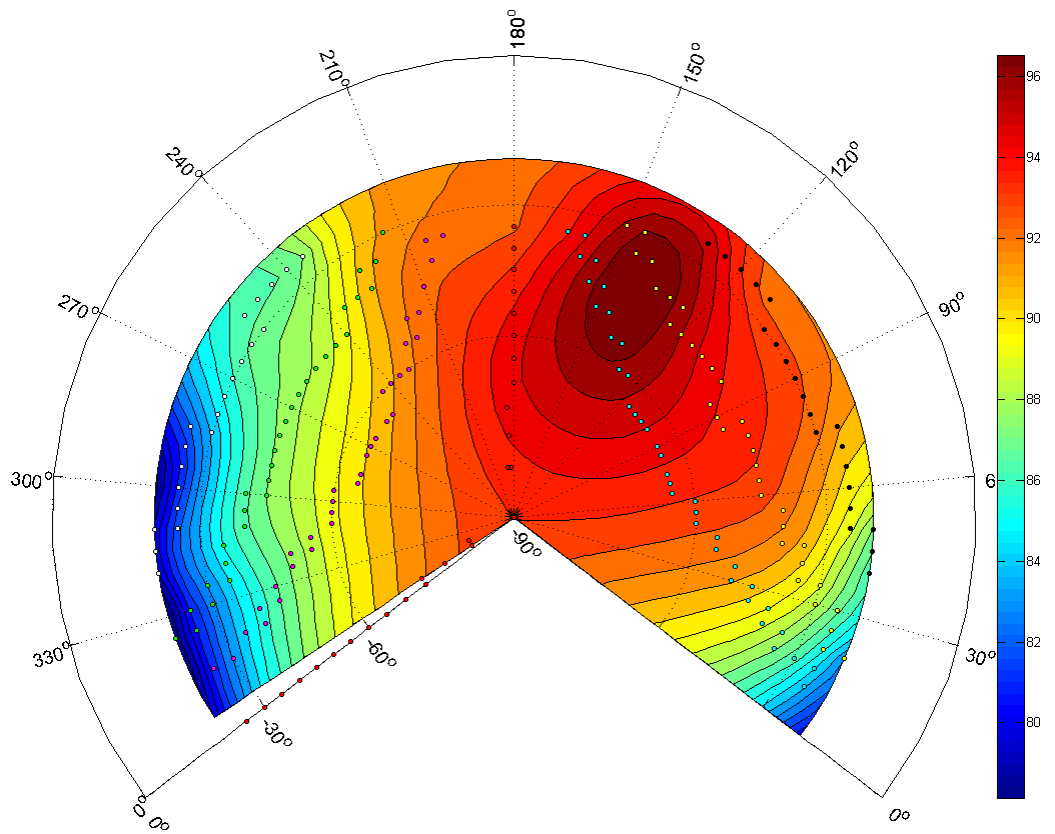points sampled from the simulated AH-1 hemisphere and is plotted below. (Figure 32)
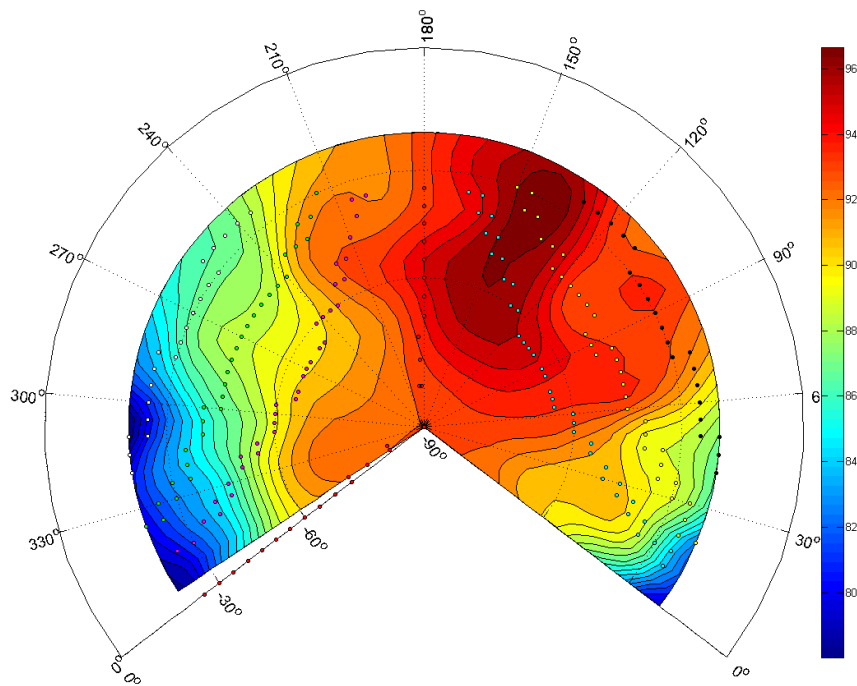
Figure 32: SRMQ Radial Basis Function Interpolation Applied to Simulated AH-1 BVI Noise Data, dB effective BVISPL

The noise contours generated by this method are smoother and appear to have a more
natural shape that either of the method previously used in interpolation of acoustic
hemispheres. The error between the simulated and interpolated values is plotted in
Figure 33.
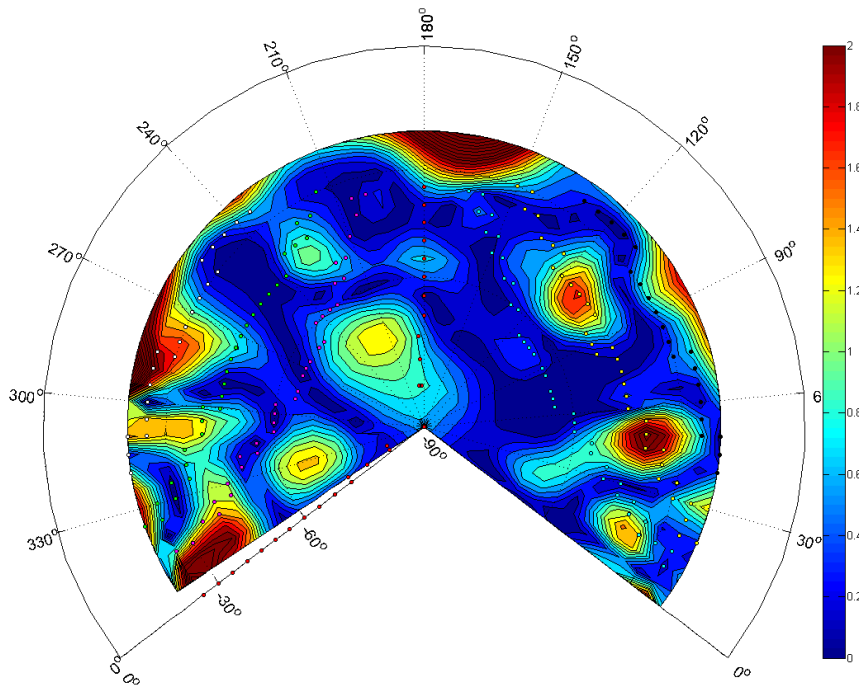
Figure 33:Map of the Absolute Error Values between Simulated and Interpolated Data for the SRMQ Scheme. Unweighted dB.

Overall, the error is reduced significantly, however it is apparent that some basis function weights are not well chosen by the method, leading to local regions with peak errors of almost 2 dB.

The results of using the RBF scheme with spherical spline basis functions to interpolate the helicopter BVI noise levels are shown in Figure 34 It is clear that the resulting contours are smooth and well behaved over most of the acoustic hemisphere. The result appears very similar to the exact simulated AH-1 hemisphere. (Fig. 27)

Figure 34:Spherical Spline Radial Basis Function Interpolation Applied to Simulated AH-1 BVI Noise Data, dB effective BVISPL

The noise contours are further smoothed over the SRMQ scheme, with less local variation. The absolute error values between the simulated and interpolated spheres are plotted in Figure 35.
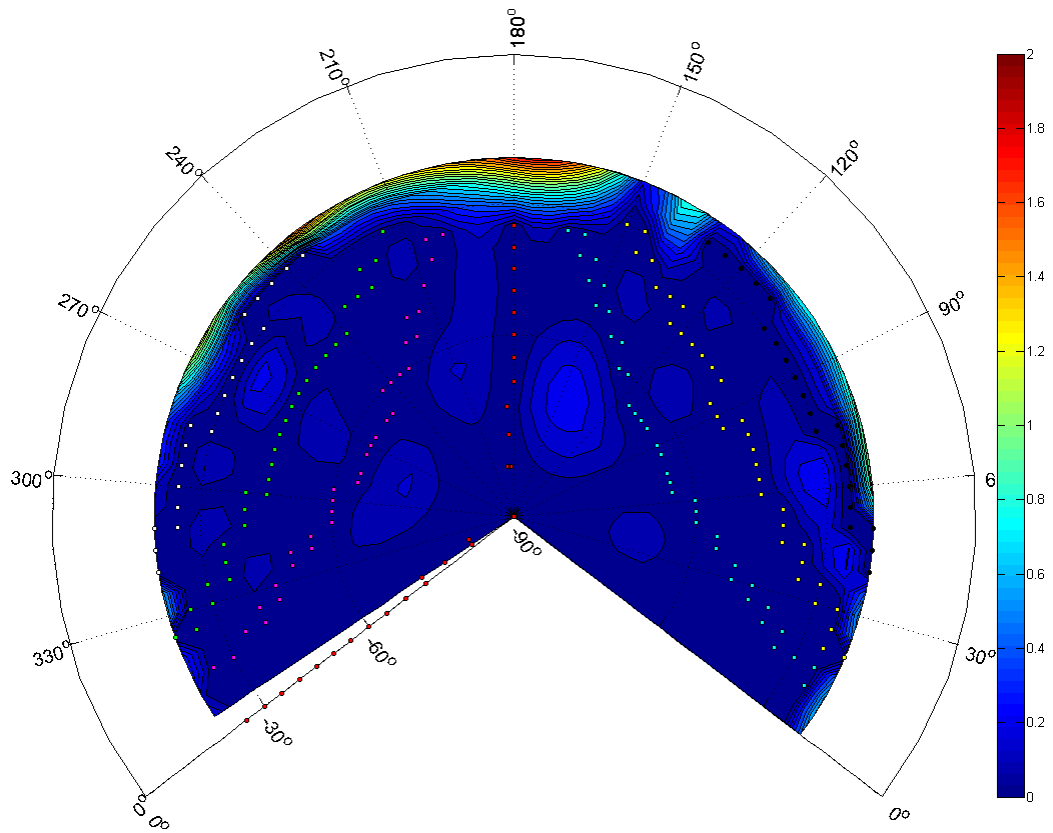
Figure 35: Map of the Absolute Error Values between Simulated and Interpolated Data for the New Radial Basis Function Interpolation with Spherical Splines Scheme. Unweighted dB.

Within the interpolated region, peak error values of only 0.2 dB are reached within the sparse region – a marked improvement over the previous interpolation methods. Near the front of the sphere, where results are extrapolated beyond the sampled data, the error increases to as much as 2 dB as the sphere is extended ten degrees closer to the horizon line. While these values are much higher than those inside the interpolated region, they are much improved over the other interpolation methods. Therefore, this method can

provide reasonable estimations of noise levels should extrapolation be necessary due to the difficultly of collecting near in-plane data from ground noise measurements.

Overall, the RBF method with spherical spline basis functions scheme is shown to converge more reliably and provide better accuracy over the interpolation region for typical BVI noise contours. This method will be used to develop the noise contours from ground measurements for the Bell 206-B helicopter in this thesis. Both of the radial basis function schemes appear to be superior to traditional spline mesh and triangulation based methods. It has been shown that a poor choice of interpolation scheme can lead to very significant variation of interpolated results – greatly diminishing the accuracy of the physical directivity and magnitude of the source noise.

Chapter Four: Acoustic Flight Test Campaigns

4.1 Test Setup

The Bell 206B acoustic data used in this thesis was gathered in two distinct flight test campaigns that were flown one year apart. The research testing was led by the University of Maryland at two different sites in Northern California. The University of Maryland team was led by Professor Fred Schmitz and consisted of three graduate students; Rick Sickenberger, the primary developer of the optical tip-path-plane tracking system, Cal Sargent, the primary developer of the air data boom and responsible for reducing the acoustic data associated with tail rotor noise as measured on the boom mounted microphones, and the author, who had the primary responsibility of gathering and reducing all of the acoustic data measured by the ground mounted microphones. The entire team took part in collecting the performance and acoustic data measured in the helicopter (~70 hours of flight time).

4.1.1 2006 Flight Test

In June of 2006, a Center for Rotorcraft Innovation (CRI) funded flight test was conducted by the University of Maryland, NASA, and the US Army Aeroflightdynamics
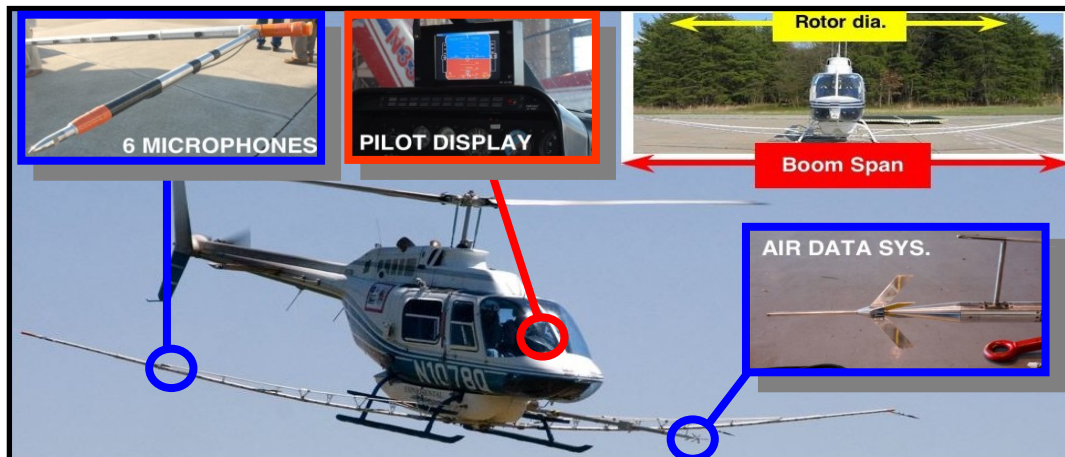
Figure 36: Bell 206B Configuration, 2006 Flight Test Program

Directorate at Moffett Field, CA to measure the noise radiation of the Bell 206B helicopter. The main objective of the flight testing was to gather a very high quality set of helicopter acoustic data under very controlled steady-state and accelerating conditions for both straight and turning flight. The re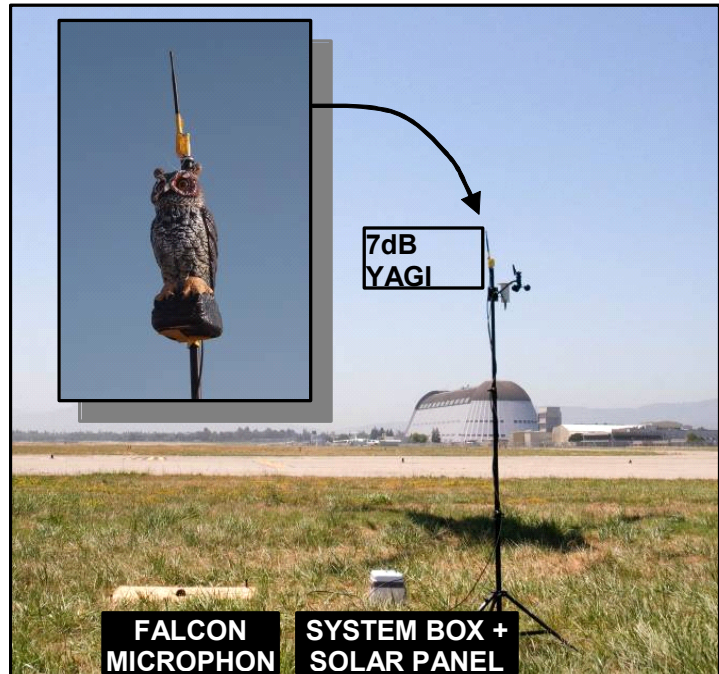sulting data set is unique in that it combines both in-flight noise measurements with ground noise measurements through a range of flight states, including level, descending, accelerating, turning flight, as well as combinations of these states. [29]

Figure 37: Wireless Ground Board Microphone

The in-flight noise measurements were gathered using a linear array of microphones mounted to booms extending from both the advancing and the retreating side of the helicopter. (Figure 36) The microphones were positioned to measure both the magnitude and directivity of radiated noise, and extend beyond the edges of the rotor disk to capture a wide range of blade-vortex interaction (BVI) noise. The radiated noise from this helicopter was altered by the addition of the microphone boom which increased the drag of the helicopter. As discussed previously, the increased drag resulted in an increased rotor inflow for any specific flight condition and thereby increased the effective descent rate required to reach the peak BVI noise radiation condition.

A team from NASA Langley Research Center conducted ground noise measurements using a linear array of reflecting ground-board microphones. (Figure 37) The ground boards were constructed of plywood and measured 1.5 x 1.5 feet. The main reason for using ground board mounted microphones was to avoid interference caused by the reflection of acoustic waves from the ground to above ground microphones.   For straight flight cases, the microphones were spaced to provide evenly spaced angular measurements on the helicopter as it passed over the array on either side of the slight path flight path. (Figure 38) In order to accurately model the propagation of noise from the helicopter to the ground based microphones, meteorological data was collected by a mobile weather balloon. The weather balloon was equipped with a weathercock anemometer, temperature probe, and hygrometer and was capable of traversing a range of

Figure 38: 2006 Flight Test Program Microphone Layout

altitudes, to provide wind and temperature gradients for each test point.

In-flight aerodynamic data was collected by mounting an air data boom extending from the front of the helicopter to reduce the influence of the main rotor wake on the measurements. The air data boom was instrumented with a swiveling pitot probe, alpha and beta vanes, a thermocouple, and a static pressure transducer. An on-board inertial measurement unit coupled to a differential GPS receiver provided additional measurements of velocities, accelerations, angular positions and rates, as well as absolution position tracking. In addition, an optical tip-path plane measurement system combined with air data measurements provided the aerodynamic angle of attack with respect to the longitudinal rotor tip-path-plane.[30] Accurate time synchronization was provided to all instruments, both in-flight and on the ground, through GPS carrier time synchronization.

To improve the consistency of the test data, the pilot was supplied with an on-board Portable Pursuit Display Guidance (PPDG) system developed at NASA Ames Research

Figure 39: PPDG Display System

Center.[31] The system used real-time measurement of the aircraft performance state to supply the pilot with a virtual "leader" aircraft. By following the virtual aircraft, the pilot

received gradual course corrections to help him maintain the desired flight state with minimal pilot induced unsteadiness. (Figure 39)

4.1.2 2007 Flight Test

Another complementary flight test was performed in June of 2007 at Hollister, CA. The main focus of this testing was to measure Bell 206B external noise radiation under even more controlled conditions and to more carefully look at the acoustic radiation patterns of steady turning flight. This test campaign was led by Bell helicopter with the University of Maryland, NASA, and the Army as testing partners. To keep background

Figure 40: Bell 206B Helicopter, 2007 Flight Test Program

noise levels very low and to insure very low winds, the test was run at a farm in Hollister CA. (Figure 40) In this test program, ground noise measurements were conducted by Bell using five wired microphones mounted 1.2 meters above ground and spaced 150

meters apart, in compliance with FAA noise certification testing standards. In addition to these microphones, the University of Maryland set up seven ground-board microphones: five collocated with the Bell certification microphone positions and one microphone approximately 50 meters to each side of the centerline microphone in Bell's array. (Fig. 41)   The additional two locations used in the University of Maryland array were designed in order to provide good coverage of the acoustic hemisphere for both straight-line and turning flight trajectories, as developed in sections 2.5 and 6.1.3, respectively. These ground board microphones were configured similarly to those provided by NASA Langley in 2006, except larger 2 x 2 foot plywood ground boards were employed.

The in-flight microphone array was not utilized for this flight test program so that the drag of the helicopter would be representative of a typical Bell 206.   The air data boom was retained; however one additional microphone was added to the end of the boom for in-flight noise monitoring. The in-flight guidance and position tracking system were retained as well as an improved version of the optical tip-path plane tracking system.

Weather data was collected from a ground based metrology system offering temperature, pressure, humidity, and wind velocity information throughout each flight. However, due to airspace restrictions, it was not possible to launch an above ground balloon system, preventing the measurement of temperature and wind gradients.
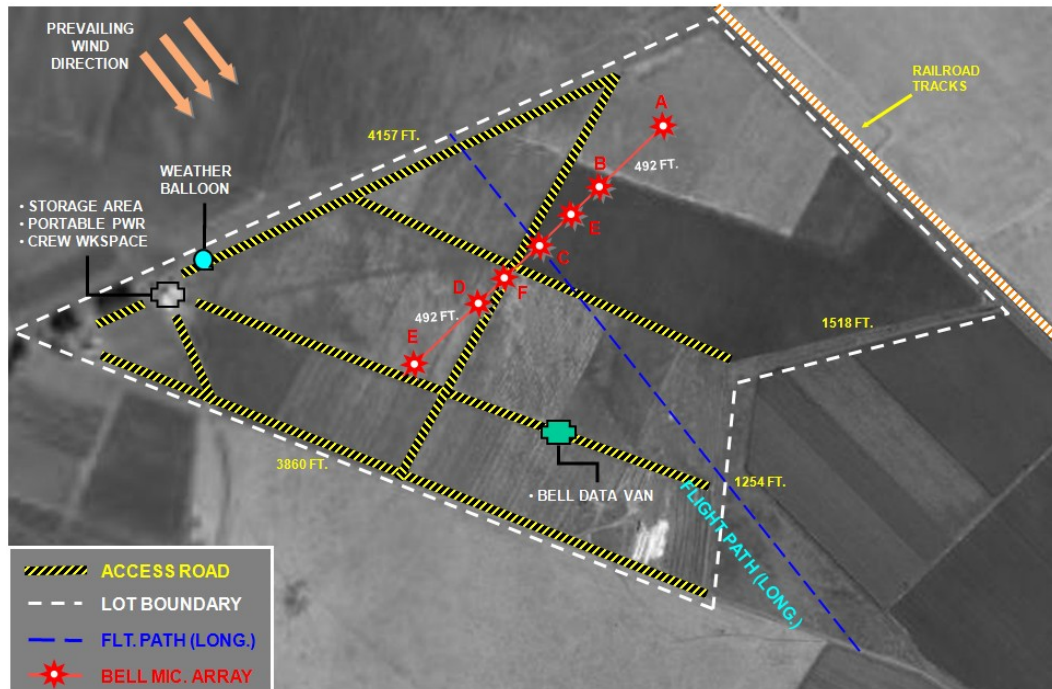
Figure 41: 2007 Flight Test Campaign Site Layout

Some complications arose during the 2007 campaign. The wired microphone array proved vulnerable to environmental damage, such as condensation between connections and severed cables from nearby jackrabbits. Unfortunately, data acquisition system used by Bell was not configured to allow immediate review of noise measurements. During post-test analysis of the data, some microphones positions yielded no or poor quality signals on certain test days.   Additionally, trajectory and microphone spacing requirements imposed by the FAA noise certification test specification resulted in less evenly spaced coverage of the noise hemisphere than for the 2006 array.

Consequently, in order to produce noise hemispheres with sufficient angular coverage, it was necessary to incorporate measurements from the FAA 1.2 meter noise certification microphones alongside the UMD ground board microphones.   Since these microphones were located above the ground plane, they were susceptible to interference

from ground reflections. A ground reflection correction scheme was implemented in this

thesis to correct for this effect, and is described fully in Appendix E.

4.2 In-Flight Noise Assessment

Blade-Vortex Interaction Sound Pressure Levels (BVISPL), measured from the

microphone located underneath the advanced blade tip on the 2006 in-flight measurement

array are plotted in Figure 42. The BVISPL include only noise measured from between

the 6th and 40th harmonics of the main rotor blade passage frequency, and are time-
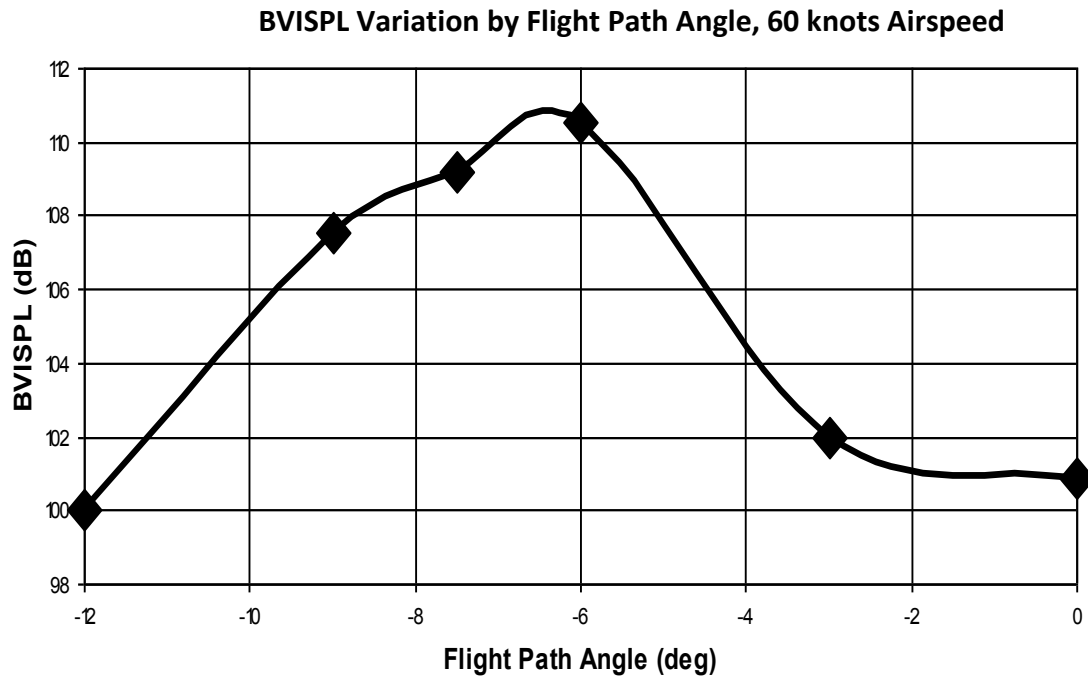
Figure 42: In-Flight Measurement of BVISPL Variation by Descent Rate

averaged on the main-rotor period in order to remove the influence of the tail rotor noise.

The measured peak noise levels correspond to the estimated zero overall inflow condition

for this helicopter with the in-flight measurement array affixed. It is important to note

that for this test setup, the in-flight measurement microphones are affixed to the

helicopter through the use of an external boom structure – causing a significant increase in the effective flat plate area drag of the helicopter. The increased drag over the clean configuration requires that the rotor tip path plane tilt farther forward to maintain the same flight condition. As a result net inflow for the test configuration is higher than that for the clean configuration for a given flight state. Therefore, the helicopter as configured in 2006 must flight at a steeper descent rate in order to achieve the same inflow state as the clean configuration. In addition, it can be seen that for this configuration the BVI noise does not change significantly for small changes in flight path angle when flying at a low descent rate – the wake is far below the rotor for these conditions and has little influence on overall noise.

Chapter Five: The Development of Acoustic Hemispheres for Straight-Line Flight

The flight test procedures and RNM methodology described in this thesis were combined with the spherical spline RBF interpolation method developed in Chapter Three and applied to the 2007 flight test in order to generate new representations of the magnitude and directivity of noise radiation from the Bell 206B helicopter for straight-line flight conditions. Noise hemispheres were developed for the BVISPL noise metric at a distance of thirty feet from the conceptual compact source located at the rotor hub. In this thesis, a baseline 60kts airspeed case is evaluated over a range of descent angles. The resulting hemispheres are plotted on the following pages, Figures 43 through 48.

Peak BVISPL for the straight and level 60 kts airspeed case is 103 dB. (Fig. 43) As the descent angle increases, the noise levels increase until approximately a 4.5 degrees descent where the peak BVISPL of 109 dB is reached. (Fig. 45) Further increases in descent rate yield reductions in peak BVI noise levels (Fig. 46, 47, 48). In addition to affecting the magnitude of BVI noise, the change in descent angle leads to a shift in the directivity of BVI noise radiation. At the shallower descent angles, the BVISPL "hotspot" is oriented in front of and below the helicopter. Beyond the peak BVISPL descent angle of 4.5 degrees, the directivity of BVI noise shifts towards the advancing side. The data is consistent with Q-SAM predictions and the 2006 in-flight data presented previously – the reduced drag of the helicopter in the "clean" 2007 configuration leads to a shallower tip-path-plane angle of attack resulting in less inflow. The reduced inflow corresponds to a shallower descent rate required to achieve peak BVI noise levels. Table 1 lists peak values by descent rate.
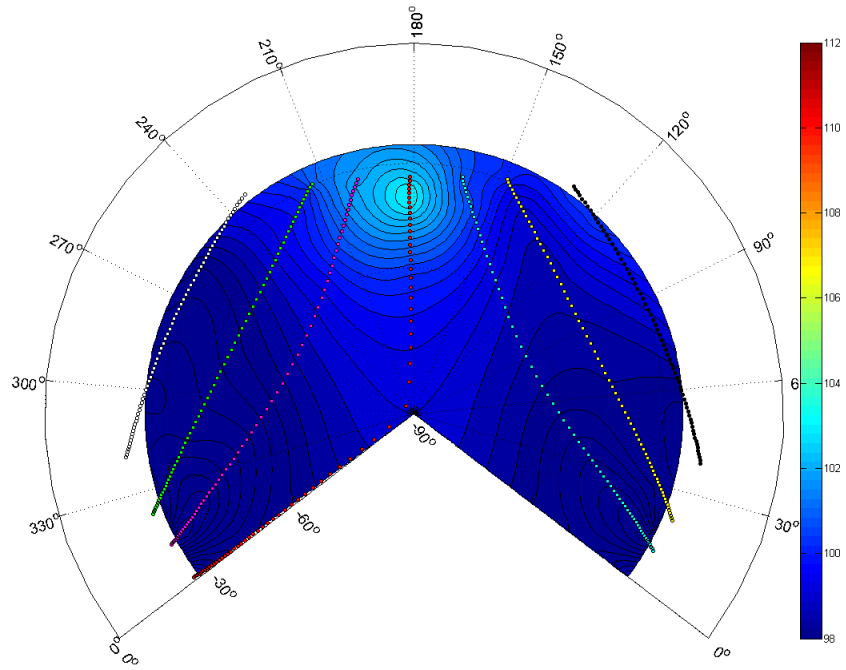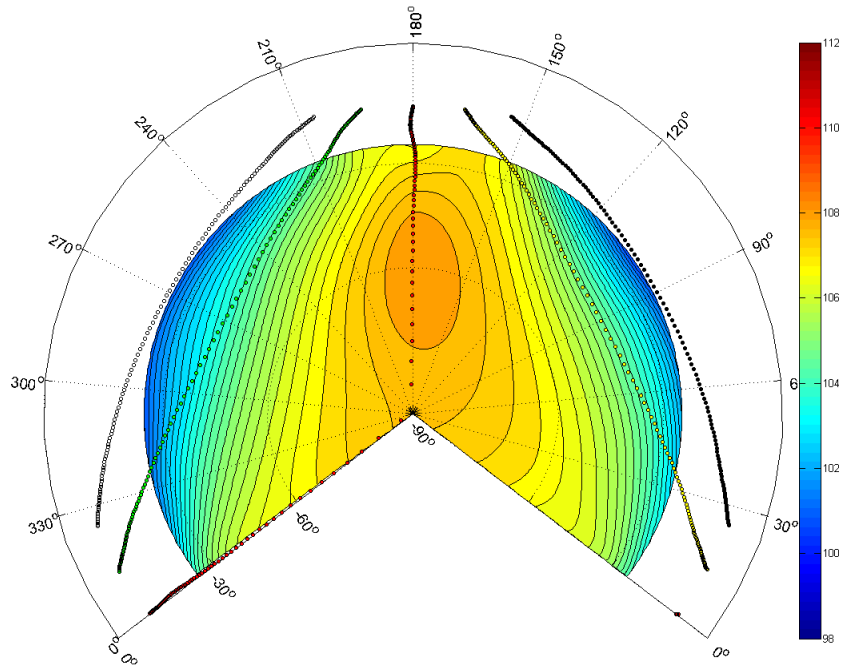
Figure 43: 60kts, Level Flight, dB BVISPL

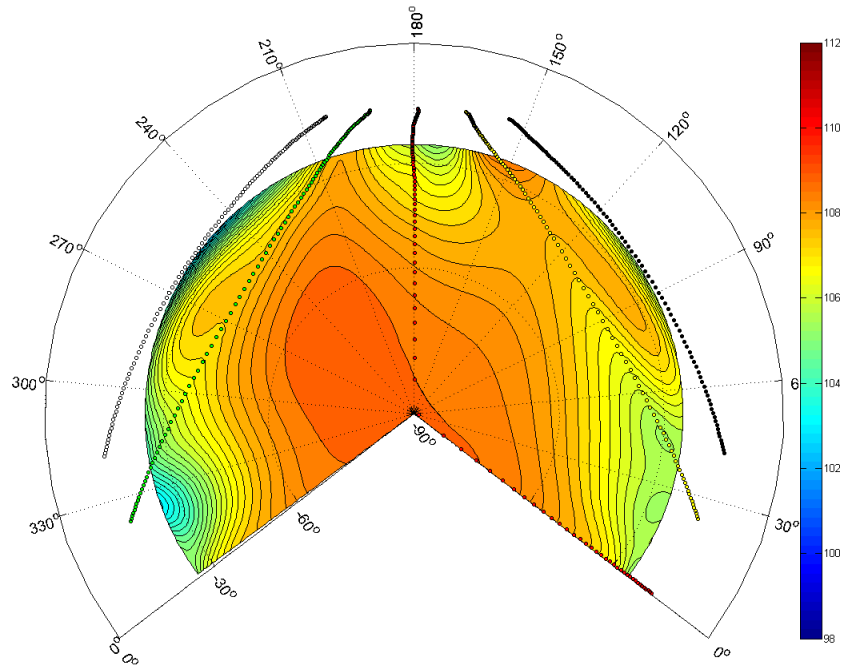**Figure 44: 60kts, 3 Degree Descent, dB BVISPL**

84

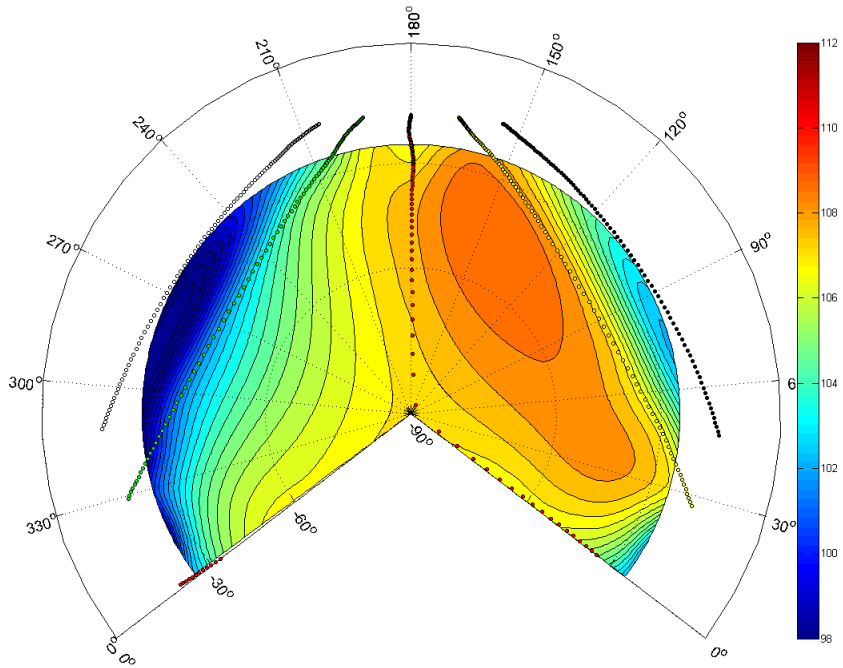**Figure 45: 60kts, 4.5 Degree Descent, Peak BVISPL Condition, dB BVISPL**
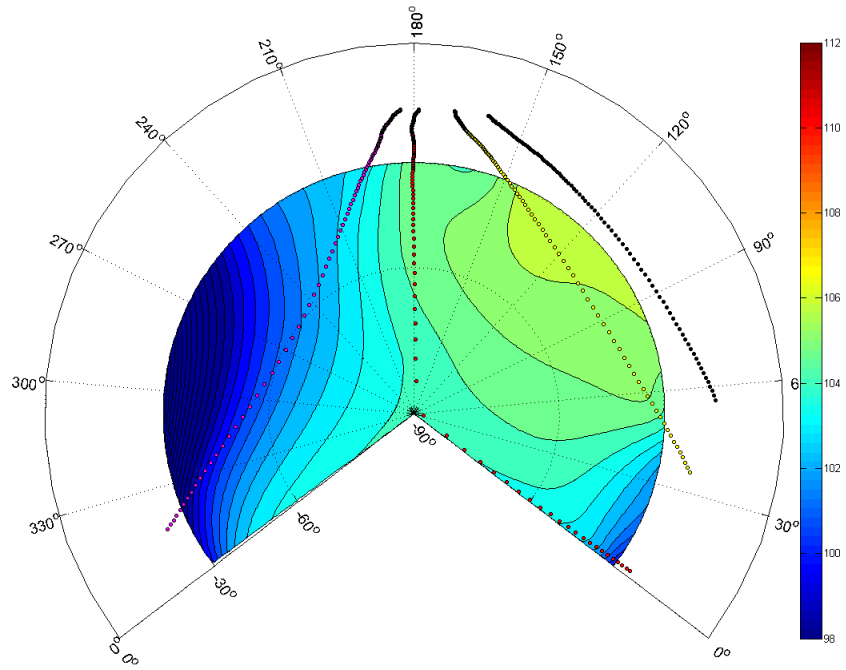

Figure 46: 60kts, 6 Degree Descent, dB BVISPL

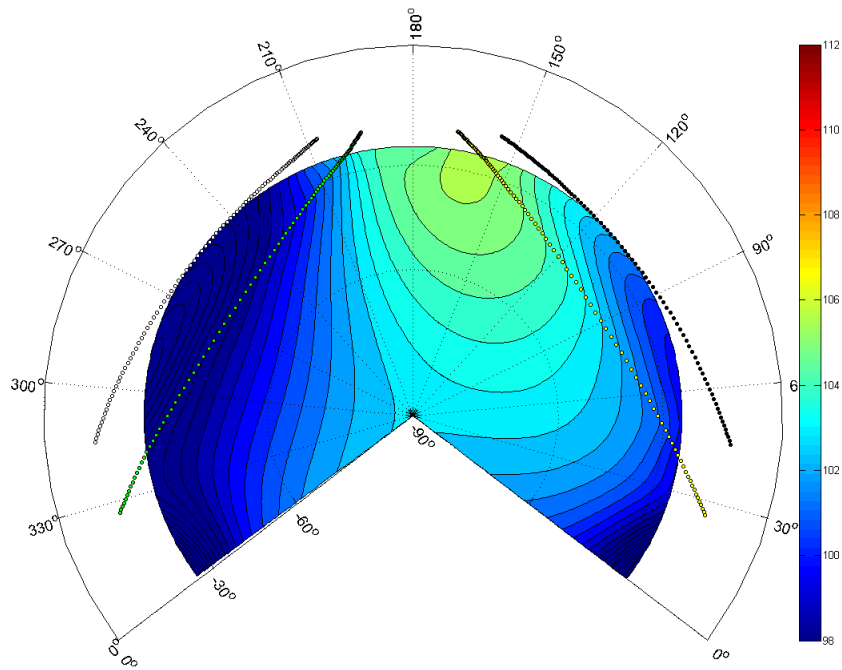**Figure 47: 60kts, 7.5 Degree Descent, dB BVISPL**

Figure 48: 60kts, 9 Degree Descent, dB BVISPL

86

Descent Angle	Peak BVISPL
0.0	103.0
3.0	107.5
4.5	108.5
6.0	107.5
7.5	106.0
9.0	105.0

Table 1: Peak BVISPL by Descent Angle, Straight-Line Flight

It is important to note that the Q-SAM technique is only applicable to BVI noise;
however the tail rotor blade passing frequency and its first several harmonics are within
the BVISPL frequency range for many helicopters, including the Bell 206B evaluated for
this thesis. It is therefore important to assess not only the BVISPL metric, but to look at
frequency spectra and pressure time-histories of the data to correctly identify the
dominant noise source for each flight condition.   In order to provide clear representations
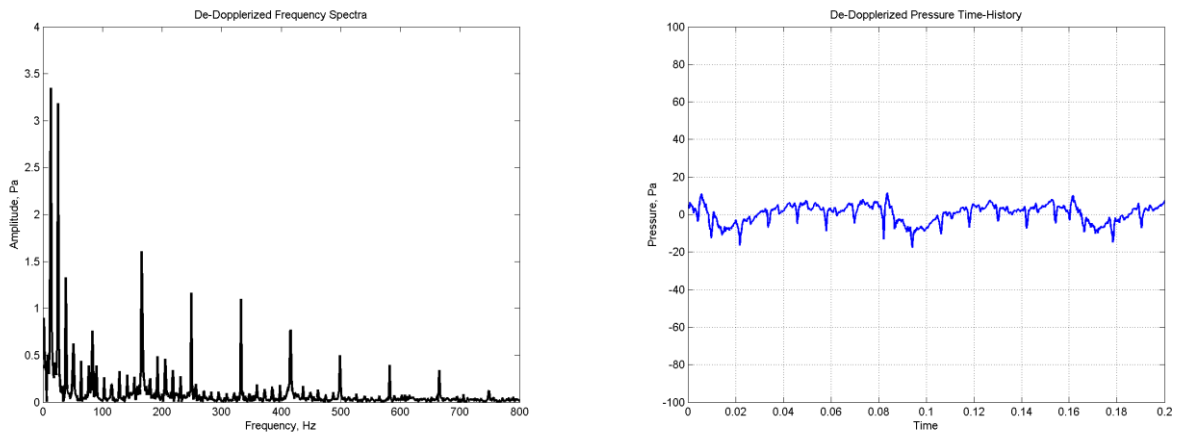of the frequency spectra and pressure time-history signals as they would appear on the

Figure 49: Straight-Line 60 kts Level Flight, Frequency Spectra and Pressure Time-History

surface of the acoustic radiation sphere, a time-domain de-Dopplerization scheme was developed and applied to the data. This scheme corrects for the temporal distortion of the acoustic waves deposited in the stationary medium by the moving source due to the motion of the source relative to the medium. By de-Dopplerizing the data in the time domain, noise radiated at harmonics of the main and tail rotor may be clearly identified in the frequency spectra. The details of this method are provided in Appendix D. During level flight, the tail rotor appears to dominate in the BVISPL frequency range (approximately 80-800 Hz). The tail rotor can be identified in the frequency spectra through the characteristic sharp amplitude peaks occurring at the tail rotor blade passing frequency and its harmonics. In the pressure time history, the tail rotor noise is identified by the sharp thickness noise pulses occurring at the tail rotor blade passing frequency. These plots are shown for the straight-line level flight case in Figure 49.

At the descent rates with peak observed noise levels, the characteristics of main rotor BVI noise predominate. BVI noise can be observed over a wide range of frequencies at multiples of the main rotor blade passing frequency. In the time domain, evidence of
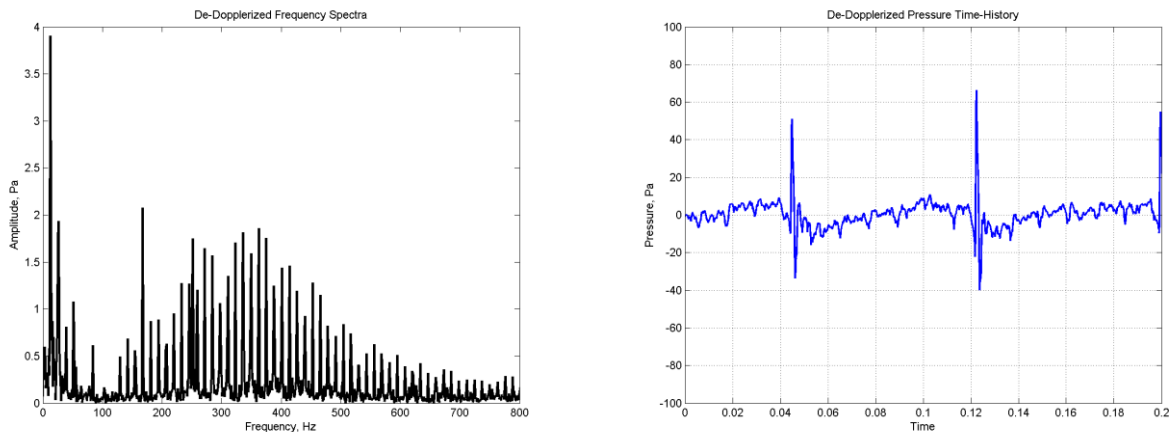

Figure 50: Straight-Line 4.5 Degree 60 kts Descent, Frequency Spectra and Pressure Time-History

BVI is seen in the strong impulses observed at the main rotor blade passing frequency. The 4.5 degree straight-line descent case is shown in Figure 50. Similar plots are included for all cases in Appendix C. In general, the importance of BVI noise increases as the peak BVI noise descent rate approaches. This is because the tail rotor thickness noise is largely independent of descent rate – where BVI noise does not exist, tail rotor noise dominates the BVISPL metric. However, when BVI noise occurs it tends to be significantly louder than the tail rotor. Additionally, tail rotor loading noise would be expected to decrease as the peak BVI descent rate is reached, since at the zero net inflow flight condition the main rotor torque is low, and little tail rotor trust is required to trim the helicopter.

In many of the cases with strong BVI noise, the presence of ground reflections is evident. The effects of ground reflection interference can be observed in the frequency domain as a harmonic shaping of pressure amplitudes by frequency. Additionally, this can be observed in the pressure time-history as a secondary BVI noise pulse following the first strong pulse after a brief time delay. The observed time delay can be compared to the time delay estimated using the ground reflection approach described in Appendix E of this thesis assuming the ground to be a perfect reflector. The results are tabulated in Table 2.

Table 2: BVI "Hotspot" Estimated and Observed Time-Delay of Reflections

Case	Elevation Angle	Estimated Time-Delay (ms)	Observed Time-Delay (ms)
Straight-Line Level	38.65°	4.5	4.5
Straight-Line 3°	58.00°	6.1	6.3
Straight-Line 4.5°	15.14°	1.9	2.0
Straight-Line 6°	28.72°	3.5	4.3
Straight-Line 7.5°	40.16°	4.7	5.0
Straight-Line 9°	22.00°	2.7	3.1

The estimated time-delay values are close to the observed time-delay for all cases, confirming the existence of ground reflections. The estimated time-delay values tend to be slightly shorter than the observed time-delay – this is most likely because the reactance of the ground has been neglected in the calculation of the time-delay estimate.

Chapter Six: Turning Flight

6.1 RNM Theory for Turning Flight

6.1.1 Steady Turning Flight

Real world turns can be broken down into three phases, a transient roll into the turn where the helicopter bank angle is increases, the steady portion of the turn where the bank angle is maintained, and a transient roll out of the turn where the bank angle decreases until it is again level with the horizon and the helicopter returns to straight-line flight. (Fig. 51)
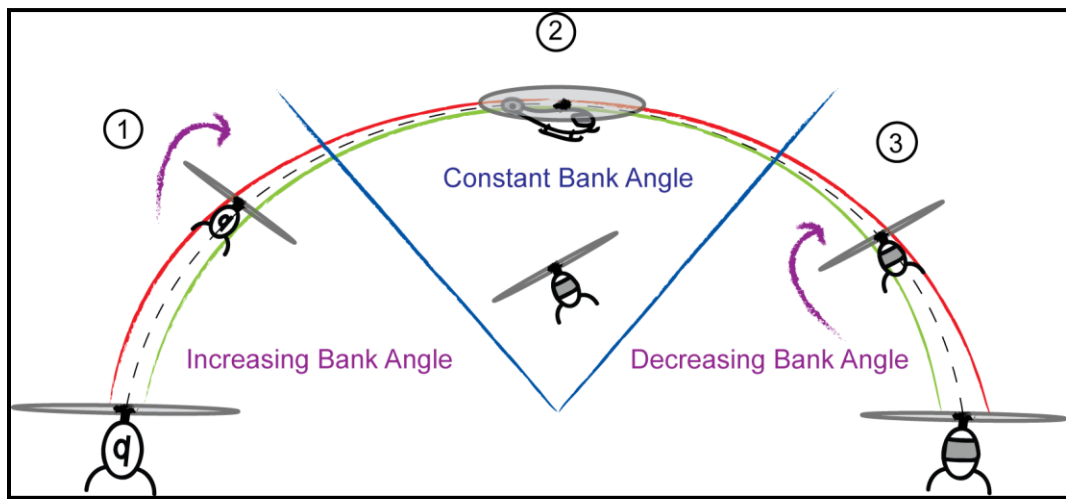

Figure 51: Three Stages of a Typical Turn

For typical commercial helicopter operations, turns will be performed at moderate speeds with low bank angles and will primarily consist of the steady constant bank angle segment of the turn. It is known that high roll rates during the transient phases of the turn can lead to large magnitudes of BVI noise – rapid maneuvers should be avoided in order to achieve quiet helicopter flight.

Recall that RNM constructs the acoustic hemisphere by making ground based microphone measurements across a range of directivity angles; however these measurements are made at different times and therefore the acoustic state of the helicopter must remain the same for the entire flight test run in order for the hemisphere to be representative of a single flight condition. Extending RNM to the construction of turning flight hemispheres requires that a steady flight condition is maintained throughout the test trajectory – airspeed, bank angle, and descent angle must be held constant. The resulting trajectory in no wind conditions is a helix, shown in Figure 52.
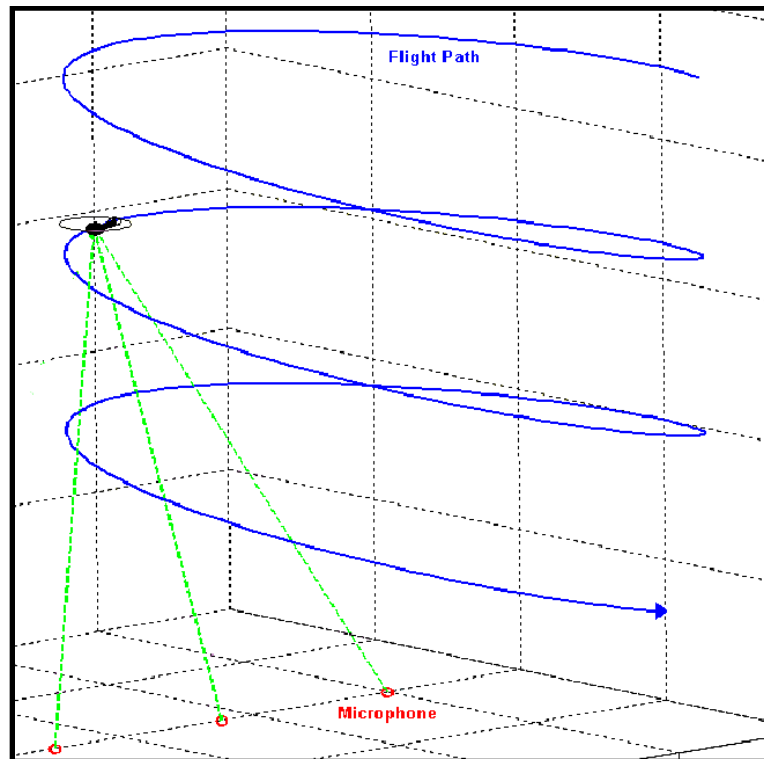
Figure 52: Helical Steady Turn

6.1.2 Sphere Selection

Currently, RNM handles turning flight by subdividing the turning into a number of short straight-line segments, selecting a straight-line acoustic sphere by airspeed and flight path angle, and tilting the directivity angles of the acoustic radiation sphere by the bank angle of the helicopter in the turn. This approach does not consider the affect turning flight has on the governing parameters of BVI. However, the RNM/Q-SAM method for sphere selection may be extended to describe how steady turning flight influences these governing parameters.
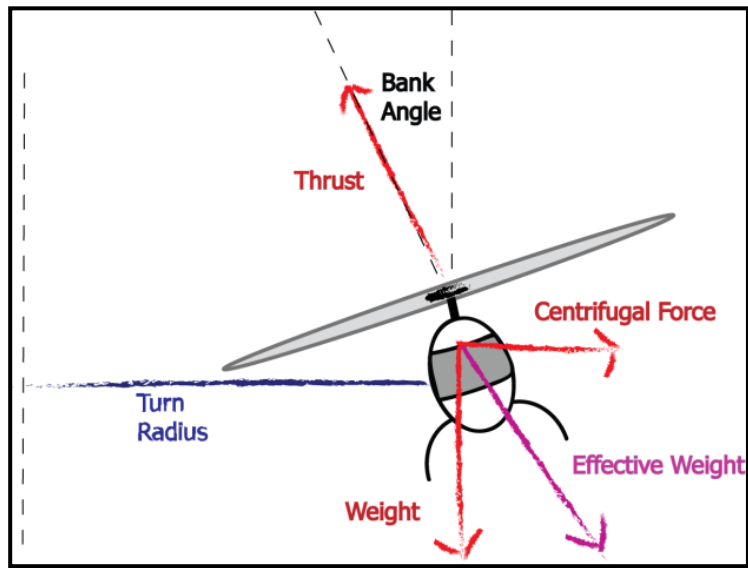
Figure 53: Lateral Force Balance

When a helicopter is in a steady turning flight condition, a new centrifugal inertial force is applied to the helicopter due to the centripetal acceleration experienced in a turn. This force must be opposed by banking the helicopter main rotor inwards. The vector sum of the helicopter weight and the centrifugal force can be thought of as the effective helicopter weight, W'. The longitudinal plane of the helicopter can now be defined as one containing the flight velocity vector and the effective weight vector. (Fig 53)   A longitudinal force balance, to first order and ignoring tail rotor forces, yields the extended Q-SAM relation:

$$\alpha_{TPP} = \left(-\frac{D_f}{W} - \gamma \right) \cos\phi - \frac{1}{g} a_x \qquad (21)$$

$$T = W \sec\phi; \qquad\qquad (22)$$

where, $\tan\phi = \dfrac{\dot{\psi}^2 s}{g}$.

Note that while α_{TPP} and γ are assumed to be small angles, bank angle ϕ is not. Appendix A contains a more detailed derivation of the above equations.

Compared to longitudinal flight, when the helicopter is undergoing a turn, the thrust will increase in order to balance the outward centrifugal force produced by turning. An increase in thrust changes BVI noise levels directly though a corresponding increase in vortex strength. However, an increase in thrust also yields an increase in the inflow through the rotor. Changes in thrust and tip-path-plane angle result in a change in inflow which changes the "miss distance" between the wake and the rotor - hence changing BVI noise levels. Since the noise generated by the helicopter is due to the interaction between the main rotor and the acoustic medium, the directivity of noise radiated by the main rotor is assumed to rotate along with the main rotor tip-path plane.
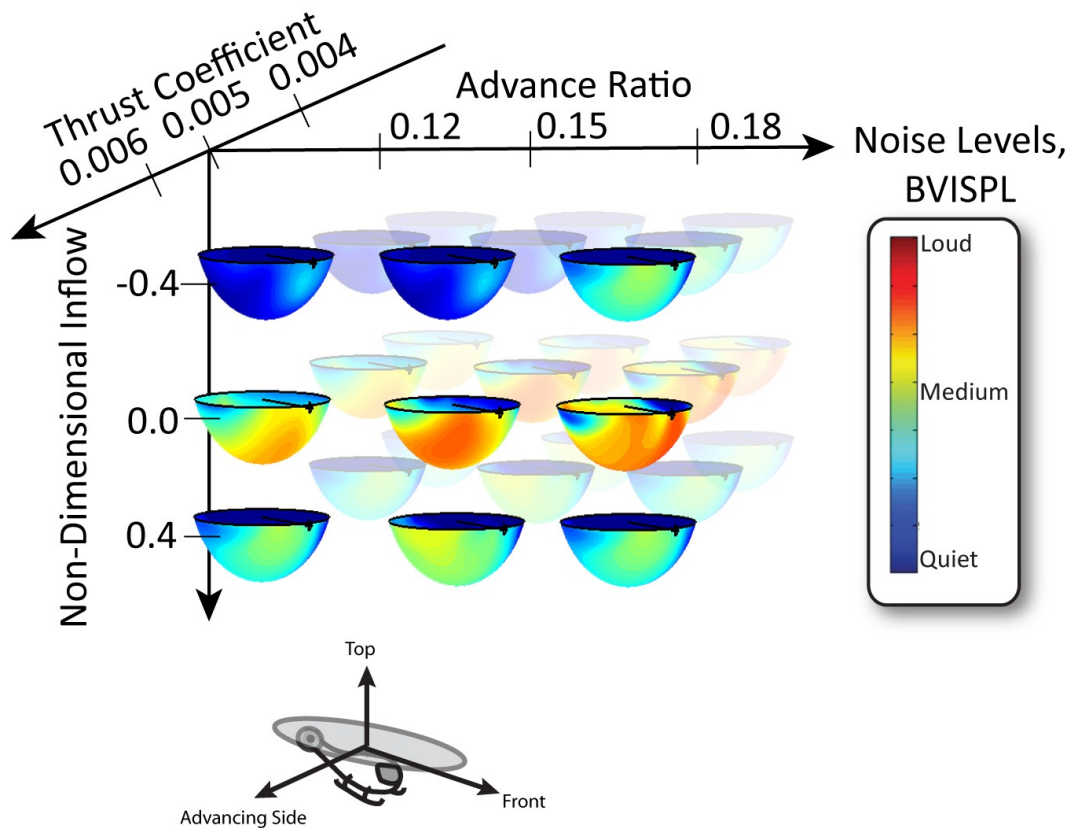
Figure 54: Sphere Selection in RNM/Q-SAM Extended to Turning Flight

Sphere selection using RNM/Q-SAM extended to turning flight therefore requires the use of three of the four governing non-dimensional parameters of BVI: advance ratio, inflow, and thrust coefficient. (Figure 54) As for the straight-line flight case, hover tip Mach number may be assumed constant given constant rotor RPM and atmospheric conditions. The thrust coefficient may be directly measured, calculated from performance data, or determined through direct measurement of the main rotor tip-path-plane bank angle given knowledge of the helicopter gross weight.

A turn may also have additional effects not described by this model. The effective rotation rate of the blades will change during a turn and the blades will be effectively rotating faster during a left turn compared to straight flight, and slower in a right turn. This will have the effect of modifying BVI intersection locations for a given advance ratio compared to straight flight.

Effective Blade Rotation Rate:

$$\frac{\dot{\psi}_B}{\Omega} = 1 + \frac{\dot{\psi}}{\Omega}\cos\phi \qquad (23)$$

During a turn, the tip-path-plane rotation rates in pitch and roll can be estimated as below:

TPP Pitch Rate: $\qquad \dfrac{\dot{\theta}_{TPP}}{\Omega} = \dfrac{\dot{\psi}}{\Omega}\sin\phi \qquad (24)$

TPP Roll Rate: $\qquad \dfrac{\dot{\phi}_{TPP}}{\Omega} = \dfrac{\dot{\psi}}{\Omega}\alpha_{TPP}\cos\phi \qquad (25)$

However, for steady moderate turns, these changes in tip-path-plane rates are small and their effects on the resulting aeroacoustics is secondary. For a relatively aggressive steady turn tested at 70 knots with a 38° bank, the non-dimensional tip-path-plane pitch and roll rates are 2.1×10^{-3} and 1.5×10^{-4}, respectively. Such pitch and roll rates would have the kinematical effect of changing vortex miss distance at the advancing side of the rotor disk by about 0.5% of the blade chord. Since the vortex core size is typically 10% to 30% of blade chord at the time of the BVI, the influence of these TPP rotation rates on BVI noise for these flight conditions can be safely neglected.

While RNM/Q-SAM has only been extended to steady turns, an initial effort at further extending Q-SAM for application to transient maneuvers has applied measurements of noise data during pitch-up and left and right rolling maneuvers in order to develop an empirical correction factor to the radiated noise levels measured for steady-state flight conditions. [23] At this time, the extended Q-SAM Prime methodology does not yet describe how transient maneuvers might affect the directivity of radiated noise. Further data is required across a range of directivity angles for a large set of maneuvers in order to expand and validate this method.

6.1.3 Trajectory and Array Design

As in the straight-line trajectory case, it is desirable for the helicopter to pass directly
above one microphone in the array, in order to capture measurements at directivity angles
beneath the helicopter. Since the helicopter will traverse through a complete circle,
noise propagated to the ground will be
radially symmetric about the axis of the
turn – therefore only a linear microphone
array is required to capture all azimuth
angles of the radiation sphere. However,
in turning flight the helicopter has the
ability to pass over the linear array
multiple times while still maintaining a
steady flight condition. By configuring the
helicopter flight trajectory such that a
second pass will approach nearby, but not
directly over, a second microphone on the
measurement array the sparseness of the
underside of the hemisphere may be
further reduced. Additionally, by
offsetting the center of the turn from the array,
a smaller set of microphones can cover a
larger range of elevation angles – since at
some points on the turn the helicopter will be far away from the array and at other it will
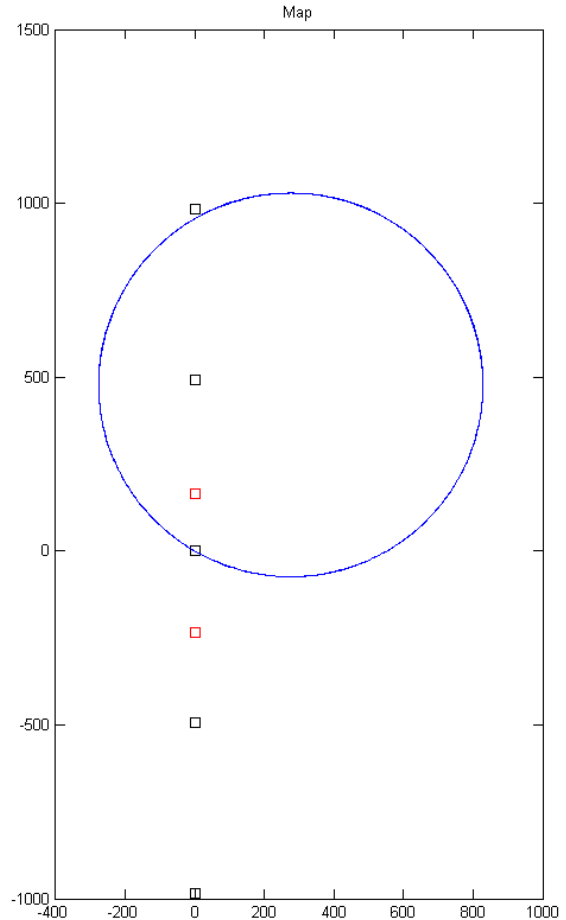be very close. Using these guidelines, level steady turning flight trajectories were

Figure 55: Proposed Steady Turn Top-View Geometry and Microphone Positions, Distances in Feet

98

generated which ensure good coverage of the hemisphere. The top-view of a typical

trajectory, with 60 knots airspeed and thirty degree right-hand bank angle is shown in

Figure 55. The locations of microphones composing the array are indicated by the square

markers. This offset trajectory results in the following distribution of measurements on
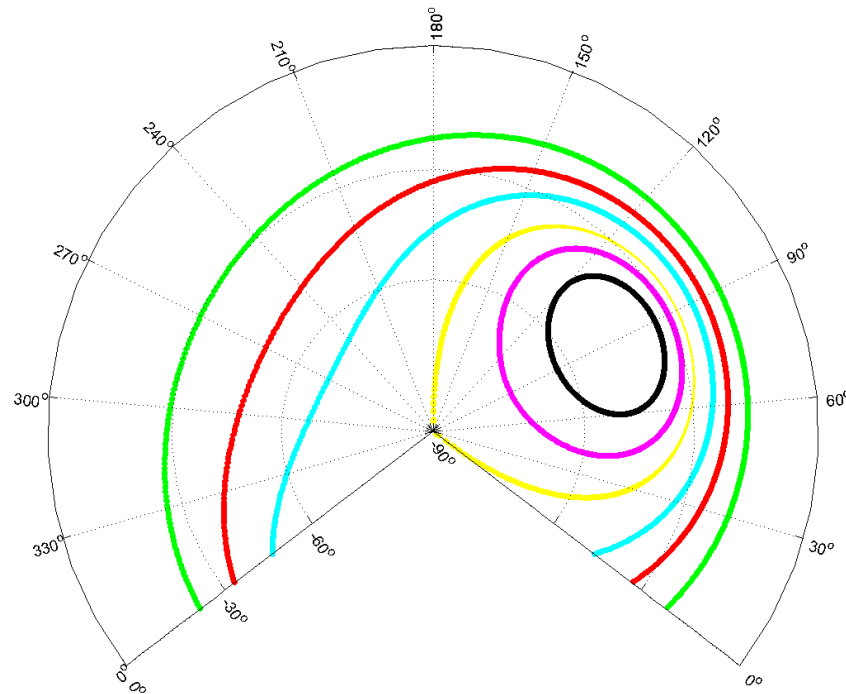
the horizon-fixed hemispherical surface. (Figure 56)

Figure 56: Distribution of Measurements on Acoustic Radiation Sphere, Proposed Steady Level Turn

Note that unlike in the straight-line flight trajectory case, the distribution of

measurement points on the sphere is no longer symmetrical. In addition, the left-hand

side of the hemisphere (on the outside of the turn) is sparser and does not cover as wide a

range of elevation angles. In an ideal case, each revolution of the level-flight turn results

in measurements which overlap those made during previous revolutions – in practice,

there will be some deviation from the prescribed trajectory.

The same array configuration is applied to a descending turn. Again, the trajectory is developed for an airspeed of 60 knots with a 30 degree right bank angle centered about the same point, however a six degree descent angle is also introduced. This yields the following distribution of measurements on the hemisphere. (Figure 57)
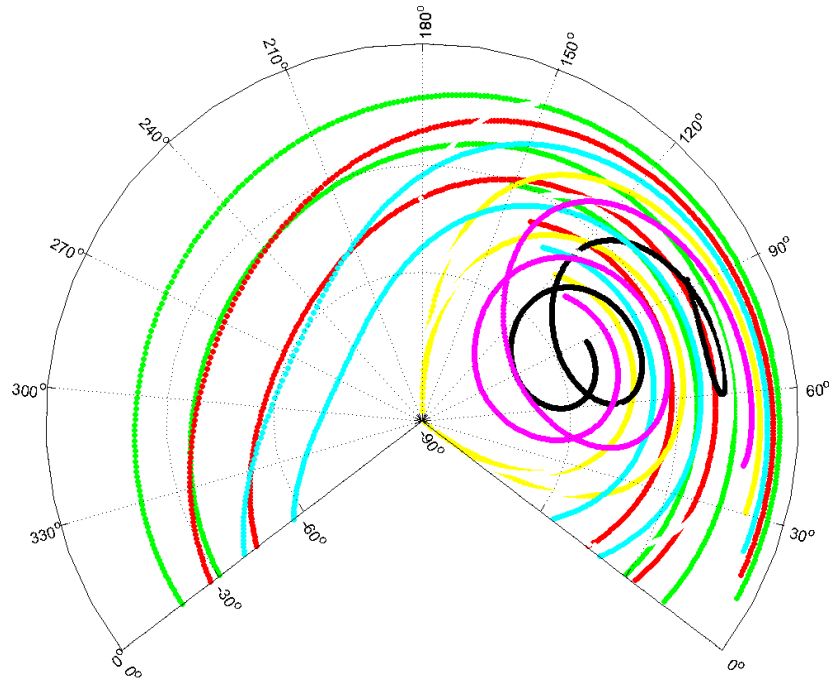

Figure 57: Distribution of Measurements on Acoustic Radiation Sphere, Proposed Steady Helical Turn

The resulting distribution of points on the hemisphere surface is more complex; however, overall sparseness is reduced since additional revolutions about the center of the turn cover increasingly shallower elevation angles. The "traces" of microphone measurements across the surface of the sphere are now able to cross one another. The interpolation scheme applied to this data must be able to handle the resulting asymmetrical, scattered and overlapping data distribution and produce meaningful and accurate results.

6.1.4 Interpolation

Ground measurements of steady turning flight trajectories produce larger numbers of data points distributed unevenly across the spherical surface. These properties further increase the computation time of radial basis function interpolation approaches, as well as produce even more poorly conditioned systems of equations resulting in increased instability. One method of improving the speed and stability of the interpolation problem is to perform a coarsening step before solving for the radial basis function weights. The coarsening procedure reduces the number of points of the scattered data and additionally reduces the unevenness of the distribution of data point across the sphere, resulting in a better conditioned coefficient matrix.

For straight-line flight, coarsening can be effectively performed by averaging the position and measured SPL of every few measurement points along each microphone trace. Since each microphone trace is spaced far from other traces across the sphere, this method evenly reduces the density of measurements over the entire domain.

The turning flight problem is more complicated, since microphone measurement traces are no longer evenly distributed across the spherical surface, and may intersect in many locations. A new method has been developed to coarsen the scattered data across the sphere. The geodesic distance between every pair of points on the hemisphere may be evaluated. The pair of points which are the smallest distance from each other may then be combined into a new point which lies at the average location and has the average value of the two points. This process is repeated until the minimum distance between any pair of points in above some threshold. In order to ensure a representative distribution of data, the averaging process used to combine pairs of points may be weighted by the

number of times each of the points in the pair has previously been combined. This method applies the most coarsening to areas of the hemisphere which have a high density of measurement points, and applies little to no coarsening where the data is already sparse. This process helps to improve the distribution of data across the sphere, resulting in a quicker and more stable radial basis interpolation.

Appendix F shows a comparison of the output from the interpolation schemes currently used in RNM with that of the new radial basis function scheme applied to one of the steady descending turn cases shown in Section 6.2. The RBF scheme is shown to be a good method for both straight-line and turning flight acoustic radiation hemispheres.

6.2 Turning Flight Sphere Results

The extensions to the RNM/Q-SAM method developed in this chapter were employed to collect and process steady-turning flight acoustic radiation hemispheres for the Bell 206B during the 2007 flight test program. As for the straight-line flight cases presented earlier, noise hemispheres were developed for the BVISPL noise metric at a distance of thirty feet from the conceptual compact source located at the rotor hub. Likewise, the cases presented in this thesis are all produced for an airspeed of 60 kts. Both left and right hand turns were performed with a turn radius of 552 ft, corresponding to a 30 degree bank angle for the 60 knot airspeed. Turns were performed across a range of descending flight path angles, in order to evaluate the effect of turns on BVI noise generation.

Three methods of flying the helical trajectories were attempted. The first method was to use the PPDG to provide active guidance throughout the turn to keep the pilot on

condition. However, this method was found to lead to excessive pilot control corrections and therefore an unsteady acoustic state violating the hemisphere generation assumptions. The next method attempted was to employ the PPDG to begin the turn, ensuring correct positioning of the trajectory relative to the microphone array, and then have the pilot attempt to manually hold bank angle, descent rate, and airspeed constant. While the results were steadier than the full PPDG control case, attempting to closely follow descent rate led to frequent collective pitch adjustments and some unsteadiness. The third method attempted was to again use the PPDG to begin the turn and to hold constant bank angle and airspeed. However, instead of attempting to hold descent rate constant, the pilot was instructed to maintain a constant rotor torque setting. Through some experimentation the torque setting required to maintain the desired flight path angle for each case was determined. This flight testing procedure led to the steadiest flight conditions with a minimum of undesired pilot control input.

The steady turning flight hemispheres are plotted on the following pages.   Note that the data used to generate the level right turn hemisphere (Fig. 58) was captured on a different day from the other turns, using the fully PPDG guided method of flying the trajectory – for this reason, the noise contours are somewhat less smooth than for the other cases. In particular, the peak BVISPL value of the hemisphere is 104 dB over a very small region with a solid angle on the hemisphere of less than a square degree. Outside of this small region, a peak BVISPL of 102 dB is observed over a broader region and is more representative of the peak BVISPL for a steady flight condition. As compared to the straight-line flight case, the BVI "hotspot" has shifted to the left hand side of the hemisphere. However, the hemisphere is defined as fixed to the horizon – the

directivity of the BVISPL "hotspot" has banked approximately 30 degrees along with the helicopter. Since the noise is radiated in front of and below the helicopter, when the helicopter banks towards the right during a turn, this corresponds to noise radiated towards the left side of the horizon-fixed radiation hemisphere. As in the level flight case, as the helicopter begins to descend, BVISPL levels increase. At a three degree descending flight path angle (Fig. 59) peak BVISPL levels within the "hotspot" have increased to 105.5 dB. An increase in descent angle to 6 degrees (Fig. 60) yields a substantial increase in peak BVISPL levels to 111.0 dB. A further increase in descent angle to 9 degrees (Fig. 61) also yields a BVISPL of 111.0 dB, although the "hotspot" covers a wider range of directivity than for the 6 degree case. This indicates that an even higher peak BVISPL might be achieved at a descent rate between 6 and 9 degrees for this helicopter. In all cases, the location of the BVISPL "hotspot" has been rotated by the 30-degree bank angle of the helicopter towards the left hand side of the radiation hemisphere.

The results are similar for left hand turns. The level and 3 degree descent rate cases (Fig. 62 and 63) show peak BVISPL levels which are the same as for the corresponding right hand turns, however the BVISPL "hotspot" is now on the right hand side of the horizon-fixed sphere, as expected for a left turning bank angle. However, peak BVISPL levels for the 6 and 9 degree left hand turn cases are 1.5 dB lower than those observed for the right hand turns. (Fig. 64, 65) Peak BVISPL levels are tabulated in Table 3.
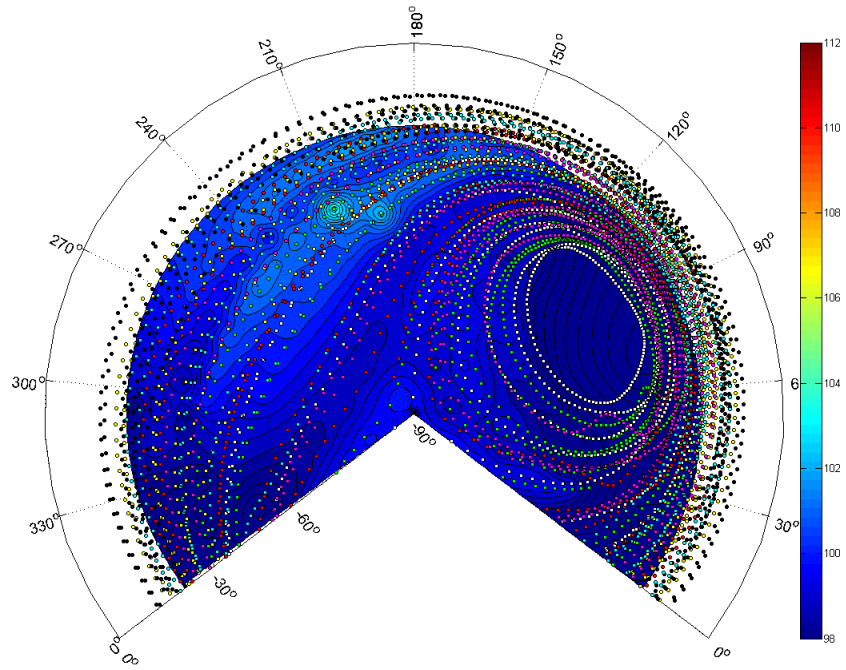
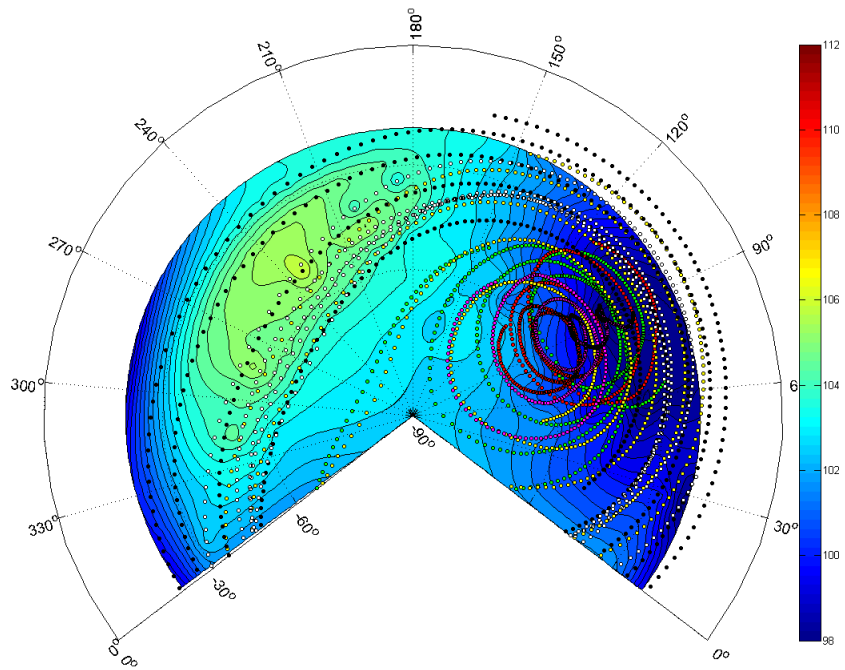**Figure 58: 60 kts, 30 Degree Bank, Level Right Turn, db BVISPL**

Figure 59: 60 kts, 30 Degree Bank, 3 Degree Descent Right Turn, db BVISPL
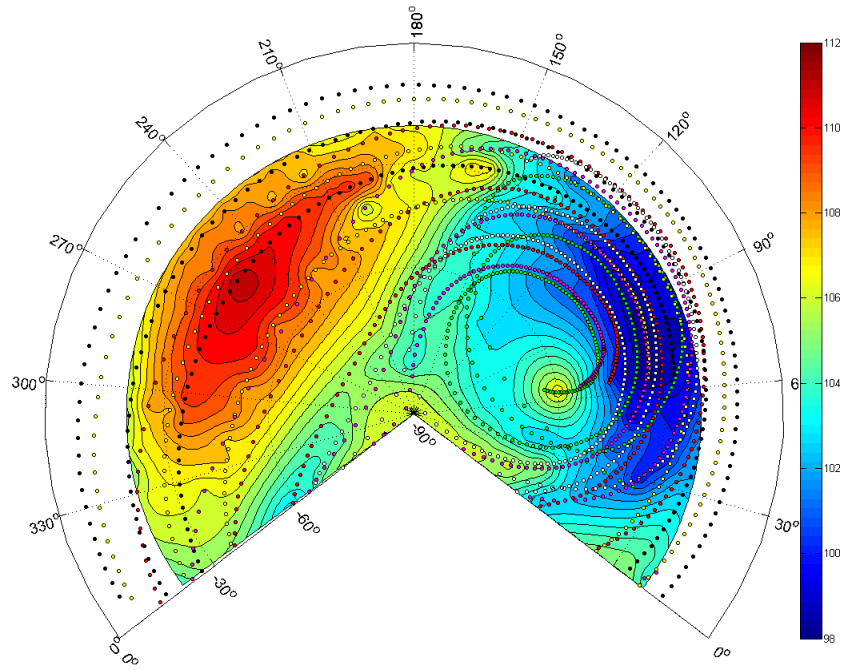
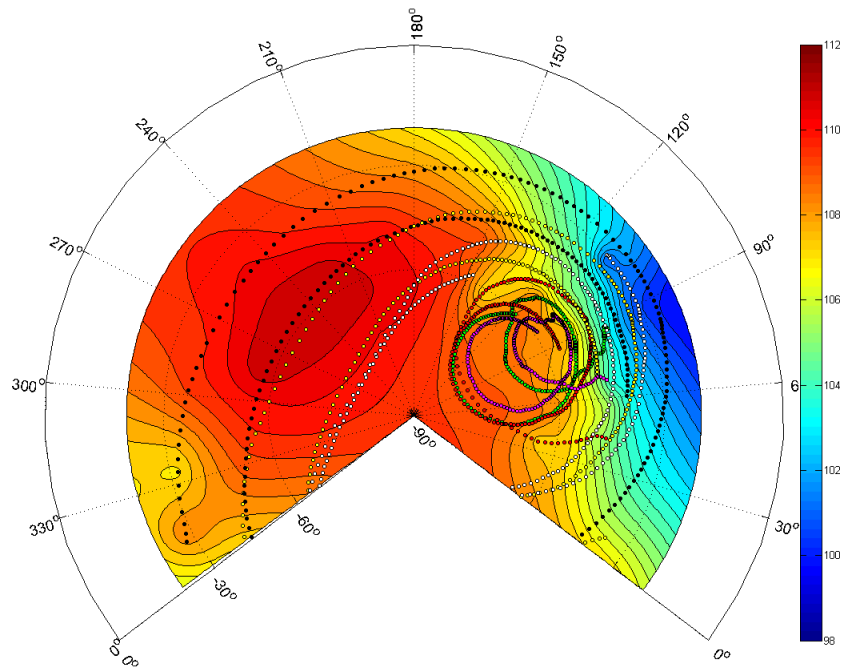**Figure 60:60 kts, 30 Degree Bank, 6 Degree Descent Right Turn, db BVISPL**

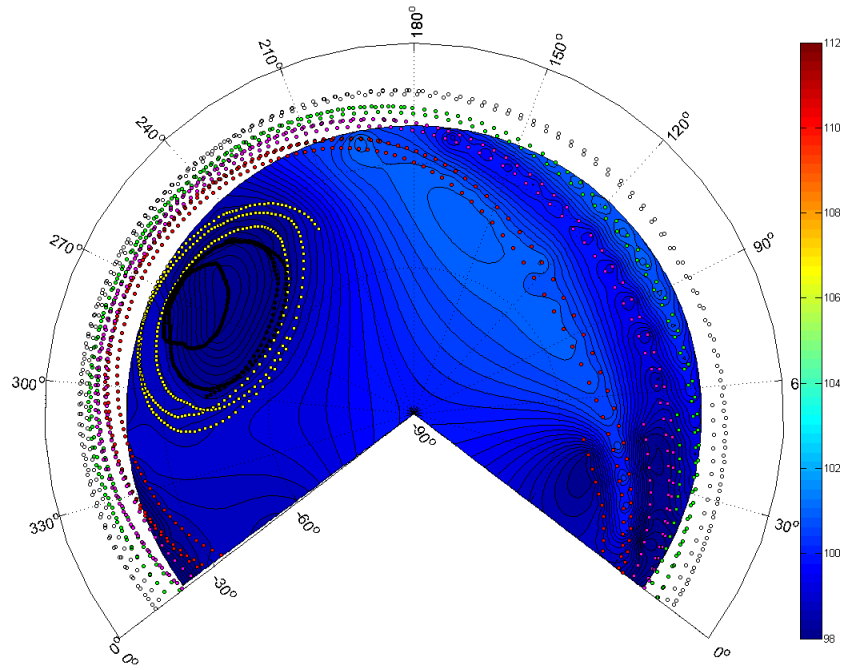**Figure 61: 60 kts, 30 Degree Bank, 9 Degree Descent Right Turn, db BVISPL**

106

Figure 62:60 kts, 30 Degree Bank, Level Left Turn, db BVISPL
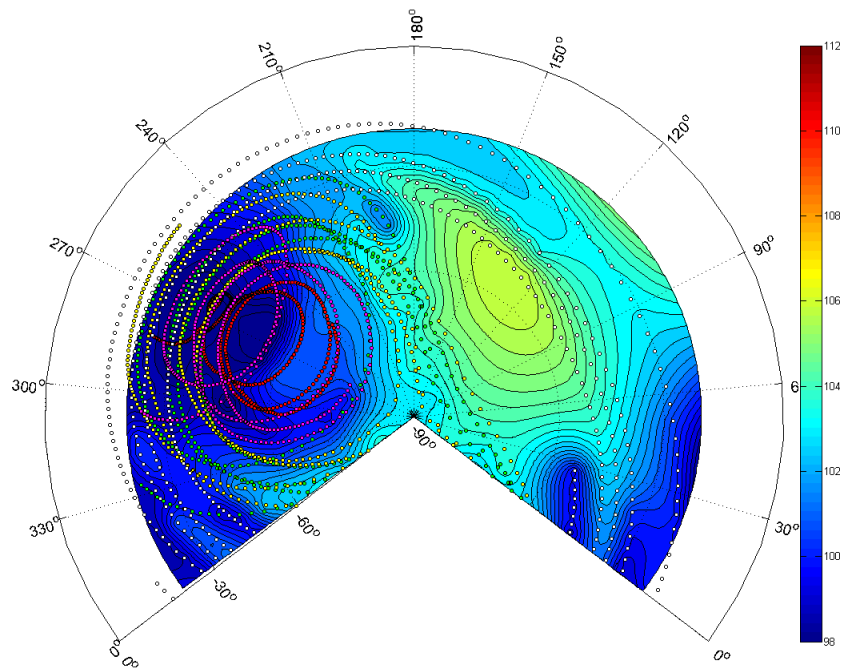

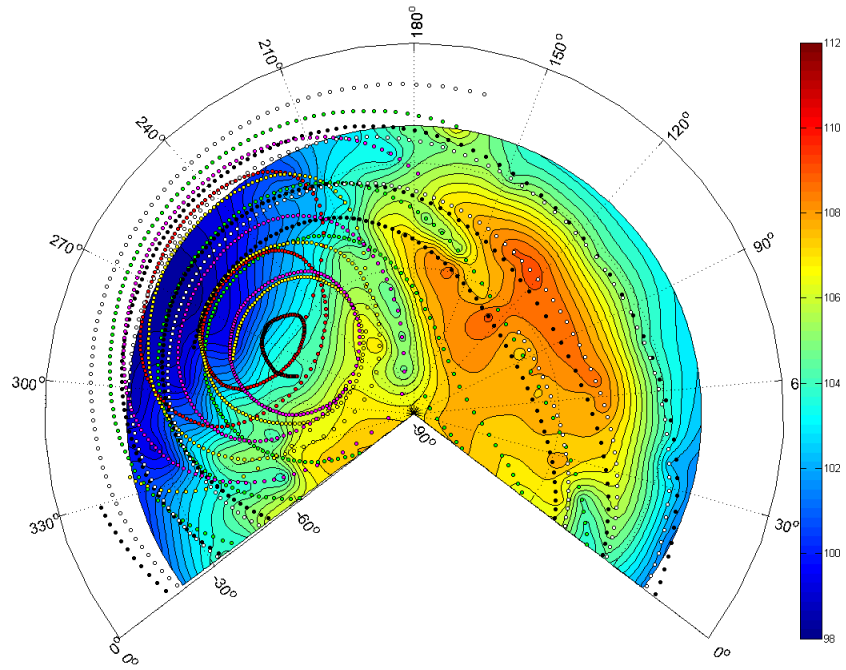**Figure 63: 60 kts, 30 Degree Bank, 3 Degree Descent Left Turn, db BVISPL**

107

Figure 64:60 kts, 30 Degree Bank, 6 Degree Descent Left Turn, db BVISPL
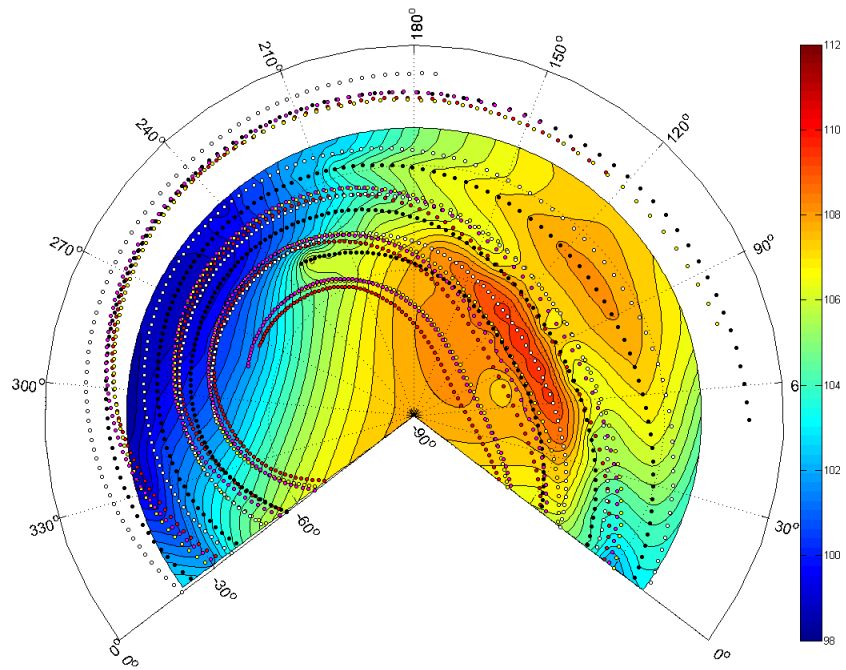

Figure 65:60 kts, 30 Degree Bank, 9 Degree Descent Left Turn, db BVISPL

Table 3: Peak BVISPL Levels During Steady Turn Maneuvers

Descent Angle	Peak BVISPL, Left Hand Turn	Peak BVISPL, Right Hand Turn
0.0	102.0	102.0
3.0	105.5	105.5
6.0	109.5	111.0
9.0	109.5	111.0

As predicted by the turning flight extension to the Q-SAM model, an increase in bank angle due to a turn yields an increase in thrust and therefore, an increase in inflow. In order to push the wake into the rotor disk, the helicopter must descend more quickly than for the straight line flight case. In addition, the increased thrust yields an increased tip vortex strength producing higher levels of BVI noise when the peak noise descent rate is achieved for the turning flight condition. In addition, for all cases the directivity pattern of the BVISPL peak appears to orient along with the bank angle of the helicopter, i.e. as the helicopter banks to the right the BVI noise is directed to the left by the equivalent bank angle. At low descent rates, there does not appear to be any significant differences between left and right hand turn noise levels. However, near the peak BVISPL descent angle, a slight increase in noise is observed for right hand turns model, where the advancing side of the rotor is inboard. This difference between left and right turns near the BVISPL peak is not accounted for by the extended Q-SAM model.
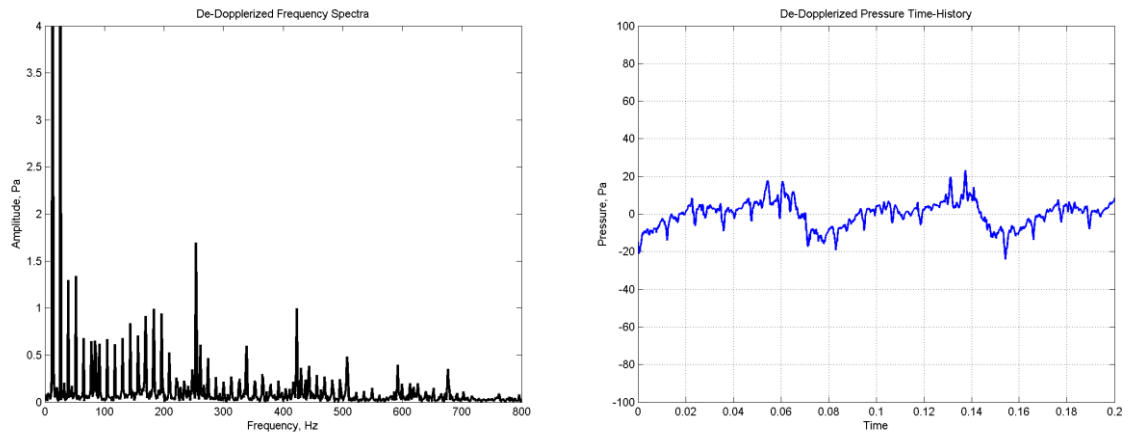
Figure 66: 30 Degree Left Banked 60 kts Level Turn , Frequency Spectra and Pressure Time-History
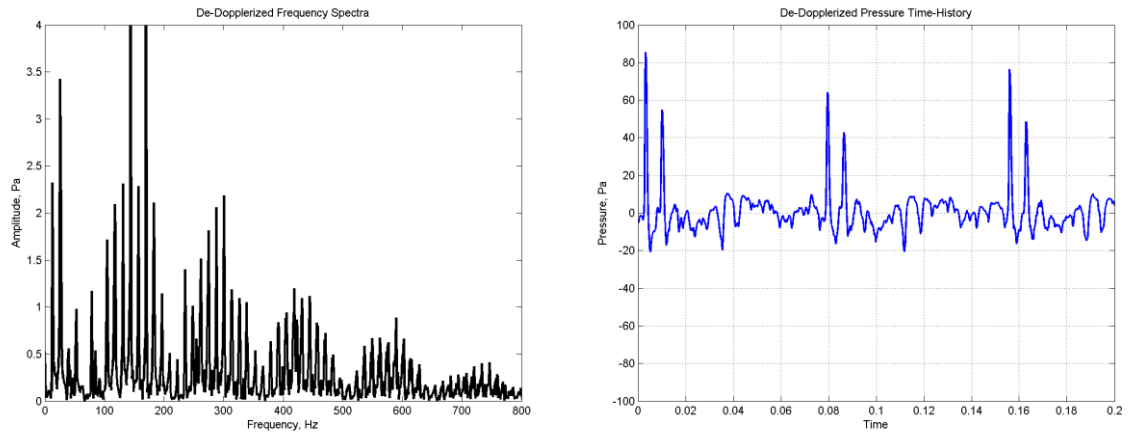

Figure 67: 30 Degree Left Banked 60 kts 9 Degree Descending Turn, Frequency Spectra and Pressure Time-History

The frequency spectra and pressure time histories of the ground noise measurements with directivity angles nearest the BVISPL "hotspot" on the sphere were examined for the turning flight cases, as well. Tail rotor noise was again found to be dominant for level flight conditions (Fig. 66); however as the descent rate increases BVI noise dominates. (Fig. 67)
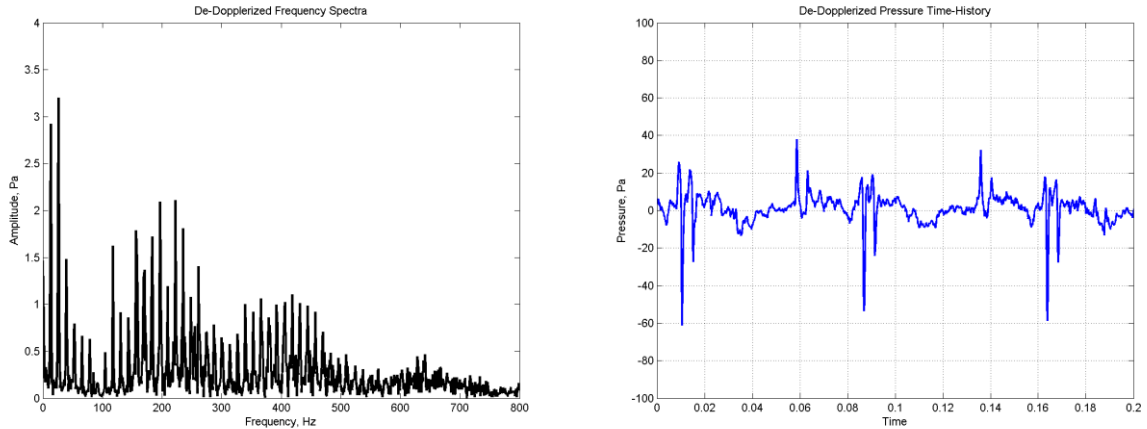
Figure 68: 30 Degree Right Banked 60 kts Level Turn , Frequency Spectra and Pressure Time-History

A closer examination of the unsteady peak of the fully PPDG guided right hand level flight turn indicates the presence of BVI caused by the undesired pilot control inputs due to the guidance system instructing the pilot to closely follow the prescribed trajectory in space, without consideration towards maintaining a steady flight condition. (Fig.68)

Table 4: BVI "Hotspot" Estimated and Observed Time-Delay of Reflections

Case	Elevation Angle	Estimated Time-Delay (ms)	Observed Time-Delay (ms)
Left Turn Level	37.04°	4.4	6.3
Left Turn 3°	23.45°	2.9	3.4
Left Turn 6°	47.48°	5.3	5.8
Left Turn 9°	62.54°	6.4	7.1
Right Turn Level	38.65°	4.5	4.6
Right Turn 3°	39.83°	4.6	5.0
Right Turn 6°	34.49°	4.1	4.0
Right Turn 9°	62.77°	6.4	6.9

As for the straight-line flight cases, evidence of ground reflections was seen in the pressure time history data and compared well with the ground reflection correction time-delay estimates from the model derived in Appendix E. (Table 4)

Chapter Seven: Conclusions and Future Work

7.1 Conclusions

A practical method of characterizing the external noise radiation of helicopter for use in the generation of ground noise contours over a range of straight-line and turning steady flight conditions has been introduced in this thesis. This new method has been developed by extending the RNM methodology to a non-dimensional basis using the governing parameters of BVI noise for both straight and turning flight trajectories. The interpolation of ground microphone measurements across the surface of the acoustic hemisphere has been identified as critical factor in determining of the accuracy of the source noise model. Existing interpolation schemes have been reviewed and determined to offered inadequate levels of accuracy. A new interpolation scheme is advanced in this thesis which dramatically improves the accuracy of acoustic hemispheres describing the magnitude and directivity of the externally radiated noise of helicopters. Additionally, new flight test procedures have been developed in order to generate acoustic hemispheres from microphone measurements produced by the flight testing of helicopters in steady turning flight. The new methods and procedures developed in this thesis have been successfully applied to ground noise data collected in the flight testing of the Bell 206B helicopter. The resulting experimentally generated acoustic hemispheres confirm the dependency of BVI in steady turning flight on the non-dimensional governing parameters incorporated in the extended RNM/Q-SAM methodology developed in this thesis.

Helical steady turning flight trajectories have been developed in order to measure the effect of turns on BVI noise generation. By careful placement of the microphone array relative to the helical steady turning flight trajectory, it has been shown that a small

number of microphones may be used to achieve adequate coverage of the acoustic radiation sphere across a wide range of directivity angles.   By placing additional microphones further afield, it may be possible to measure noise closer to the plane of the horizon; however as the propagation distance increases the signal-to-noise ratio of the acoustic measurements decreases.

A new interpolation scheme has been developed in this thesis, in order to represent the scattered noise data on the hemisphere as continuous and physically accurate noise contours across a range of directivity angles. In order to overcome the distortion effects introduced by typically used planar interpolation methods for scattered data, a new spherical radial basis function approach to interpolating acoustic hemispheres was introduced. The stability of RBF methods was improved through the adaptation of a preconditioning scheme to spherical surfaces and the development of a method of coarsening the scattered data sites in order to improve the distribution of measurement points across the sphere.   The RBF method was compared to the traditional methods used previously in RNM by sampling points on simulated BVI noise hemispheres, and was found to provide a significantly more accurate representation of radiated noise. In addition, the specific choice of a spherical spline radial basis function was found to produce the most accurate results for typical BVI noise spheres.

The methods developed in this thesis were applied to data collected for the Bell 206B helicopter. Hemispheres were generated for both straight-line and turning steady flight across a range of descent angles. These results were consistent with the extension of the Q-SAM theory to steady turning flight developed in this thesis. Steady turning flight results in an increase in thrust over straight-line flight due to the centripetal acceleration

induced by the turn. This increase in thrust leads to an increase in main rotor inflow. This increase in inflow corresponds to a steeper descent angle required to reach a zero average inflow condition and therefore maximum BVI noise, as compared to a similar straight-line flight condition. Additionally, the peak noise levels during descent were higher for turning flight than for straight-line flight – this is because the increase in thrust causes an increase in the strength of the tip vortices and thus the blade-vortex interactions. The directivity of the BVI noise was found to bank by the same angle as the helicopter during the turn. No measureable difference between noise levels was found between left hand and right hand turns far away from the peak BVI noise descent rate. Near the peak BVI noise descent rate, the right hand (advancing side) turn was found to be slightly louder than the left hand (retreating side) turn. Steady turning flight does not cause large increases in BVI noise – the large noise increases seen during turns in previous research are most likely caused by transient maneuvers into and out of the turn and not the steady turning flight condition itself.

This thesis extends the RNM/Q-SAM method to accurately describe the BVI noise generated during all steady-flight conditions, enabling the generation of ground noise contours for realistic helicopter flight trajectories. This method extends the RNM methodology to non-dimensional basis for BVI noise which supports the inclusion of steady turning flight. The improved interpolation methods described in this thesis allow the collection of source noise data to be performed accurately with fewer microphones, reducing the cost of data collection. Additionally, the extension of Q-SAM to turning flight provides a means of adapting straight-line flight data to equivalent turning-flight data – reducing the number of runs required to characterize a particular helicopter.

Altogether, the advancements proposed in this thesis result in means of creating and analyzing helicopter externally radiated noise which can be immediately applied to the creation of useful and accurate ground noise contours across the range of typical helicopter low-noise mission profiles. This thesis also provides a starting point for a more dramatic advancement of the RNM methodology with the potential to allow the external noise radiation produced by any of the noise sources on the helicopter to be accurately modeled across the full range of possible atmospheric and flight conditions using a practical set of empirically generated data.

7.2 Recommendations for Future Work

Further improvements could be made to the method described in this thesis. RNM/Q-SAM only provides an analytical framework for assessing equivalent BVI noise states – while this is generally the most important mechanism of noise generation for helicopter operating around landing areas, mechanisms of assessing the change in other measured noise sources by flight condition must be developed. Methods must be developed in order to separate the contribution of each noise source to the overall helicopter noise radiation sphere, so that each noise source may be independently characterized and its governing parameters identified and modeled. This effort must also include a separation of noise sources associated with the main rotor from those associated with the tail rotor.

RNM must be further generalized in order to draw further acoustic equivalences between a small set of measured data and a wide range of simulated flight conditions, incorporating additional non-dimensional governing parameters for external noise. The effect of changes in rotor advancing tip Mach number on the various helicopter noise sources must be assessed. For example, RNM must be capable of modeling the effect of

changes rotorcraft noise radiation due to changes in atmospheric conditions, so that data collected under normal atmospheric conditions will still be applicable to the generation of noise contours in "hot and high" flight conditions.

Extending the RNM/Q-SAM method as proposed will allow physics-based analysis to be applied in order to extend the applicability of RNM to the generation of noise contours for any flight condition, without requiring a large and prohibitively expensive flight testing program for every helicopter for which ground noise contours are to be generated.

Appendix A: Development of Helicopter Inflow Model

A.1 Equations of Motion

An earth-fixed inertial coordinate system, XYZ, is established, where a "flat earth" is assumed and the Z vector is oriented along the direction of gravitational acceleration. (Fig. 69) Within this coordinate system is the helicopter, whose position is described by vector $\vec{A}$.
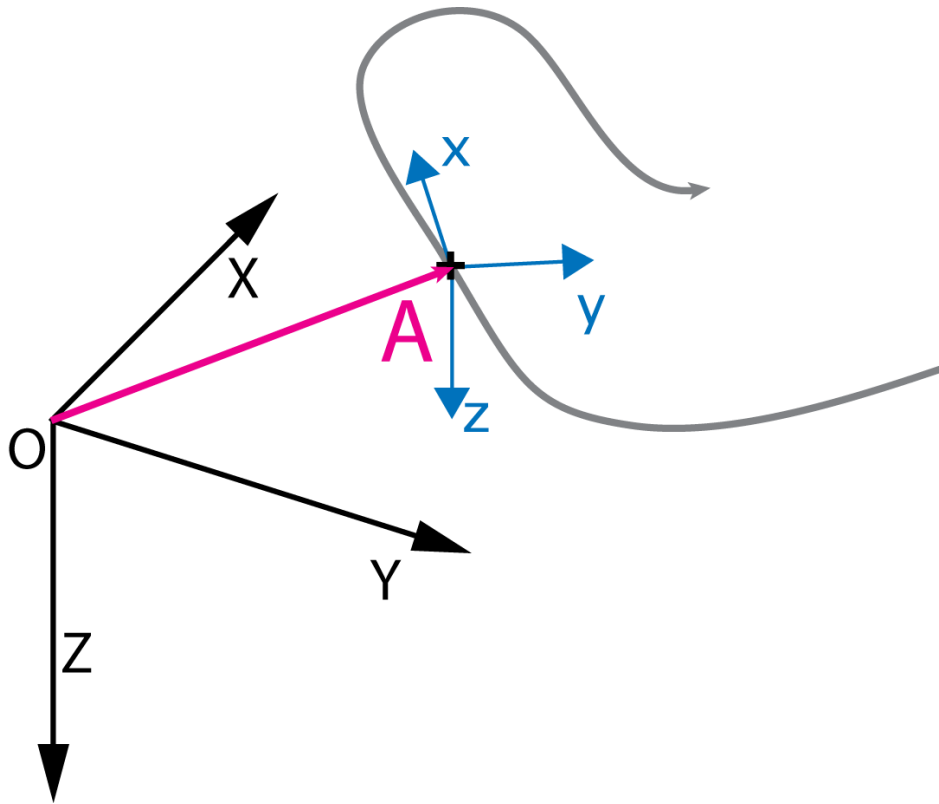
Figure 69: Arbitary Body A, in Motion

Newton's 2nd law for an elemental mass on the helicopter provides:

$$\delta \vec{F} = \delta m \frac{d\vec{v}}{dt} \qquad (26)$$

When the elements are summed over the body:

$$\sum \delta \vec{F} = \sum \delta m \frac{d\vec{v}}{dt} = \frac{d}{dt} \sum \vec{v} \, \delta m = \vec{F} \qquad (27)$$

The velocity of each element on the body is the center of mass of the body plus the time rate of change of the distance vector between the center of mass of the body and element (Fig. 70):

$$\vec{v} = \vec{v}_{CM} + \frac{d\vec{r}}{dt} \qquad (28)$$

$$\sum \vec{v} \, \delta m = m\vec{v}_{CM} + \frac{d}{dt} \sum \vec{r} \, \delta m \qquad (29)$$
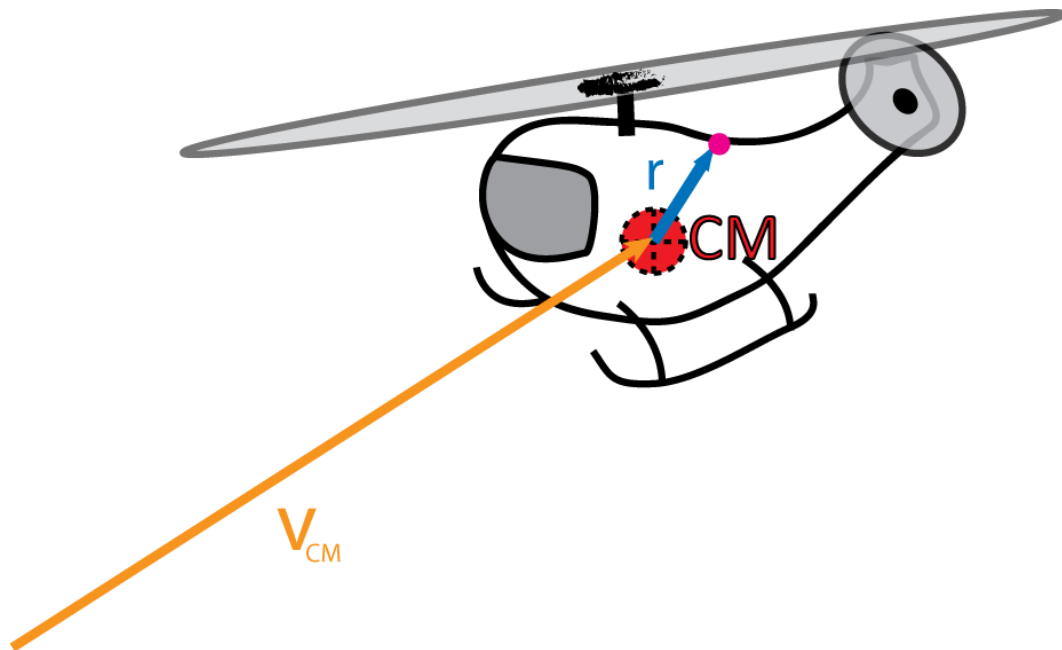

Figure 70: Helicopter Center of Mass Velocity Relation

However, when taken about the center of mass, $\sum \vec{r}\, \delta m = 0$, therefore Newton's law for the entire body is established as:

$$\vec{F} = m\frac{d\vec{v}_{CM}}{dt} \qquad (30)$$

Similarly, the angular momentum, $\delta\vec{h}$, of each element can be considered:

$$\frac{d}{dt}\left(\delta\vec{h}\right) = \frac{d}{dt}(\vec{r} \times \vec{v})\delta m = \frac{d\vec{r}}{dt} \times \vec{v}\delta m + \vec{r}\frac{d\vec{v}}{dt}\delta m \qquad (31)$$

Recalling that $\frac{d\vec{r}}{dt} = \vec{v} - \vec{v}_{CM}$, the moment of each element about the center of mass is described as:

$$\delta\vec{G} = \frac{d}{dt}\left(\delta\vec{h}\right) - (\vec{v} - \vec{v}_{CM}) \times \vec{v}\delta m = \frac{d}{dt}\left(\delta\vec{h}\right) + \vec{v}_{CM} \times \vec{v}\delta m \quad (32)$$

$$\sum \delta\vec{G} = \frac{d}{dt}\sum \delta\vec{h} + \vec{v}_{CM} \times \sum \vec{v}\delta m = \vec{G} \qquad (33)$$

Since the elements are summed about the center of mass, $\sum \vec{v}\delta m = 0$ therefore:

$$\vec{G} = \frac{d}{dt}\sum \delta\vec{h} = \frac{d\vec{h}}{dt} \qquad (34)$$

An additional coordinate system, xyz, can be established which is affixed to the center of mass of the helicopter, and aligned with the fuselage. The orientation of this coordinate system with respect to the stationary inertial coordinate system, XYZ, can be described through a sequence of three rotations of the Euler angles ψ, θ and φ which occur about sequentially about the body-fixed z, y, and x axes, respectively. (Fig.71)
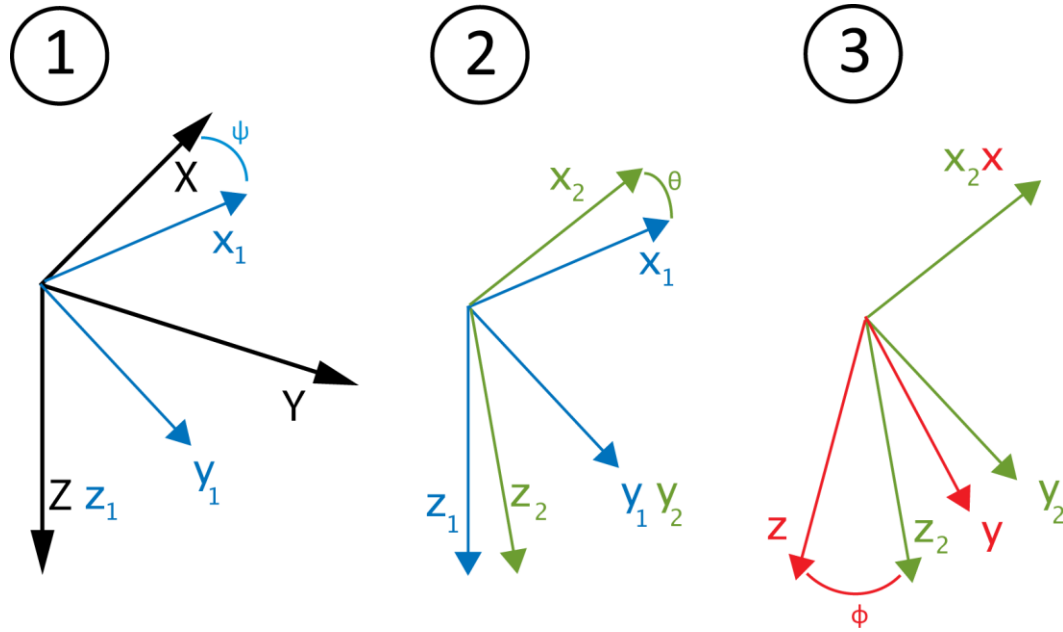
Figure 71: Euler Angle Transformation

The angular velocity of the helicopter and its affixed coordinate system can be described as:

$$\vec{\omega}_b = p\hat{\imath} + q\hat{\jmath} + r\hat{k} \qquad (35)$$

The velocity of any point on the rotating body can then be described as:

$$\vec{v} = \vec{v}_{CM} + \vec{\omega}_b \times \vec{r} \qquad (36)$$

Therefore, the angular momentum can be expressed as:

$$\vec{h} = \sum \vec{r} \times (\vec{v}_{CM} + \vec{\omega}_b \times \vec{r})\delta m = \sum \vec{r} \times \vec{v}_{CM}\delta m + \sum \vec{r} \times (\vec{\omega}_b \times \vec{r})\delta m \qquad (37)$$

Again, since $\sum \vec{r}\,\delta m = 0$ and $\vec{v}_{CM}$ is constant within the summation, $\sum \vec{r} \times (\vec{v}_{CM})\delta m = 0$

Therefore,

$$\vec{h} = \sum \vec{r} \times (\vec{\omega}_b \times \vec{r})\delta m = \vec{\omega}_b \sum r^2 \, \delta m - \sum \vec{r} \, (\vec{\omega}_b \cdot \vec{r})\delta m \qquad (38)$$

$$= \vec{\omega}_b \sum (r_x^2 + r_y^2 + r_z^2) \, \delta m - \sum \vec{r} \, (pr_x + qr_y + r \, r_z)\delta m \qquad (39)$$

Additionally, the angular momentum of the rotor, $\vec{h}'$ may be added to that of the body:

$$\vec{h} = \vec{\omega}_b \sum (r_x^2 + r_y^2 + r_z^2) \, \delta m - \sum \vec{r} \, (pr_x + qr_y + r \, r_z)\delta m + \vec{h}' \qquad (40)$$

Ultimately, it is most convenient to express the equations of motion with respect to the body of the aircraft, along the rotating and translating coordinate system xyz at A. Taking the derivative of A with respect to time yields:

$$\frac{d\vec{A}}{dt} = \frac{d\vec{A}_x}{dt}\hat{\imath} + \frac{d\vec{A}_y}{dt}\hat{\jmath} + \frac{d\vec{A}_z}{dt}\hat{k} + \vec{\omega}_b \times \vec{A} \qquad (41)$$

Evaluating the force and moment equations in this frame of reference then yields:

$$\vec{F} = m\frac{d\vec{v}_{CM}}{dt} + m\vec{\omega}_b \times \vec{v}_{CM} \qquad (42)$$

$$\vec{G} = \frac{d\vec{h}_x}{dt}\hat{\imath} + \frac{d\vec{h}_y}{dt}\hat{\jmath} + \frac{d\vec{h}_z}{dt}\hat{k} + \vec{\omega}_b \times \vec{h} \qquad (43)$$

These can also be expressed as scalar equations:

$$F_x = m(\dot{u} + qw - rv) \qquad (44)$$

$$F_y = m(\dot{v} + ru - pw) \qquad (45)$$

121

$$F_z = m(\dot{w} + pv - qu) \qquad (46)$$

$$L = \dot{h}_x + qh_z - rh_y \qquad (47)$$

$$M = \dot{h}_y + rh_x - ph_z \qquad (48)$$

$$N = \dot{h}_z + ph_y - qh_x \qquad (49)$$

Additionally, the Euler angle rates may be applied in order to calculate the aircraft pitch, roll, and yaw rates through the standard Euler rate transformation:

$$\vec{\omega}_b = \begin{bmatrix} p \\ q \\ r \end{bmatrix} = \begin{bmatrix} 1 & 0 & -\sin\theta \\ 0 & \cos\varphi & \cos\theta\sin\varphi \\ 1 & -\sin\varphi & \cos\theta\cos\varphi \end{bmatrix} \begin{bmatrix} \dot{\varphi} \\ \dot{\theta} \\ \dot{\psi} \end{bmatrix} \qquad (50)$$

If it is assumed that the rate of change of the Euler pitch and roll angles are negligible, than the yaw, pitch, and roll rates of the tip path plane can be estimated as follows:

$$r = \dot{\psi}\cos\varphi\cos\theta \,, q = \dot{\psi}\sin\varphi\cos\theta \,, p = \dot{\psi}\cos\varphi\sin\theta \qquad (51,52,53)$$

If the Euler pitch angle of the tip-path-plane is assumed small the following expressions for the rotation rates are found, non-dimensionalized against the angular speed of rotation of the main rotor:

$$r = \frac{\dot{\psi}}{\Omega}\cos\varphi \,, q = \frac{\dot{\psi}}{\Omega}\sin\varphi \,, p = \frac{\dot{\psi}}{\Omega}\theta\cos\varphi \qquad (54,55,56)$$

The applied forces F_x, F_y, and F_z are composed of the aerodynamic and gravitational forces. The gravitational forces along the body axis directions are dependent on the Euler rotation angles between the inertial frame XYZ and the body frame xyz such that:

$$F_x = X - mg \sin \theta \qquad (57)$$

$$F_y = Y + mg \cos \theta \sin \varphi \qquad (58)$$

$$F_z = Z + mg \cos \theta \cos \varphi \qquad (59)$$

A.2 Helicopter Aerodynamic Forces

The applied aerodynamic forces on the left hand side of the six equations of motion described in the previous section may be solved for through force and moment summation of the individual elements of the helicopter.[48]   Aerodynamic forces are produced by the helicopter main rotor, tail rotor, fuselage, and empennage.   It is convenient to evaluate the forces along the body axes of the helicopter and resolve them to the vehicle center of mass.

The longitudinal force balance is applied along the xz plane in order to evaluate the horizontal and vertical forces, as well as the pitching moment. (Fig. 72)
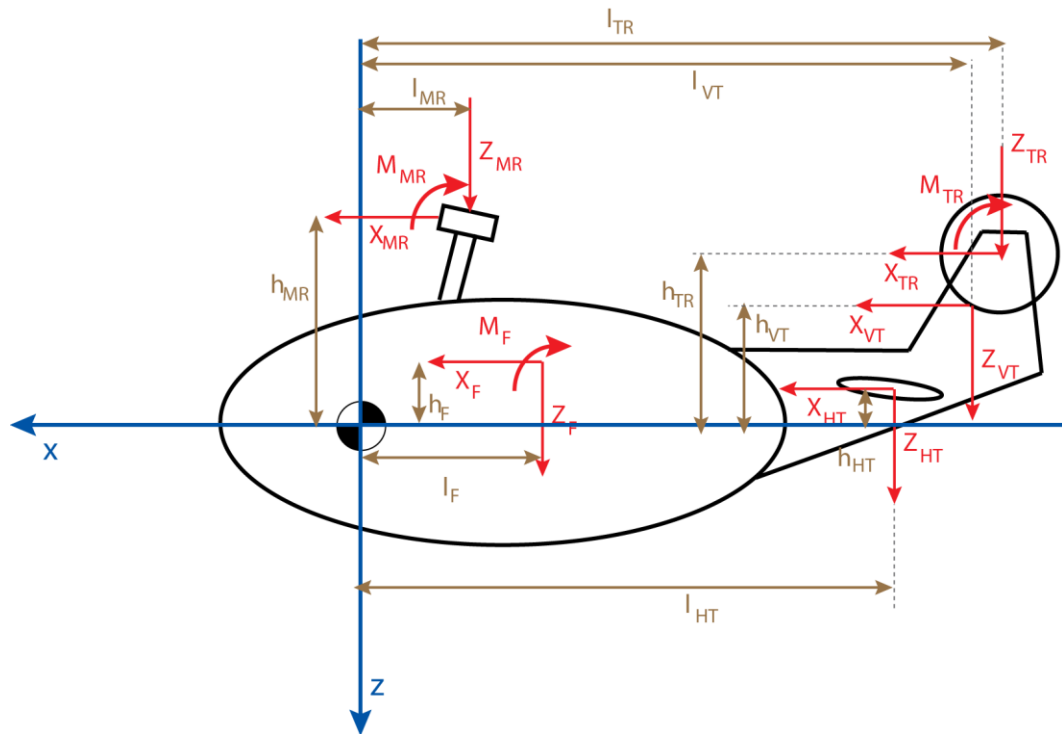
Figure 72: Longitudinal and Vertical Forces

The resultant forces along X and Z are then:

$$X = X_{MR} + X_{TR} + X_{HT} + X_{VT} + X_F \qquad (60)$$

$$Z = Z_{MR} + Z_{TR} + Z_{HT} + Z_{VT} + Z_F \qquad (61)$$

The pitching moment is dependant of the locations of the various components with respect to the center of mass, and can be calculated as:

$$M = M_{MR} - X_{MR}h_{MR} + Z_{MR}l_{MR} + M_{TR} - X_{TR}h_{TR} + Z_{TR}l_{TR} - X_{HT}h_{HT} + Z_{HT}l_{HT} -$$

$$X_{VT}h_{VT} + Z_{VT}l_{VT} + M_F - X_Fh_F + Z_Fl_F$$

$$(62)$$

Likewise, a rear-view free-body diagram of the helicopter may be used to evaluate the lateral forces and rolling moment. (Fig. 73)
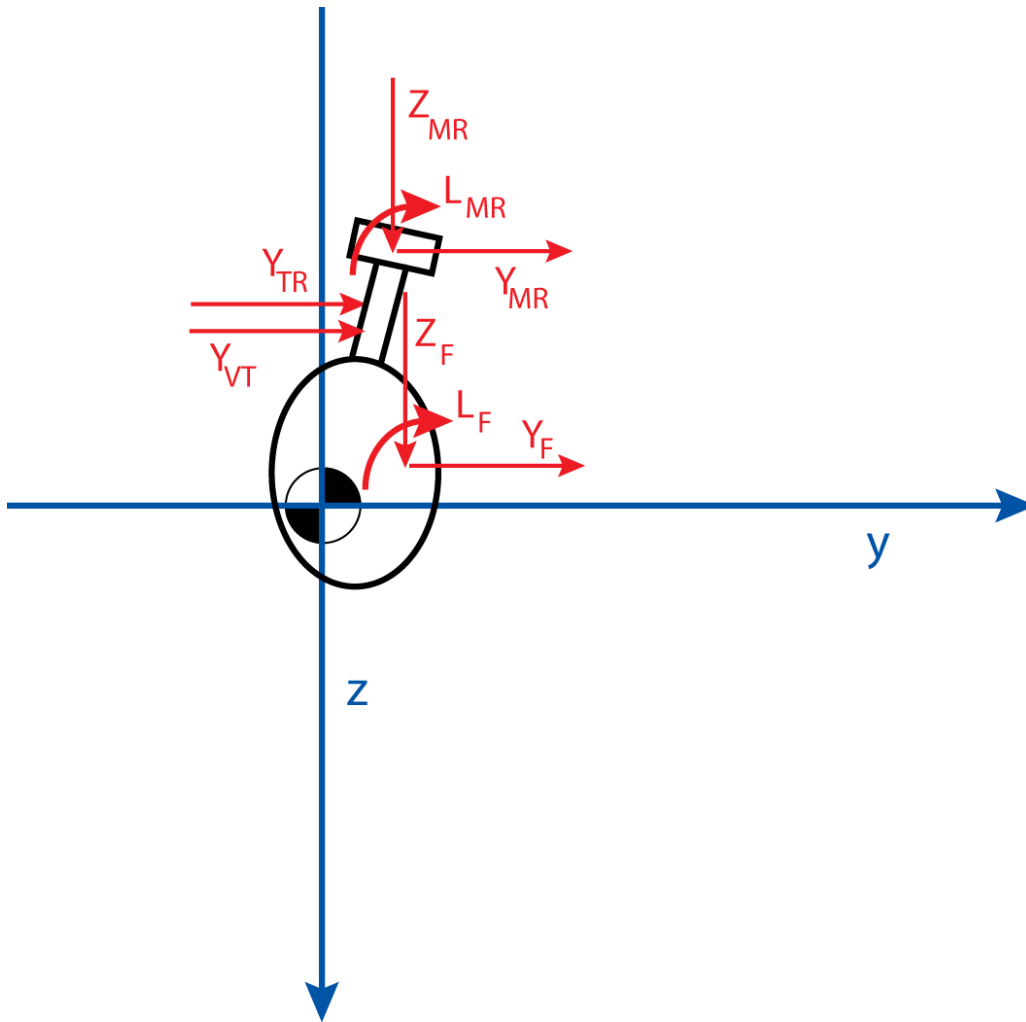
Figure 73: Lateral and Verticle Forces

The lateral force and rolling moment are then:

$$Y = Y_{MR} + Y_{TR} + Y_{VT} + Y_F \qquad (63)$$

$$L = L_{MR} + Y_{MR}h_{MR} + Z_{MR}y_{MR} + Y_{TR}h_{TR} + Y_{VT}h_{VT} + Y_F h_F + L_F \qquad (64)$$

126

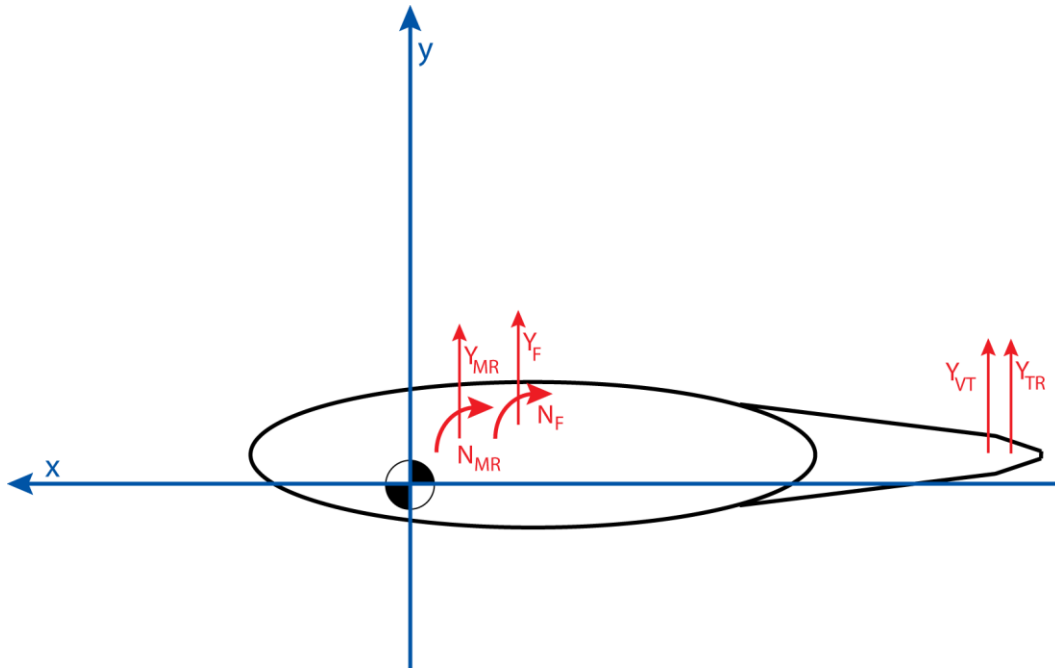Lastly, the top-view free-body diagram may be used to calculate the yaw moment (Fig. 74):

Figure 74: Lateral Forces

$$N = N_{MR} - Y_{MR} l_{MR} - Y_{TR} l_{TR} - Y_{VT} l_{VT} - Y_F l_F + N_F \quad (65)$$

A.2.1 Main Rotor Forces:

Forces on the main rotor are typically calculated along the rotor tip-path-plane, which is generally not aligned with the body axes. The longitudinal and lateral blade flapping, β_{1c} and β_{1s} , determine the tip-path-plane orientation, and may be applied to resolve the rotor forces along the body axes. (Fig. 75)
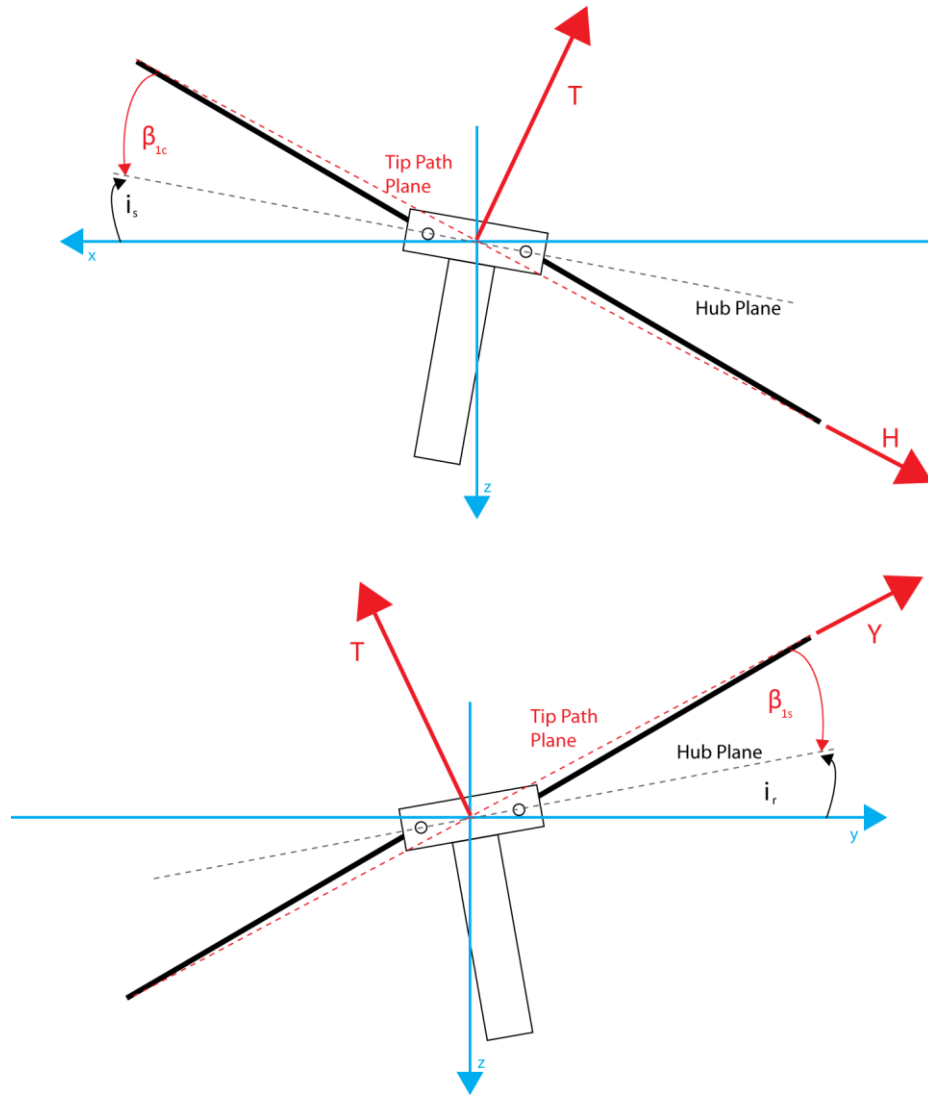
Figure 75: Rotor Planes

The rotor forces along the body axis are therefore:

$$X_{MR} = -H\cos(i_s - \beta_{1c}) - T\sin(i_s - \beta_{1c}) \qquad (66)$$

$$Y_{MR} = -Y\cos(i_r - \beta_{1s}) - T\sin(i_r - \beta_{1s}) \qquad (67)$$

$$Z_{MR} = -T\cos(i_r - \beta_{1s})\cos(i_s - \beta_{1c}) \qquad (68)$$

128

The rotor moments are likewise transformed from the TPP axis to the body axes as follows:

$$L_{MR} = M_x \cos(i_s - \beta_{1c}) - Q \sin(i_s - \beta_{1c}) \qquad (69)$$

$$M_{MR} = M_y \cos(i_r - \beta_{1s}) - Q \sin(i_r - \beta_{1s}) \qquad (70)$$

$$N_{MR} = Q \cos(i_r - \beta_{1s}) \cos(i_s - \beta_{1c}) \qquad (71)$$

Often, the shaft tilt angles, i_s and i_r, may be set to zero if the z axis of the body is aligned with the shaft.

The rotor forces themselves may be calculated through various methods, such as the blade element method, CFD, or simple momentum theory.

When calculating the rotor forces by any method, it is important to note that the aerodynamic applied forces at the rotor are dependent on the airspeed seen at the rotor hub. This is calculated from the speed of the center of mass by adding the wind and rotation velocities, yielding:

$$\vec{v}_{hub} = \vec{v}_{CM} + \vec{\omega}_b \times \vec{h}_s + \vec{w} \qquad (72)$$
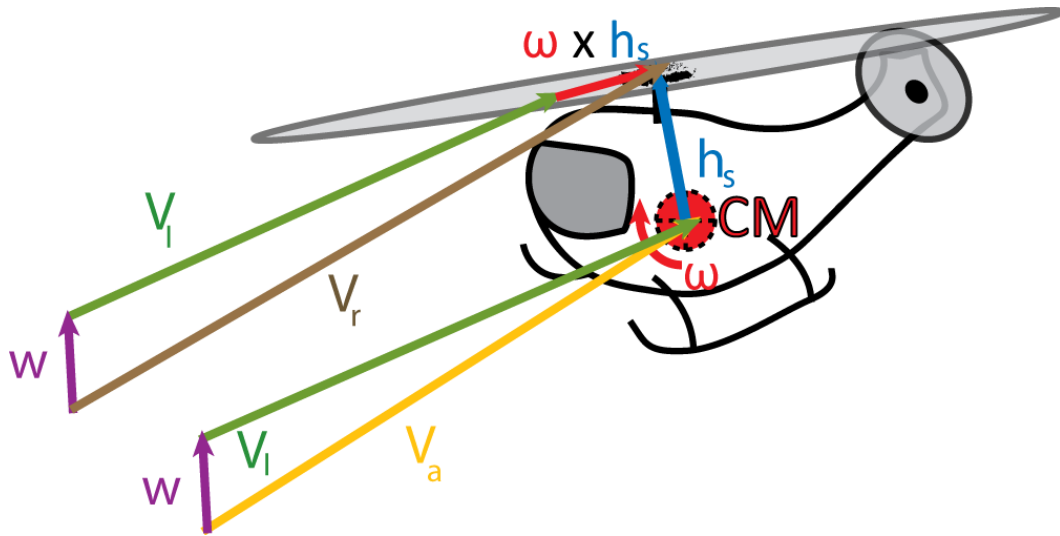
Figure 76: Rotor Velocities

This can also be expressed as the component velocities along the body axes:

$$u_{hub} = u + w_x - r\,y_s + q\,z_s, v_{hub} = v + w_y + r\,x_s - p\,z_s, \quad w_{hub}$$

$$= w + w_z - q\,x_s + p\,y_s$$

$$(73,74,75)$$

Where the location of the hub with respect to the center of mass is expressed as:

$$\vec{h}_s = x_s\hat{\imath} + y_s\hat{\jmath} + z_s\hat{k} \quad (76)$$

In order to develop a simple analytic solution, some approximations may be made. The rotor side force, Y, is typically small for steady flight conditions and may be neglected. The rotor H-force may be approximated by the blade profile drag contribution to the H force which can be derived from the blade element theory:

$$C_H = \frac{1}{4}\sigma\mu C_{d_0} \qquad (77)$$

Where the H-force coefficient is defined as:

$$C_H = \frac{H}{\rho\, A\, (\Omega R)^2} \qquad (78)$$

If the blade flapping angles are assumed small and the body z axis is aligned with the shaft, the rotor forces can then be evaluated as:

$$X_{MR} = -H + T\beta_{1c} \qquad (79)$$

$$Y_{MR} = T\beta_{1s} \qquad (80)$$

$$Z_{MR} = -T \qquad (81)$$

A.2.2 Tail Rotor Forces

The tail rotor forces may be calculated in a similar fashion as the main rotor. However, the tail rotor force in the y direction must be set to counteract the main rotor torque. Additionally, the tail rotor Y-force and longitudinal flapping are typically neglected, yielding the following simplified expressions:

$$X_{TR} = -H_{TR} \qquad (82)$$

$$Y_{TR} = T_{TR} = \frac{Q}{l_{TR}} - Y_{VT}\frac{l_{VT}}{l_{TR}} \qquad (83)$$

Since the tail rotor lateral flapping and torque definitions are dependent on the direction of rotation of the tail rotor, there are different expressions for tail rotor pitching moment and vertical force for tail rotor rotational direction. For a tail rotor with the advancing side on the top:

$$Z_{TR} = -\sin(\beta_{1s})_{TR}\, T_{TR} \qquad (84)$$

$$M_{TR} = Q_{TR} \qquad (85)$$

For a tail rotor with the retreating side on the top, the sign of the above two expressions will be reversed.

The tail rotor H-force may be calculated using the same profile drag expression that was applied to the main rotor. If tail rotor lateral flapping is neglected, the tail rotor vertical force is zero.

A.2.3 Fuselage Forces

Fuselage aerodynamic forces are typically expressed along the aerodynamic velocity of the fuselage. This can be related to the inertial velocity as:

$$\vec{v}_{aero} = \vec{v}_{CM} + \vec{w} \qquad (86)$$

In the absence of wind, the angle of attack and sideslip angles of the fuselage are typically defined as:

$$\alpha_I = \tan^{-1}\frac{u}{w}, \quad \beta_I = \tan^{-1}\frac{v}{V} \qquad (87,88)$$

In the presence of wind, the aerodynamic angles of incidence are no longer directly related to the kinematic velocities of the vehicle. Instead, the velocities of the vehicle relative to the medium must be used:

$$u_{aero} = u + w_x, \quad v_{aero} = v + w_y, \quad w_{aero} = w + w_z \qquad (89,90,91)$$

Then the aerodynamic angles of incidence are:

$$\alpha = \tan^{-1} \frac{u_{aero}}{w_{aero}}, \quad \beta = \tan^{-1} \frac{v_{aero}}{V_{aero}} \qquad (92,93)$$

The fuselage lift and drag forces may then be resolved to the body axes:

$$X_F = -D_F \cos\alpha \cos\beta - L_F \sin\alpha \cos\beta \qquad (94)$$

$$Y_F = -D_F \cos\alpha \sin\beta - L_F \sin\alpha \sin\beta \qquad (95)$$

$$Z_F = -D_F \sin\alpha \cos\beta - L_F \cos\alpha \cos\beta \qquad (96)$$

The lift and drag forces can be expressed functions of the aerodynamic incidence angles, however for helicopters with relatively bluff bodies, the aerodynamic forces may be assumed constant with incidence. Additionally, fuselage lift forces are small and may be neglected. The drag force can be expressed in terms of the effective flat plate area drag of the fuselage, f:

$$D_F = \frac{1}{2}\rho V_\infty^2 f_{eff} \qquad (97)$$

The fuselage yaw, pitch, and roll moments are difficult to calculate but may also be transformed to the body axes in a similar fashion. However, fuselage aerodynamic moments are generally small, and may also be neglected.

Assuming the incidence angles are small and neglecting fuselage lift forces, the following expressions may be used to estimate the fuselage forces:

$$X_F = -D_F \qquad (98)$$

$$Y_F = -D_F \beta \qquad (99)$$

$$Z_F = -D_F \alpha \qquad (100)$$

A.2.4 Empennage Forces

The horizontal and vertical forces of the horizontal stabilizer are related to the lift and drag forces, aligned with the relative wind seen by the horizontal stabilizer (Fig. 77):

$$X_{HT} = L_{HT} \sin(\alpha_{HT} - i_{HT}) - D_{HT} \cos(\alpha_{HT} - i_{HT}) \qquad (101)$$

$$Z_{HT} = -L_{HT} \cos(\alpha_{HT} - i_{HT}) - D_{HT} \sin(\alpha_{HT} - i_{HT}) \qquad (102)$$
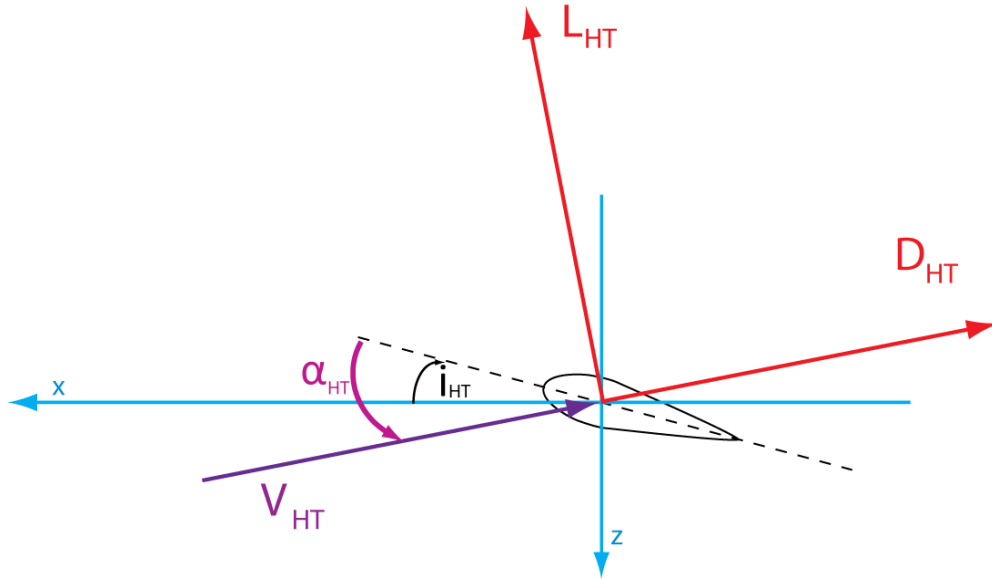
Figure 77: Aerodynamics of a Horizontal Tail

The free-stream velocity and angle of attack for the horizontal tail differ from those seen by the vehicle center of mass, due to downwash from the fuselage and main rotor and the pitch rate of the helicopter about the center of mass.

$$\alpha_{HT} = \alpha - \epsilon_{MR} - \epsilon_F + \frac{q\, l_{HT}}{V} \qquad (103)$$

The downwash angles and change in free-stream velocity for both main rotor and fuselage are difficult to find analytically and so are typically found from either empirical or computational methods.

The vertical stabilizer forces are found in a similar fashion:

$$X_{VT} = -D_{VT} \cos(\beta_{VT} + i_{VT}) - L_{VT} \sin(\beta_{VT} + i_{VT}) \qquad (104)$$

$$Y_{VT} = -D_{VT} \sin(\beta_{VT} + i_{VT}) + L_{VT} \cos(\beta_{VT} + i_{VT}) \qquad (105)$$

$$Z_{VT} = X_{VT} \sin\left(\alpha + \frac{q\, l_{VT}}{V}\right) \qquad (106)$$

A vertical force is produced by the vertical tail due to the component of the

longitudinal force in the vertical direction. As in the horizontal stabilizer case, the

sideslip angle is dependant not only on the sideslip seen at the center of mass, but also

components due to the yawing motion of the helicopter, and sidewash from the main

rotor, tail rotor, and fuselage.

$$\beta_{VT} = \beta + \eta_{MR} + \eta_{TR} + \eta_F - \frac{r\, l_{VT}}{V} \qquad (107)$$

Sidewash contributions from the fuselage are generally very small and may be

ignored. The main rotor contributes to sidewash at the vertical tail through swirl in the

main rotor wake, and is likewise a small effect for most flight conditions. Sidewash due

to the tail rotor can be significant when there is little separation between the tail rotor and

vertical stabilizer – this angle can be estimated through the rotor download relation:

$$\eta_{TR} = \frac{T_{TR}}{2\, \rho\, V^2 A_{VT}} \qquad (108)$$

The empennage components provide significant contributions to the moment

equations, however the forces applied to the helicopter by the tail components are small

relative to the main rotor and body forces, and may be neglected or lumped into the

fuselage lift and drag parameters when evaluating the vehicle force equations.

A.2.4 Simplified Force and Moment Balance:

By substituting the simplified expressions for each component listed above into the

X, Y, and Z force balance equations, and neglecting the empennage, the following

equations are produced:

$$-H + T\beta_{1c} - H_{TR} - D_F - mg\sin\theta = m(\dot{u} + qw - rv) \qquad (109)$$

$$T\beta_{1s} + \frac{Q}{l_{TR}} - D_F\beta + mg\cos\theta\sin\varphi = m(\dot{v} + ru - pw) \qquad (110)$$

$$-T - D_F\alpha + mg\cos\theta\cos\varphi = m(\dot{w} + pv - qu) \qquad (111)$$

If the Euler pitch angle is small, the force expressions may be simplified further:

$$-H + T\beta_{1c} - H_{TR} - D_F - W\theta = m(\dot{u} + qw - rv) \qquad (112)$$

$$T\beta_{1s} + \frac{Q}{l_{TR}} - D_F\beta + W\sin\varphi = m(\dot{v} + ru - pw) \qquad (113)$$

$$-T - D_F\alpha + W\cos\varphi = m(\dot{w} + pv - qu) \qquad (114)$$

Recall that in the case of no wind, the aerodynamic angles of incidence may be

expressed in terms of the kinematic velocities of the aircraft:

$$-H + T\beta_{1c} - H_{TR} - D_F - W\theta = m(\dot{u} + qw - rv) \qquad (115)$$

$$T\beta_{1s} + \frac{Q}{l_{TR}} - D_F\frac{v}{V} + W\sin\varphi = m(\dot{v} + ru - pw) \qquad (116)$$

$$-T - D_F\frac{u}{w} + W\cos\varphi = m(\dot{w} + pv - qu) \qquad (117)$$

The moment equations may also be simplified by making the same assumptions. Additionally, the pitching and rolling moments produced by articulated or teetering main or tail rotors are very small, and can be neglected for steady flight conditions.

$$Q\beta_{1s} + (H - T\beta_{1c})h_{MR} + Tl_{MR} + H_{TR}h_{TR} + D_Fh_F - D_F\alpha l_F = \dot{h}_x + qh_z - rh_y$$

(118)

$$Q\beta_{1c} + T\beta_{1s}h_{MR} + Ty_{MR} + \frac{Q}{l_{TR}}h_{TR} - D_F\beta h_F = \dot{h}_y + rh_x - ph_z$$

(119)

$$Q - T\beta_{1s}l_{MR} - T_{TR}l_{TR} + D_F\beta l_F = \dot{h}_z + ph_y - qh_x$$

(120)

Further, if the center of mass of the helicopter is assumed aligned along x and y with the hub and coincident with the aerodynamic center of the fuselage:

$$Q\beta_{1s} + (H - T\beta_{1c})h_{MR} + H_{TR}h_{TR} = \dot{h}_x + qh_z - rh_y \qquad (121)$$

$$Q\beta_{1c} + T\beta_{1s}h_{MR} + \frac{Q}{l_{TR}}h_{TR} = \dot{h}_y + rh_x - ph_z \qquad (122)$$

$$Q - T_{TR}l_{TR} = \dot{h}_z + ph_y - qh_x \qquad (123)$$

If the angular momentum of the helicopter is considered constant, the left hand side of the equation may be simplified:

$$Q\beta_{1s} + (H - T\beta_{1c})h_{MR} + H_{TR}h_{TR} = qh_z - rh_y \qquad (124)$$

$$Q\beta_{1c} + T\beta_{1s}h_{MR} + T_{TR}h_{TR} = rh_x - ph_z \qquad (125)$$

138

$$Q - T_{TR}l_{TR} = ph_y - qh_x \qquad\qquad (126)$$

For a steady flight condition, the Euler pitch and roll angles may be assumed constant – substituting the relations between pitch, roll, and yaw rate due to the Euler yaw rate for all six equations:

$$-H + T\beta_{1c} - H_{TR} - D_F - W\theta = m\left(\dot{u} + \dot{\psi}\sin\varphi\,w - \dot{\psi}\cos\varphi\,v\right) \qquad (127)$$

$$T\beta_{1s} + \frac{Q}{l_{TR}} - D_F\beta + W\sin\varphi = m\left(\dot{v} + \dot{\psi}\cos\varphi\,u - \dot{\psi}\,\theta\cos\varphi\,w\right) \qquad (128)$$

$$-T - D_F\alpha + W\cos\varphi = m\left(\dot{w} + \dot{\psi}\,\theta\cos\varphi\,v - \dot{\psi}\sin\varphi\,u\right) \qquad (129)$$

$$Q\beta_{1s} + (H - T\beta_{1c})h_{MR} + H_{TR}h_{TR} = \dot{\psi}\sin\varphi\,h_z - \dot{\psi}\cos\varphi\,h_y \qquad (130)$$

$$Q\beta_{1c} + T\beta_{1s}h_{MR} + T_{TR}h_{TR} = \dot{\psi}\cos\varphi\,h_x - \dot{\psi}\,\theta\cos\varphi\,h_z \qquad (131)$$

$$Q - T_{TR}l_{TR} = \dot{\psi}\,\theta\cos\varphi\,h_y - \dot{\psi}\sin\varphi\,h_x \qquad (132)$$

For a given steady flight trajectory, the left hand side of the equations can be calculated. Then, it is possible to solve all six equations of motion for the required main and tail rotor thrust, the steady longitudinal and lateral flapping angles, β_{1c} and β_{1s}, and the Euler pitch and roll angles, θ and φ. The angle of attack of the tip path plane, α_{TPP}, may then be found. (Fig. 78)
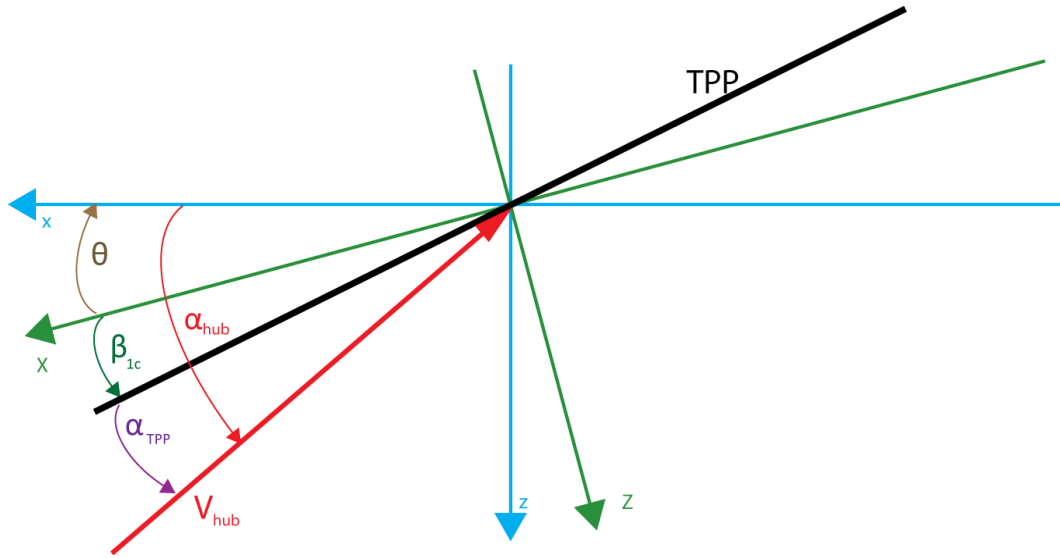
Figure 78: Rotor Tip-Path Plane Angle

$$\alpha_{TPP} = \alpha_{hub} + \theta - \beta_{1c} \qquad (133)$$

Where the angle of attack seen at the hub may be calculated from the hub airspeed velocity components previously derived from the fuselage rotation:

$$\alpha_{hub} = \tan^{-1} \frac{u_{hub}}{w_{hub}} \qquad (134)$$

Assuming a small angle and substituting the hub velocity components derived previously yields:

$$\alpha_{hub} = \frac{u + w_x - r\, y_s + q\, z_s}{w + w_z - q\, x_s + p\, y_s} \qquad (135)$$

If the rotational rates are small enough to be neglected, this expression reduces to the fuselage angle of attack.

A.3 Rotor Inflow:

Now having the velocity and angle of attack of the main rotor tip path plane with respect to the medium, it is possible to apply momentum theory to estimate the main rotor inflow.

Simple momentum theory requires that a known control volume be established in which the conservation laws may be applied. For a conventional helicopter, the standard procedure is to idealize the main rotor as an actuator disk through which an evenly distributed airflow passes. The following assumptions are made: The flow is assumed to be one dimensional, quasi-steady, incompressible, and inviscid.

The induced velocity produced normal to disk of each rotor can be expressed through simple momentum theory as:

$$v_i = \sqrt{\frac{T}{2\rho A}}$$

(136)

where A is the circular area swept by the rotor blades.

The hover inflow becomes the average induced velocity normal to the effective rotor disk:

$$\lambda_h = v_h = \sqrt{\frac{T}{2\rho A_{eff}}}$$

(137)

The non-dimensional thrust coefficient may be defined as:

$$C_T = \frac{T}{\rho A \Omega^2 R^2}$$
(138)

A.3.1 Extension to the Forward Flight Case

In order to solve for the induced velocity during forward flight, the momentum theory quartic can be used to relate the induced velocity to the tip-path-plane angle and to the forward airspeed:

$$v_i^4 - 2V_\infty v_i^3 \sin\alpha + V_\infty^2 v_i^2 + v_h^4 = 0$$
(139)

Assuming the tip-path-plane angle to be small, and non-dimensionalizing the equation by the hover induced velocity from equation the expression becomes:

$$\bar{v}_i^4 - 2\bar{V}_\infty \bar{v}_i^3 \alpha + \bar{V}_\infty^2 \bar{v}_i^2 + 1 = 0$$
(140)

where

$$\bar{V}_\infty = \frac{V_\infty}{v_h}$$

$$\bar{v}_i = \frac{v_i}{v_h}$$

The solution to the quartic can be found by taking the first order terms of the Taylor series expansion about perturbations in the tip-path-plane angle, yielding:

$$\bar{v}_i = \bar{v}_0 + \frac{\partial \bar{v}_i}{\partial \alpha} \Delta\alpha + ...$$
(141)

The solution to the quartic inflow equation when the tip-path-plane angle is zero is a bi-quadratic expression and can be solved explicitly:

$$\overline{v}_0 = \left[\sqrt{\frac{1}{4}\overline{V}_\infty^4 + 1} - \frac{1}{2}\overline{V}_\infty^2 \right]^{\frac{1}{2}}$$

(142)

The total inflow velocity is the combination of the induced velocity and the component of forward velocity which passes through the rotor disk aligned to the tip-path-plane. The small angle assumption is used to find the following non-dimensionalized expression:

$$\overline{\lambda} = \overline{V}_\infty \alpha - \overline{v}_i$$

(143)

The expansion of the induced velocity is then substituted into the inflow equation:

$$\overline{\lambda} = -\overline{v}_0 + \left(1 - \frac{1}{\overline{V}_\infty}\frac{\partial \overline{v}_i}{\partial \alpha} \right)\overline{V}_\infty \alpha$$

(144)

For low speed forward flight, the term $1 - \frac{1}{\overline{V}_\infty}\frac{\partial \overline{v}_i}{\partial \alpha}$ can be readily computed numerically. At hover, the term takes a value of 0.5. For forward velocities greater than three times the hover induced velocity, the term asymptotically approaches unity.

A.4 Kinematics of Turning Flight

The position vector in stationary inertial space for a helicopter general steady turn with a constant radius about a point which is drifting horizontally and descending can be described as:

$$\vec{A} = \begin{bmatrix} A_X \\ A_Y \\ A_Z \end{bmatrix} = \begin{bmatrix} x_0 + V_X t + s \sin\psi \\ y_0 + V_Y t - s \cos\psi \\ z_0 + V_Z t \end{bmatrix} \qquad (145)$$

Taking to derivative of A with respect to time yields the velocity of the helicopter body in the stationary frame:

$$\frac{d\vec{A}}{dt} = \begin{bmatrix} \frac{dA_X}{dt} \\ \frac{dA_Y}{dt} \\ \frac{dA_Z}{dt} \end{bmatrix} = \begin{bmatrix} V_X + s\dot\psi \cos\psi \\ V_Y + s\dot\psi \sin\psi \\ V_Z \end{bmatrix} \qquad (146)$$

These velocities may then be transformed along the helicopter body axis system through the standard Euler vector transformation matrix:

$$\begin{bmatrix} u \\ v \\ w \end{bmatrix} = \begin{bmatrix} \cos\theta\cos\psi & \cos\theta\sin\psi & -\sin\theta \\ \sin\varphi\sin\theta\cos\psi - \cos\varphi\sin\psi & \sin\varphi\sin\theta\sin\psi + \cos\varphi\cos\psi & \sin\varphi\cos\theta \\ \cos\varphi\sin\theta\cos\psi + \sin\varphi\sin\psi & \cos\varphi\sin\theta\sin\psi - \sin\varphi\cos\psi & \cos\varphi\cos\theta \end{bmatrix} \begin{bmatrix} \frac{dA_X}{dt} \\ \frac{dA_Y}{dt} \\ \frac{dA_Z}{dt} \end{bmatrix}$$

$$(147)$$

Expanding these expressions then provides the scalar body axis inertial velocities of the helicopter throughout the maneuver:

$$u = s\dot\psi \cos\theta + \cos\theta\cos\psi\, V_X + \cos\theta\sin\psi\, V_Y - \sin\theta\, V_Z \qquad (148)$$

$$v = s\dot{\psi} \sin \theta \sin \varphi + (\sin \varphi \sin \theta \cos \psi - \cos \varphi \sin \psi)V_X + (\sin \varphi \sin \theta \sin \psi -$$

$$\cos \varphi \cos \psi)V_Y - \sin \varphi \cos \theta \, V_Z$$

$$(149)$$

$$w = s\dot{\psi} \cos \varphi \sin \theta + (\cos \varphi \sin \theta \cos \psi + \sin \varphi \sin \psi)V_X + (\cos \varphi \sin \theta \sin \psi -$$

$$\sin \varphi \cos \psi)V_Y + \cos \varphi \cos \theta \, V_Z$$

$$(150)$$

Next, the derivatives of these quantities may be taken with respect to time to yield:

$$\dot{u} = s\ddot{\psi} \cos \theta - (s \sin \theta)\dot{\theta} + V_X(\dot{\psi} \cos \theta \sin \psi - \dot{\theta} \sin \theta \cos \psi)$$
$$+ V_Y(\dot{\psi} \cos \theta \cos \psi - \dot{\theta} \sin \theta \sin \psi) - V_Z \dot{\theta} \cos \theta$$

$$(151)$$

$$\dot{v} = s(\dot{\theta}\dot{\psi} \cos \theta \sin \varphi + \dot{\varphi}\dot{\psi} \cos \varphi \sin \theta + \ddot{\psi} \sin \theta \sin \varphi)$$
$$+ V_X(\dot{\theta} \cos \theta \cos \psi \sin \varphi + \dot{\varphi}[\cos \varphi \sin \psi \sin \theta + \sin \varphi \sin \psi]$$
$$- \dot{\psi}[\cos \varphi \cos \psi + \sin \theta \sin \varphi \sin \psi])$$
$$+ V_Y(\dot{\theta} \cos \theta \sin \psi \sin \varphi + \dot{\varphi}[\cos \varphi \sin \psi \sin \theta - \sin \varphi \cos \psi]$$
$$+ \dot{\psi}[\cos \varphi \sin \psi - \sin \theta \sin \varphi \cos \psi])$$
$$+ V_Z(-\dot{\theta} \sin \theta \sin \varphi + \dot{\varphi} \cos \varphi \cos \theta)$$

$$(152)$$

$$\dot{w} = s(\dot{\theta}\dot{\psi}\cos\theta\cos\varphi - \dot{\varphi}\dot{\psi}\sin\varphi\sin\theta + \ddot{\psi}\sin\theta\cos\varphi)$$

$$+ V_X(\dot{\theta}\cos\theta\cos\psi\cos\varphi + \dot{\varphi}[-\sin\varphi\cos\psi\sin\theta + \cos\varphi\sin\psi]$$

$$+ \dot{\psi}[\sin\varphi\cos\psi - \sin\theta\cos\varphi\sin\psi])$$

$$+ V_Y(\dot{\theta}\cos\theta\sin\psi\cos\varphi + \dot{\varphi}[-\sin\varphi\sin\psi\sin\theta - \cos\varphi\cos\psi]$$

$$+ \dot{\psi}[\sin\varphi\sin\psi + \sin\theta\cos\varphi\cos\psi])$$

$$+ V_Z(-\dot{\theta}\sin\theta\cos\varphi - \dot{\varphi}\sin\varphi\cos\theta)$$

$$(153)$$

V_Y can be assumed as zero, since the direction of drift in the stationary XY plane is arbitrary. The expressions can be further simplified by assuming the Euler pitch and roll rates, $\dot{\theta}$ and $\dot{\varphi}$ are negligible. This yields the following scalar expressions:

$$\dot{u} = s\ddot{\psi}\cos\theta + V_X(\dot{\psi}\cos\theta\sin\psi) \tag{154}$$

$$\dot{v} = s\ddot{\psi}\sin\theta\sin\varphi - \dot{\psi}V_X(\cos\varphi\cos\psi + \sin\theta\sin\varphi\sin\psi) \tag{155}$$

$$\dot{w} = s\ddot{\psi}\sin\theta\cos\varphi + \dot{\psi}V_X(\sin\varphi\cos\psi - \sin\theta\cos\varphi\sin\psi) \tag{156}$$

$$u = s\dot{\psi}\cos\theta + \cos\theta\cos\psi\, V_X - \sin\theta\, V_Z \tag{157}$$

$$v = s\dot{\psi}\sin\theta\sin\varphi + (\sin\varphi\sin\theta\cos\psi - \cos\varphi\sin\psi)V_X - \sin\varphi\cos\theta\, V_Z \tag{158}$$

$$w = s\dot{\psi}\cos\varphi\sin\theta + (\cos\varphi\sin\theta\cos\psi + \sin\varphi\sin\psi)V_X + \cos\varphi\cos\theta\, V_Z \tag{159}$$

These equations may then be substituted, along with the transformation equations for the Euler rates to helicopter rotational rates, into the right hand side of the force balance equations developed previously to solve for the orientation of the helicopter in space. If the Euler pitch angle is assumed small. The scalar expressions may be simplified:

$$\dot{u} = s\ddot{\psi} + V_X\left(\dot{\psi}\sin\psi\right) \tag{160}$$

$$\dot{v} = s\ddot{\psi}\theta\sin\varphi - \dot{\psi}V_X(\cos\varphi\cos\psi + \theta\sin\varphi\sin\psi) \tag{161}$$

$$\dot{w} = s\ddot{\psi}\theta\cos\varphi + \dot{\psi}V_X(\sin\varphi\cos\psi - \theta\cos\varphi\sin\psi) \tag{162}$$

$$u = s\dot{\psi} + \cos\psi\,V_X - \theta V_Z \tag{163}$$

$$v = s\dot{\psi}\theta\sin\varphi + (\theta\sin\varphi\cos\psi - \cos\varphi\sin\psi)V_X - \sin\varphi\,V_Z \tag{164}$$

$$w = s\dot{\psi}\theta\cos\varphi + (\theta\cos\varphi\cos\psi + \sin\varphi\sin\psi)V_X + \cos\varphi\,V_Z \tag{165}$$

A.5 Simplified Case: Steady Turning Flight in No Wind Conditions

Next, the simplified case of a helicopter flying a general steady helical maneuver in the absence of wind is investigated. Assume the Euler pitch angle, θ, is zero. Additionally, assume wind velocities V_x and V_z are zero. Finally, due to the steadiness condition, the rate at which the helicopter rotates about the axis of the turn can be considered constant, therefore $\ddot{\psi}$ is also set to zero. Applying these assumptions to the kinematic relations for body-axis velocity and accelerations yields:

$$\dot{u} = 0, \dot{v} = 0, \dot{w} = 0 \qquad (166,167,168)$$

$$u = s\dot{\psi}, v = 0, w = 0 \qquad (169,170,171)$$

These quantities can now be substituted into the right hand side of the force balance relations, to yield the following relations:

$$-H + T\beta_{1c} - H_{TR} - D_f = 0 \qquad (172)$$

$$T\beta_{1s} + \frac{Q}{l_{TR}} - D_f\beta + W\sin\varphi = ms\dot{\psi}^2\cos\varphi \qquad (173)$$

$$-T - D_f\alpha + W\cos\varphi = -ms\dot{\psi}^2\sin\varphi \qquad (174)$$

It is immediately apparent that the only inertial force applied is a centripetal acceleration due to the steady turn.

As shown previously, for the no wind condition the angle of attack seen by the helicopter rotor hub is equal to that seen by the fuselage. Since the helicopter is banked by angle φ, this is equivalent to a component of the flight path angle, γ. This provides the following relation for calculating the tip-path-plane angle of attack:

$$\alpha_{TPP} = \alpha - \beta_{1c} = \gamma\cos\varphi - \beta_{1c} \qquad (175)$$

The longitudinal flapping angle, β_{1c}, may be solved for from the longitudinal force balance equation.

$$\beta_{1c} = \frac{H + H_{TR} + D_f}{T} \qquad (176)$$

However, thrust remains an unknown quantity – assuming no download on the fuselage, the vertical force balance equation may be employed to find the thrust.

$$T = W\cos\varphi + ms\dot{\psi}^2\sin\varphi \qquad (177)$$

148

Evaluating the lateral force balance equation, neglecting fuselage and tail rotor side force, yields the kinematic expression:

$$\tan \varphi = \frac{s\dot{\psi}^2}{g} \quad (178)$$

Further substitution into the simplified vertical force balance expression produces:

$$T = W \cos \varphi + W \tan \varphi \sin \varphi = \frac{W}{\cos \varphi} \quad (179)$$

Substitution of these simplified expressions into the tip-path-plane angle of attack

expression:

$$\alpha_{TPP} = -\gamma \cos \varphi - \frac{D_f + H + H_{TR}}{W} \cos \varphi = -\left(\gamma + \frac{D_f + H + H_{TR}}{W}\right) \cos \varphi \quad (180)$$

H-forces may be included in the fuselage drag term, D_f:

$$\alpha_{TPP} = -\left(\gamma + \frac{D_f}{W}\right) \cos \varphi \quad (181)$$

Longitudinal accelerations may be considered by redefining $\dot{u} = a_x$ – this definition results

in a new longitudinal force balance equation:

$$-H + T\beta_{1c} - H_{TR} - D_f = ma_x \quad (182)$$

Carrying this through the above derivation of the simplified equations results in an

expression for the tip-path-plane angle of attack as:

$$\alpha_{TPP} = -\left(\gamma + \frac{D_f + H + H_{TR}}{W}\right) \cos \varphi - \frac{1}{g} a_x \quad (183)$$

This expression forms the basis of the Q-SAM equivalence for steady turning flight. It is evident that an increase in the bank angle of the helicopter (in response to the centripetal acceleration of the turn) produces an increase in overall main rotor thrust. The increase in rotor thrust will cause an increase in net rotor inflow – consequently, Q-SAM predicts that descent rate for maximum BVI noise will be higher for a helicopter in turning flight than for a helicopter in a similar straight-line flight condition. Additionally, the increase in thrust will increase the blade loading, causing the rotor blades to deposit stronger vortices into the air. Therefore, it is predicted that the peak BVI noise level in a turn, at the flight path angle for maximum BVI noise, will be higher than the peak BVI noise level for straight-line descending flight cases.

Appendix B: Sutherland and Bass Atmospheric Absorption

Atmospheric absorption losses are individually calculated and added to the SPL for each 1 Hz narrow band using the ASA/ISO standard classical and rotational relaxation method developed by Sutherland and Bass with the Goff-Gratch equation [49] used to determine absolute humidity from ambient weather data. The method is shown in the equations below. Representative atmospheric data for propagation (static pressure, temperature, and relative humidity) is collected at a point halfway between the mean altitude of the helicopter trajectory and the ground for the 2006 dataset, where a meteorology balloon was available. In 2007, this data was measured from a ground based station. Measured winds were below 5 knots in all test cases presented in this thesis, and the affect on propagation is assumed to be small.

1. Determine Ratio of Partial Pressure of Saturated Water Vapor to Reference Pressure using Goff-Gratch Equation:

$$\log_{10}\left(\frac{P_{sat}}{P_0}\right) = 10.79586\left[1 - \frac{T_{01}}{T}\right] -$$

$$5.02808\log_{10}\left(\frac{T}{T_{01}}\right) + 1.50474 \times 10^{-4}\left(1 - 10^{-8.29692\left[\frac{T}{T_{01}} - 1\right]}\right)$$

$$+ 0.42873 \times 10^{-3}\left(10^{4.76955\left[1 - \frac{T_{01}}{T}\right]} - 1\right) - 2.2195983$$

$$(184)$$

2. Compute Absolute Humidity:

$$h = h_r \frac{P_{sat}}{P_0}\left(\frac{P}{P_0}\right)^{-1}$$

$$(185)$$

3. Compute the Relaxation Frequencies of Oxygen and Nitrogen:

$$f_{r,O} = \frac{P}{P_0}\left\{24 + 4.41\times10^4 h\,\frac{0.05+h}{0.391+h}\right\}$$

$$f_{r,N} = \frac{P}{P_0}\left(\frac{T}{T_0}\right)^{-\frac{1}{2}}\left\{9 + 350e^{-6.142\left[\left(\frac{T}{T_0}\right)^{-\frac{1}{3}}-1\right]}\right\}$$

(186)

4. Compute Absorption in dB/meter

$$a(f) = 8.686\left(\frac{T}{T_0}\right)^{\frac{1}{2}} f^2 \left(\frac{P}{P_0}\right)^{-1}$$

$$\left\{1.84\times10^{-11} + 2.19\times10^{-4}\left(\frac{T}{T_0}\right)^{-1}\left(\frac{P}{P_0}\right)\right.$$

$$\times\left(\frac{2239}{T}\right)^2 \frac{e^{\frac{-2239}{T}}}{f_{r,O}+\dfrac{f^2}{f_{r,O}}} +$$

$$\left. 8.16\times10^{-4}\left(\frac{T}{T_0}\right)^{-1}\left(\frac{P}{P_0}\right)\left(\frac{3352}{T}\right)^2 \frac{e^{\frac{-3352}{T}}}{f_{r,N}+\dfrac{f^2}{f_{r,N}}}\right\}$$

(187)

Appendix C: BVI "Hotspot" Frequency Spectra and Pressure Time-Histories

All frequency spectra and pressure time-histories have been computed from de-Dopplerized data. The de-Dopplerization process used in this thesis is explained in Appendix D. The pressure time-histories and frequency spectra are computed for the ground microphone measurement point on the acoustic radiation sphere closest to the interpolated BVISPL "hotspot".

C.1 60 kts Straight-Line Flight Cases
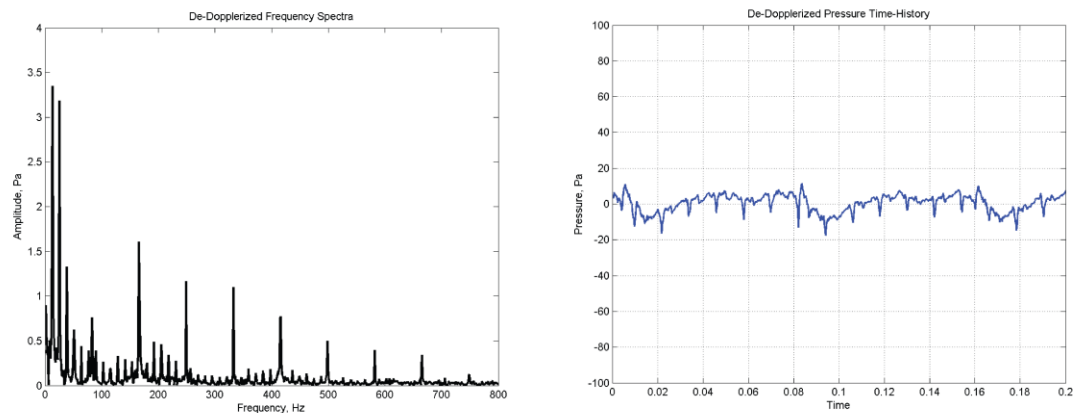
Figure 79: Level Flight
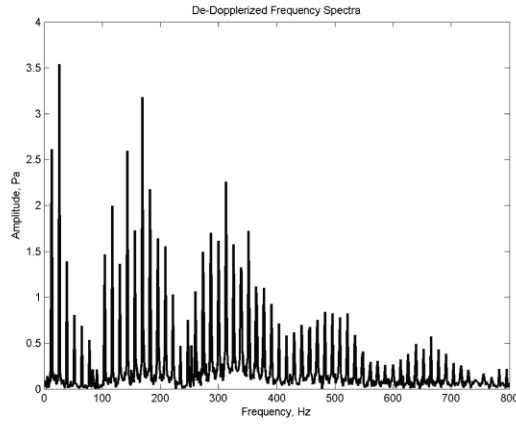
Figure 80: 3 Degree Descent
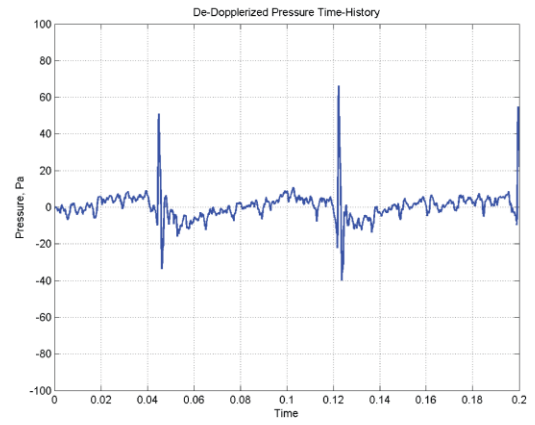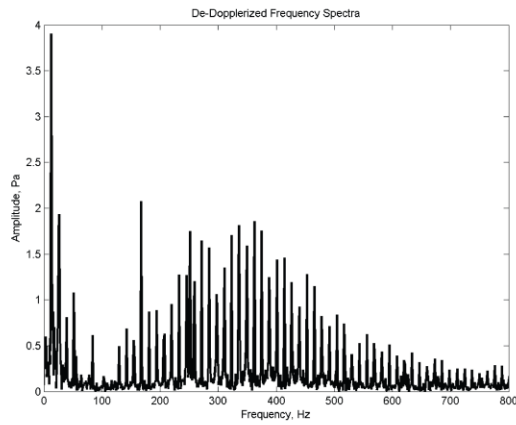
Figure 81: 4.5 Degree Descent
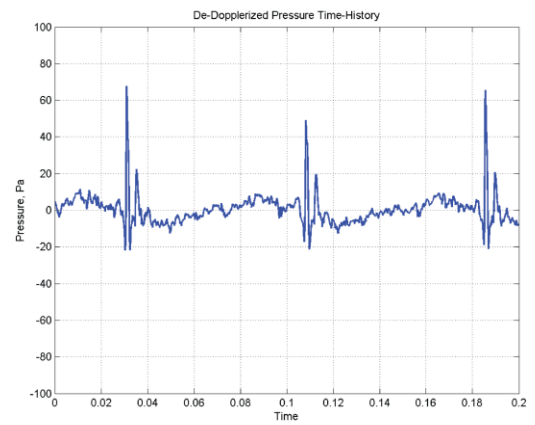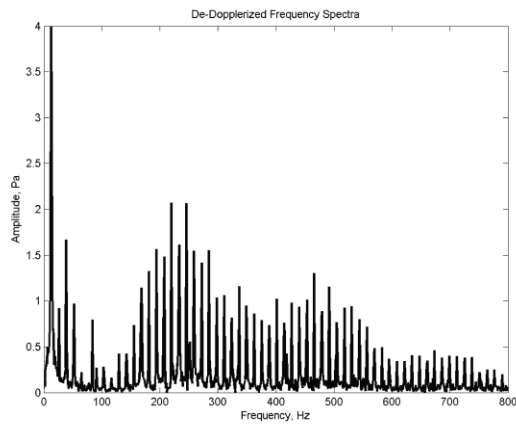
Figure 82: 6 Degree Descent

154
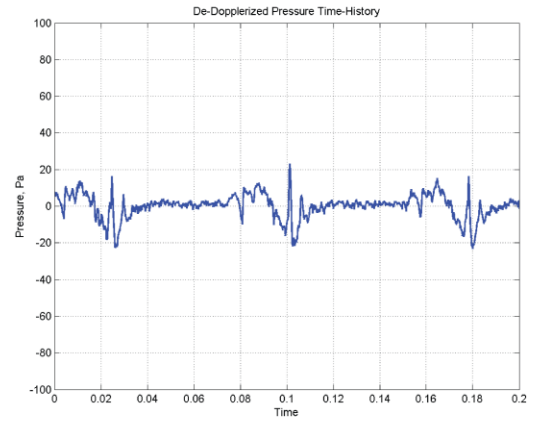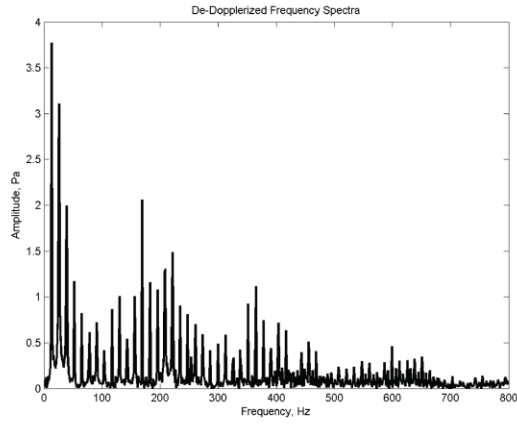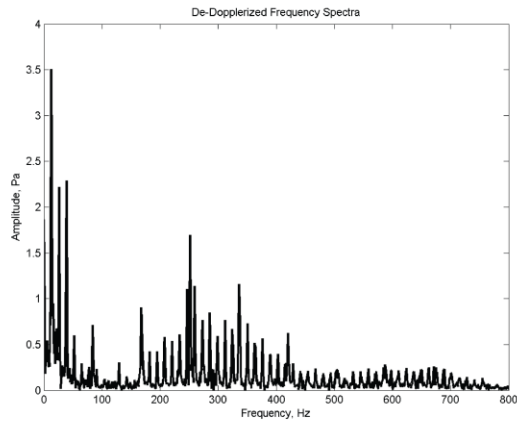
Figure 83: 7.5 Degree Descent
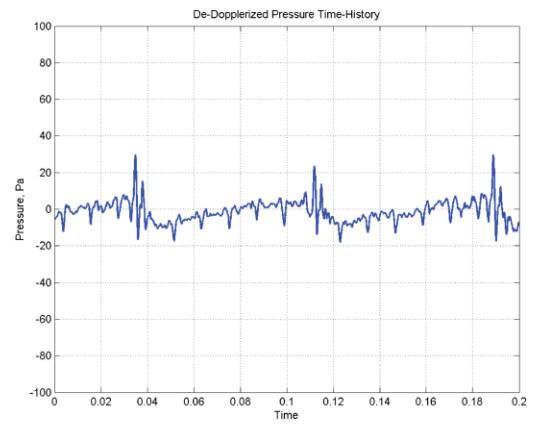
Figure 84: 9 Degree Descent

C.2 Turning Flight Cases

C.2.1 60 kts, 30 Degree Bank, Right Hand Turns

Note: "Hotspot" of Level Right Hand Turn unsteady due to rough weather and pilot control inputs. This has led to moderate BVI at this measurement point.
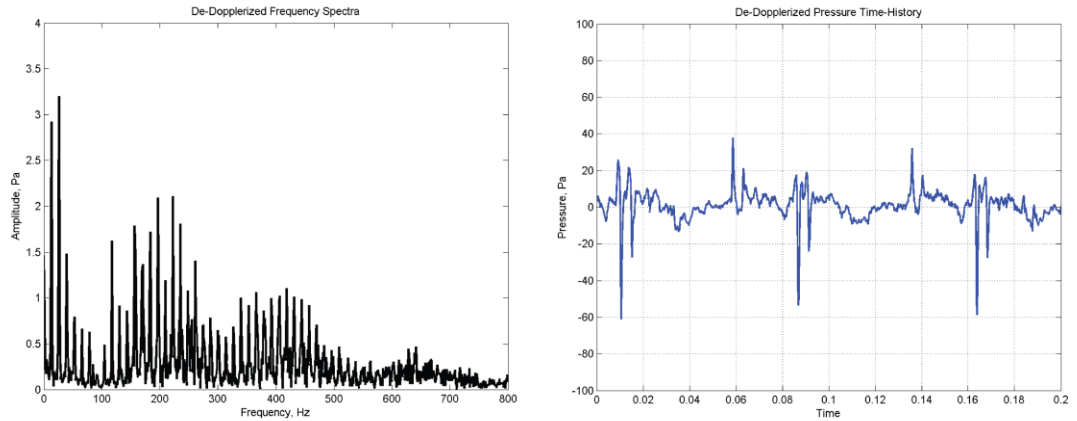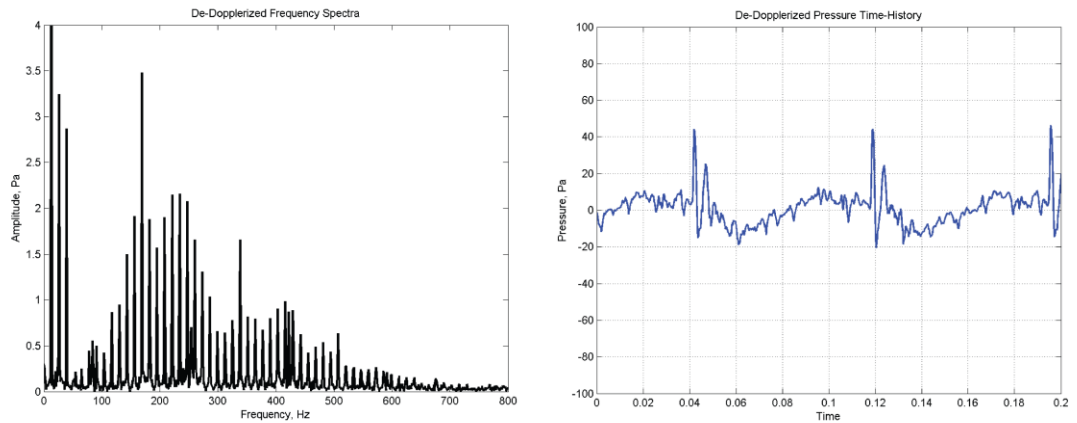

igure 85: Level Flight
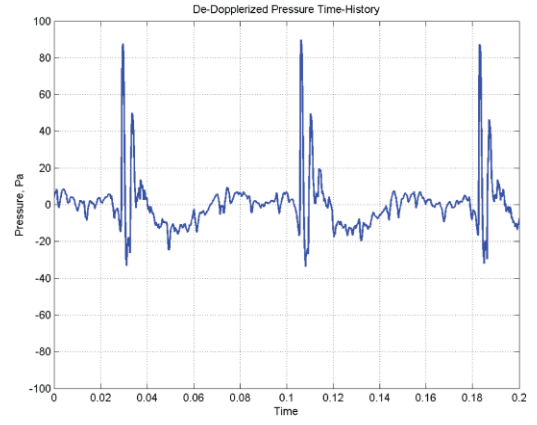

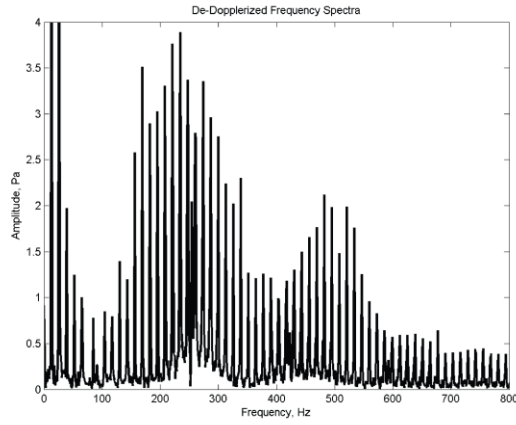**Figure 86: 3 Degree Descent**

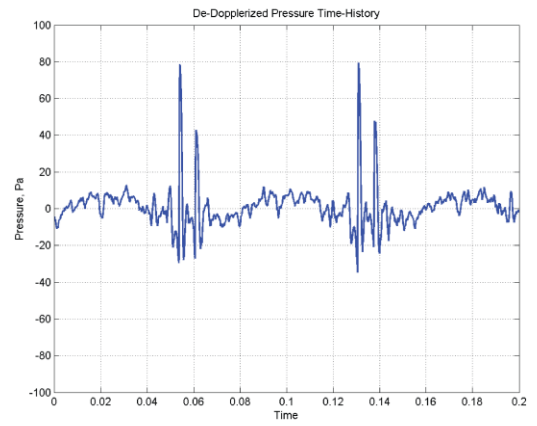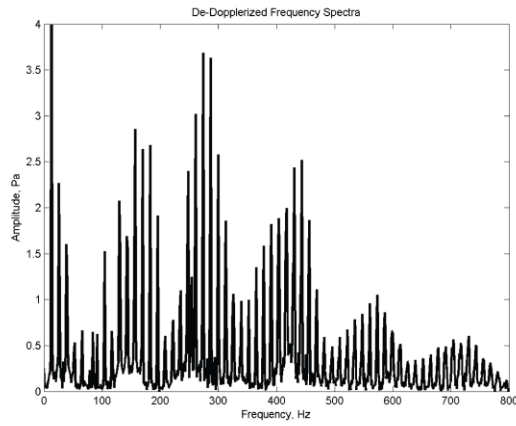**Figure 87: 6 Degree Descent**

Figure 88: 9 Degree Descent

C.2.2 60 kts, 30 Degree Bank Left Hand Turns

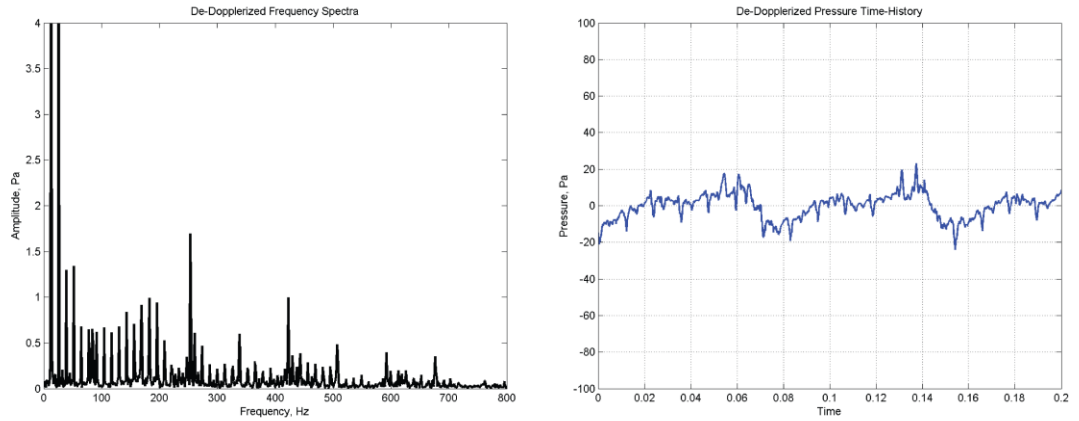**Figure 89: Level Flight**

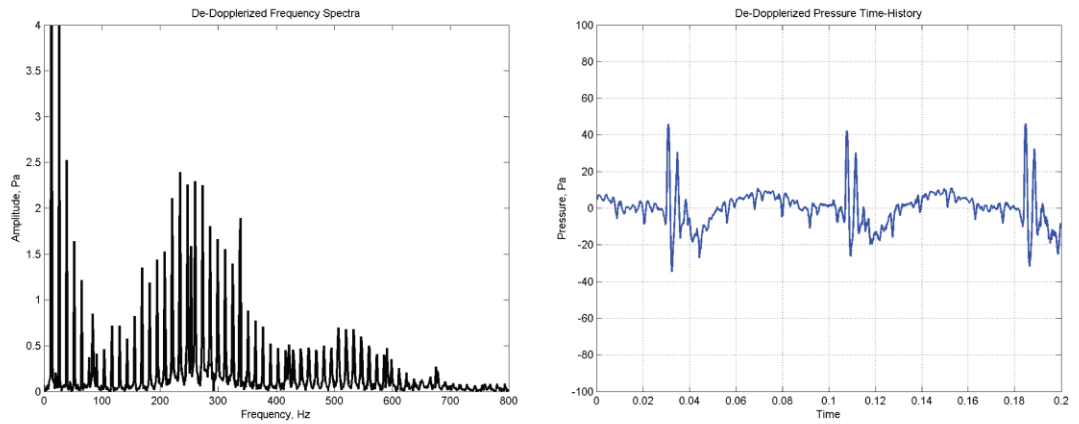**Figure 90: 3 Degree Descent**
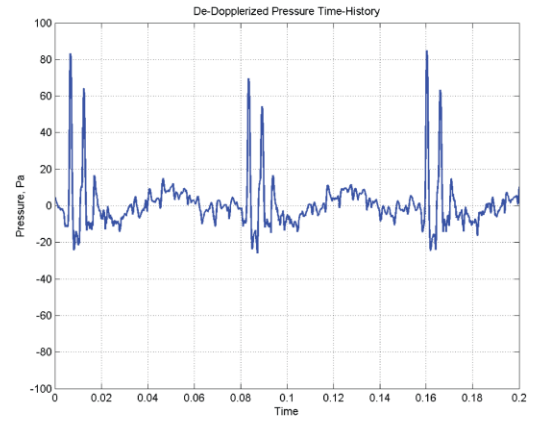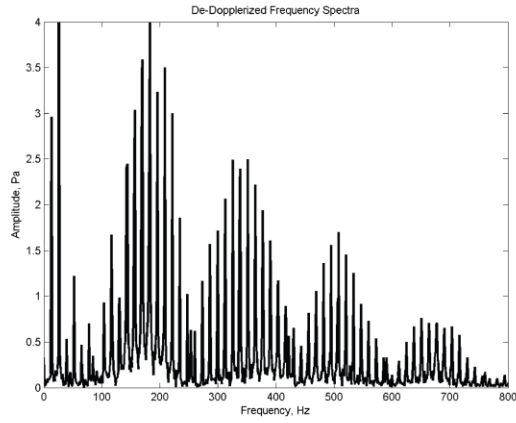
Figure 91: 6 Degree Descent
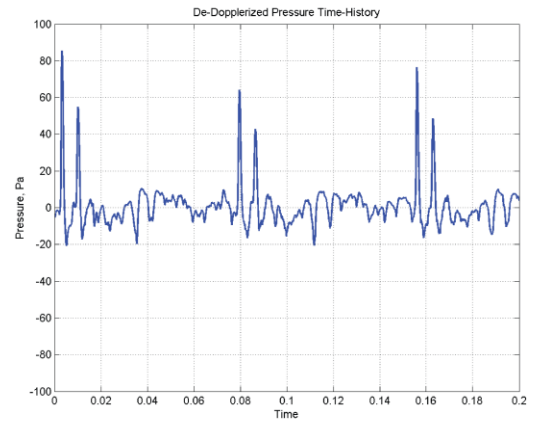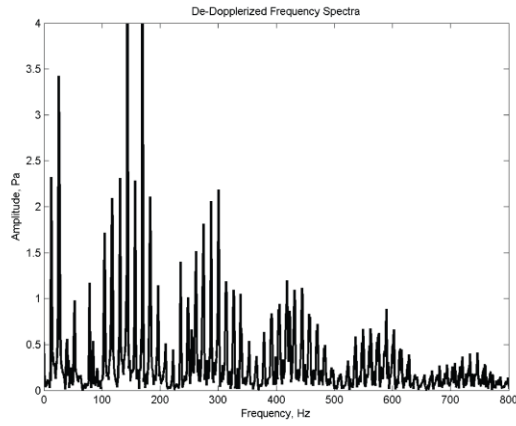
Figure 92: 9 Degree Descent

Appendix D: De-Dopplerization

D.1 The Doppler Effect

The Doppler Effect is the apparent shift in frequency of radiated noise as heard by the observer, due to the relative motion of the source and observer with respect to the medium transmitting the acoustic waves. In the case of ground noise measurement in a no wind environment, the observer and medium are stationary and the apparent shift in frequency is due to the motion of the source. The source deposits acoustic waves in the medium as it moves along the trajectory. These waves propagate from the locations in the medium where they are deposited along the trajectory at a finite speed of sound. (Fig. 93)
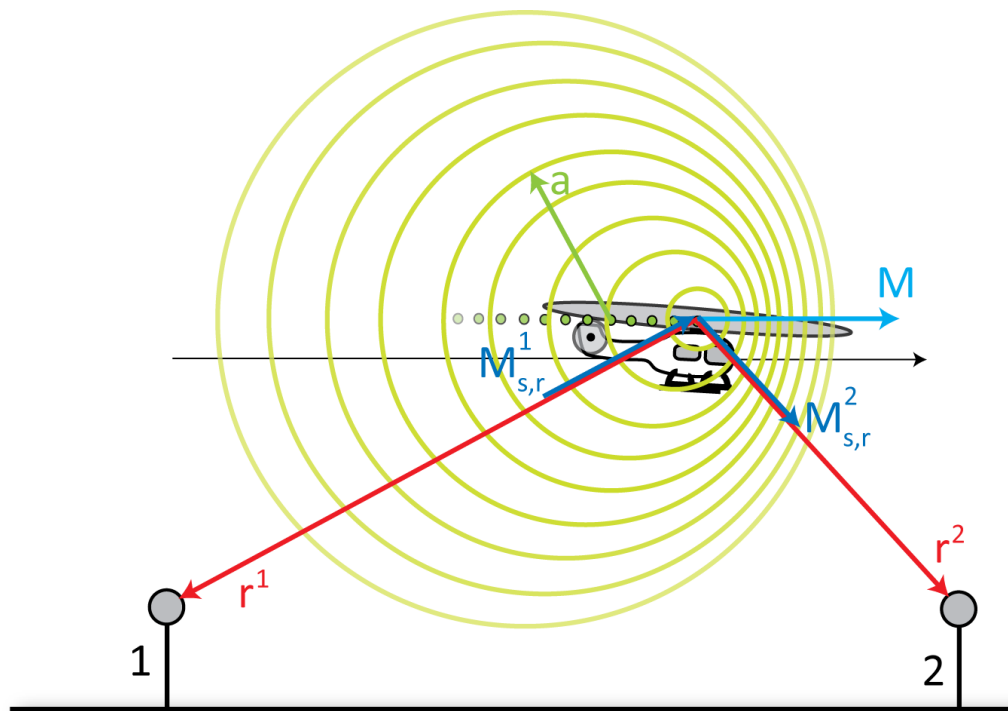
Figure 93: Doppler Effect Wave Bunching

For the subsonic source motion case, applicable to rotorcraft, the source will advance along its trajectory at a rate which is some fraction of sonic velocity at which the waves propagate. Therefore, to an observer fixed in the stationary medium these waves will appear to have a compressed wavelength ahead of the moving source, and an expanded wavelength behind.   The observed frequency is shifted based on the Mach number of source in the direction of the observer. This can be expressed through the following equation:

$$f_o = f_s + f_s\, M_{s,r} \quad (188)$$

The Mach number along the observer direction, $M_{s,r}$, can be determined by taking the dot product of the source's velocity vector against a unit vector in propagation direction oriented from source to observer.

D.2 Doppler Amplification

In addition to the shift in observed frequency due to the motion of the source relative to the observer, there is also an increase in amplitude of the emitted acoustic waves due to the motion of the source relative to the medium – this effect is called Doppler or convective amplification.   The simplest theoretical model of this effect is that of an acoustic monopole source in motion. Morse and Ingard show that as this simple moving source perturbs the medium, the resulting pressure field is related to the motion of the source with respect to the medium as measured along the direction of the observer: [50]

$$p^2 \sim \left(1 - \vec{M}_{s,m} \cdot \frac{\vec{r}}{|\vec{r}|}\right)^{-2} \quad (189)$$

Since the medium is assumed to be stationary, relative to the observer, this expression can be reduced to one involving only the Mach number of the source in the direction of the observer as in the Doppler frequency equations:

$$p^2 \sim \left(1 - M_{s,r}\right)^{-4} \qquad (190)$$

Dowling suggests, however, that the simple monopole source is a poor approximation for a physical compact source in motion.[51] Using a simple case of a compact pulsating sphere, it is suggested that the actual sound field created in the medium is more closely represented as:

$$p^2 \sim \left(1 - M_{s,r}\right)^{-6} \qquad (191)$$

The presence of a source with a very small, but finite, volume introduces more complex coupled multipole sources when in motion. These sources do have some effect on directivity of the convective amplification effect; however, the magnitude and geometry of this directivity cannot be analyzed without detailed knowledge of the true arrangement of sound sources on the helicopter and is typically ignored during the analysis of flight testing data. Practical flight testing of various aircraft has shown the exponent of the Doppler amplification expression varies between -4 and -8.5, although latter exponents are typically associated aircraft with significant quadrapole noise sources, such as jets.[52] Without more detailed knowledge of the helicopter source composition, it is difficult to select an appropriate Doppler amplification correction. In this thesis, the effects of Doppler amplification are neglected.

D.3 De-Dopplerization Process

The calculated shift in frequency can be used directly to correct frequency spectra derived from the observed time-history pressures for the Doppler frequency shift. However, there are several drawbacks to this approach. For example, when processing the observed time history spectra with an FFT, the window should encapsulate a periodic portion of the signal in order to avoid frequency leakage. When the FFT is performed on observed data from a moving source, the size of the window will vary with the shift in wavelength due to the Doppler Effect. Additionally, even within an appropriately sized window there will be some distortion since the Mach number of the source along the direction of the observer is continuously varying. Another problem with a frequency-domain De-Dopplerization approach is that it is difficult to apply the resulting data for noise source characterization. Separating main rotor and tail rotor noise could be attempted by analyzing the frequency spectra and counting noise at bins associated with main rotor harmonics to the main rotor and likewise for the tail rotor. However, even though the main and tail rotor blade passage frequencies are always non-integer multiples, there can be certain frequency bins where both main rotor and tail rotor noise contribute to the level – it is difficult to assess how much of this noise is generated by which source. Additionally, noise due to sources like BVI do not necessarily have well defined frequency-domain characteristics and may contribute significantly to frequency bins that are not associated with main or tail rotor harmonics. Frequency-domain De-Dopplerization also assumes each frequency bin represents a pure tone – this approach makes no consideration for phase shifts and cannot provide enough information in order construct an accurate representation of the time-history acoustic pressure emitted near the

source. Due to the drawbacks of the traditional frequency-domain De-Dopplerization

approach, an alternate physically consistent approach is advanced.
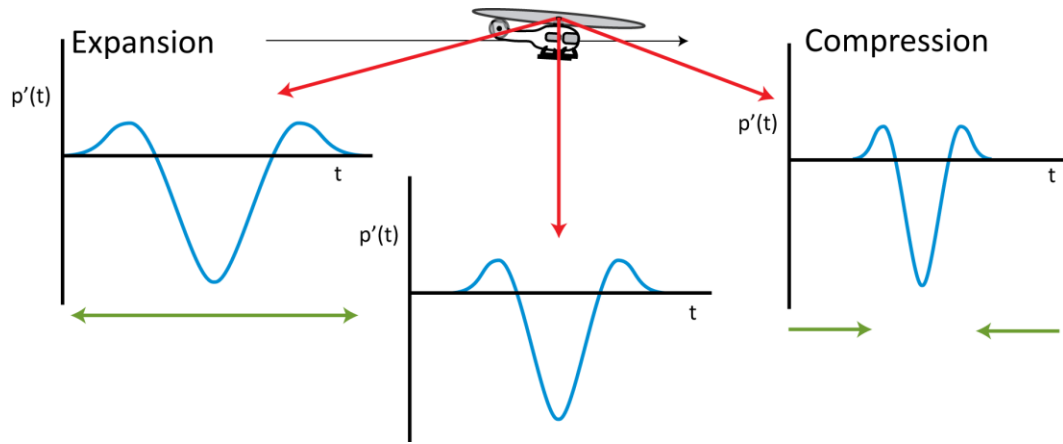
Figure 94: Doppler Effect in the Time Domain

The Doppler Effect can be viewed as a consequence of the retarded time equation

described previously. Each point of the emitted time-history pressure signal is heard by

the observer at some delayed time, due to the finite speed of sound in the medium. The

amount of this delay is based on the length of the propagation path between the source

and the observer, as the waves follow this path at the sonic velocity. Since the source is

in motion during ground-based acoustic measurement, the length of the propagation path

is continuously varying over time. The result is that as the source approaches to

observer, the amount of time delay is reduced – thereby compressing the signal and

resulting in an increase in frequency. Likewise, as the source moves away from the

observer, the amount of delay increases continuously, expanding the observed signal.

Consequently, it follows that an effective way of accounting for this effect is to evaluate

the retarded time equation at each point of the time-history acoustic pressure data instead

of only processing retarded time for each known position of the helicopter along the trajectory. (Fig. 94)

Evaluating the retarded time equation across the observed time-history pressure data requires some computation. First, a function describing the propagation path length as a function of the emission time must be constructed for each microphone. This is achieved by calculating the straight-line path length between the source and observer at each known position of the helicopter, and fitting a cubic spline as a function of time of emission to this data. Having formed this function describing the propagation path length, it is now possible to solve for the emission time associated with each sampled point of the observed time-history pressure.

$$t_s = t_o - \frac{r(t_s)}{a} \qquad (192)$$

Since the propagation path length is only known for emission times, the solution to the retarded time equation is not closed-form and must be solved iteratively. The secant method, defined by the recurrence below, was found to converge quickly and reliably.

$$t_s^{n+1} = t_s^n - \frac{t_s^n - t_s^{n-1}}{f(t_s^n) - f(t_s^{n-1})} f(t_s^n) \qquad (193)$$

Where the function $f(t_s^n)$ is a reformulation of the retarded time equation yielding a zero value when the correct emission time is selected:

$$f(t_s^n) = t_o - t_s - \frac{r(t_s)}{a} \qquad (194)$$

165

Simultaneously, it is possible to correct the signals at each sampled point for the spherical-spreading loss since the propagation length is found for each point – this eliminates the need to assume that the propagation distance of the acoustic data associated with a known location of the source is constant throughout the length of the entire window.
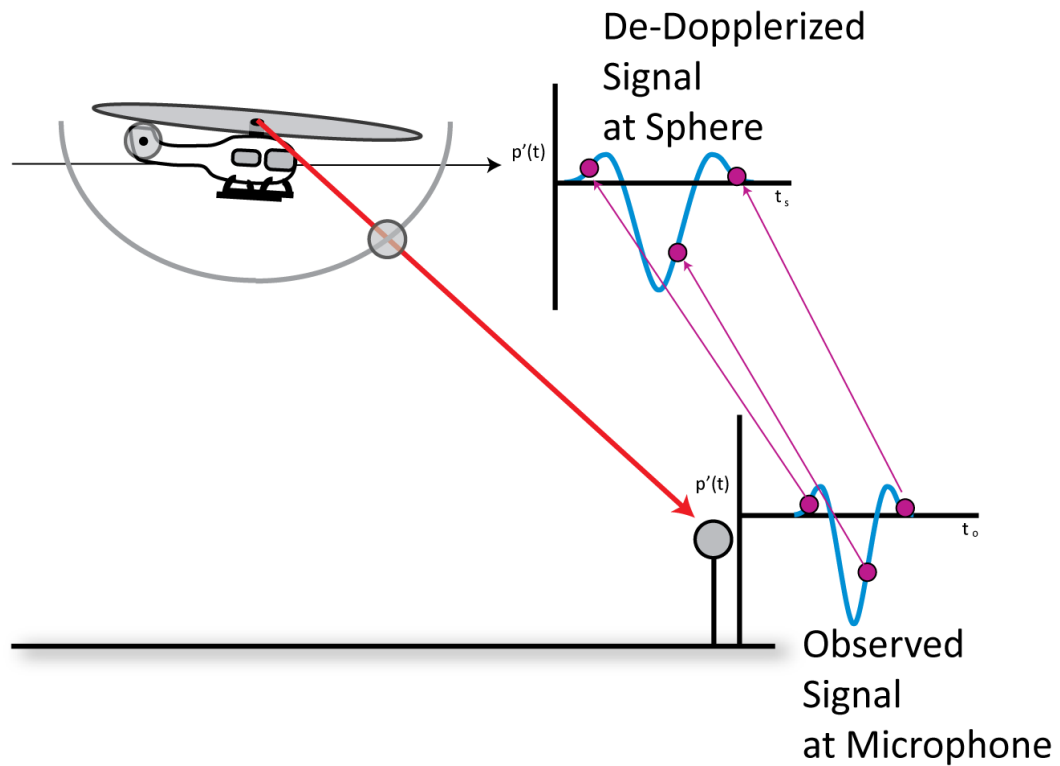
Figure 95: De-Dopplerization

Each microphone now has a time-history pressure signal associated to it and corrected to represent noise at the source, each with a distinct time vector. The sample period described by the time vector varies to account for the compression and expansion of the observed signal due to the Doppler Effect. However, the FFT process used to generate frequency spectra requires that the sample period be constant throughout the signal. A simple linear interpolation scheme is therefore applied to the De-Dopplerized time-

history pressure signal to resample it to a fixed sample period. In this case the same 30 kHz sampling rate used to capture the observed data is applied. This resampling process will introduce some high frequency error, but will accurately capture the noise of interest at frequencies below 10 kHz. [53]

Appendix E: Ground Reflection Analysis

The ground based array for the 2006 flight test was composed of ground board microphones.   If the ground board is assumed to be perfect acoustic reflector of infinite size and the microphone lies just on the surface of the board, acoustic waves incoming from any angle will reflect off the board at the measurement point.   The effect of this reflection on the measurement is well known and can be evaluated analytically.

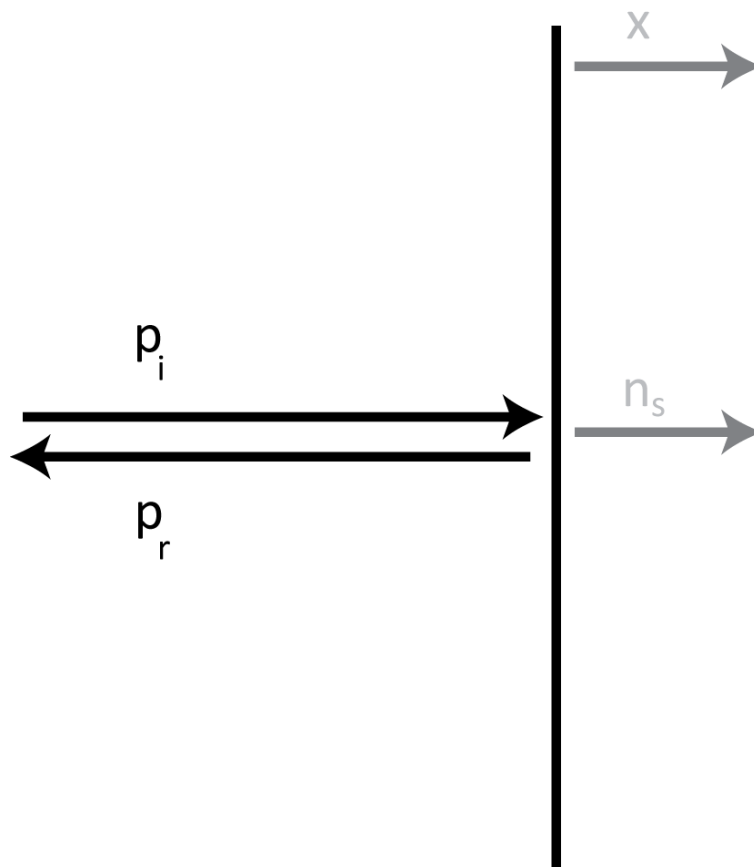## *E.1 Normal Reflections on Rigid Boundaries:*

Figure 96: Normal Reflection on Rigid Boundary

First, a boundary is established with the condition that a fluid particle located on the surface is displaced along with the surface, i.e.:

$$X_s(t) = x(t) \Rightarrow V_s(t) = v(t) \quad (195)$$

This can be generalized to three-dimensions by including the normal vector of the surface:

$$\vec{V}_s(t) \cdot \hat{n}_S = \vec{v}(t) \cdot \hat{n}_S \quad (196)$$

Consider the linearized momentum equation for a fluid element:

$$\frac{\partial \vec{v}}{\partial t} = -\frac{1}{\rho_0} \nabla p \quad (197)$$

Applying this relation to the fluid element on the boundary surface:

$$\rho_0 \frac{\partial}{\partial t} \vec{v} \cdot \hat{n}_S = -\nabla p \cdot \hat{n}_S \quad (198)$$

If the boundary is rigid, the surface motion will be zero and hence the fluid particle at the boundary will also have a zero particle velocity. Therefore at the boundary,

$$\nabla p \cdot \hat{n}_S = \frac{\partial p}{\partial \hat{n}_S} = 0 \quad (199)$$

Consider an incoming wave incident with the surface normal, along direction x. The reflected wave will be sent back along the opposite direction normal to the surface. Assume these waves take the form:

$$p_i(x,t) = Ae^{i\omega\left(t - \frac{1}{a_0}x\right)} \quad (200)$$

$$p_r(x,t) = Be^{i\omega\left(t+\frac{1}{a_0}x\right)} \quad (201)$$

Since linearity is assumed, the pressure at any point is the superposition of the two waves:

$$p(x,t) = p_i(x,t) + p_r(x,t) \quad (202)$$

Therefore, the rigid boundary condition is evaluated as:

$$\left[\frac{\partial p_i}{\partial x} + \frac{\partial p_r}{\partial x}\right]_{x=0} = 0 \quad (203)$$

$$-\frac{i\omega}{a_0}Ae^{i\omega t} + \frac{i\omega}{a_0}Be^{i\omega t} = 0 \quad (204)$$

$$A = B \Rightarrow p_i(0,t) = p_r(0,t) \quad (205)$$

Due to the linearized superposition relation, this implies that the acoustic pressure seen by the particle at the boundary is twice that of the incoming wave:

$$p(0,t) = p_i(0,t) + p_r(0,t) = 2\,p_i(0,t) \quad (206)$$

This analysis results in a 6 dB increase in the measured sound pressure level of incoming waves when using an ideal ground board. In practice, however, the board is not perfectly rigid and the microphone does not measure the pressure of only the fluid particle just on the surface boundary. Experimental studies show that the use a plywood ground board tends to produce approximately a 5 dB increase in measured SPL for all frequencies below 4 kHz – as frequencies exceed 4 kHz, the effect can be greater or lesser than 5 dB depending on the incidence angle and frequency.[32] The BVISPL frequency range extends to about 1 kHz; for this reason, an assumed 5 dB decrease in

measured levels for all frequencies of interest is valid for this application.   Furthermore, at grazing incidence angles, the geometry of the finite ground board becomes important since in practical applications the microphone cannot be mounted perfectly flush with the ground board surface and may measure signals reflected or refracted from the soft ground outside of the ground board. In this study, no measurements were made from incident angles within 15 degrees of the ground plane – ground board edge effects are generally considered negligible above this range.

In 2007, the array was composed of both ground board mounted microphones and microphones mounted 1.2 meters off the ground, as per FAA certification standard. As mentioned previously, the wired microphones were vulnerable to failure and for many test runs the ground board microphones were unavailable. In order to evaluate noise levels across the full range of directivity angles, the 1.2 meter microphones must be included into the array.

An initial comparison of the data revealed that for similar conditions, the measured noise levels differed significantly between the 2006 NASA Langley ground board measured data and the 2007 Bell Helicopter FAA certification microphone data.   The BVISPL levels measured by the center-channel microphone for 2006 and 2007 are compared in Figure 97.   Both spherical spreading and atmospheric absorption are corrected for, normalizing the data to 100 feet across all incidence angles. The BVISPL levels are plotted against the elevation angle between the helicopter and microphone (at the correct retarded time), with zero degrees representing the helicopter in front of the microphone and 180 degrees the helicopter behind the microphone at the end of the flyover run. The NASA Langley ground board microphone levels are then reduced by 5

dB to account for the known pressure doubling effect.

BVISPL Comparison of Center Channel Microphone Levels over Elevation normalized to 100 ft, Ground Board Adjusted
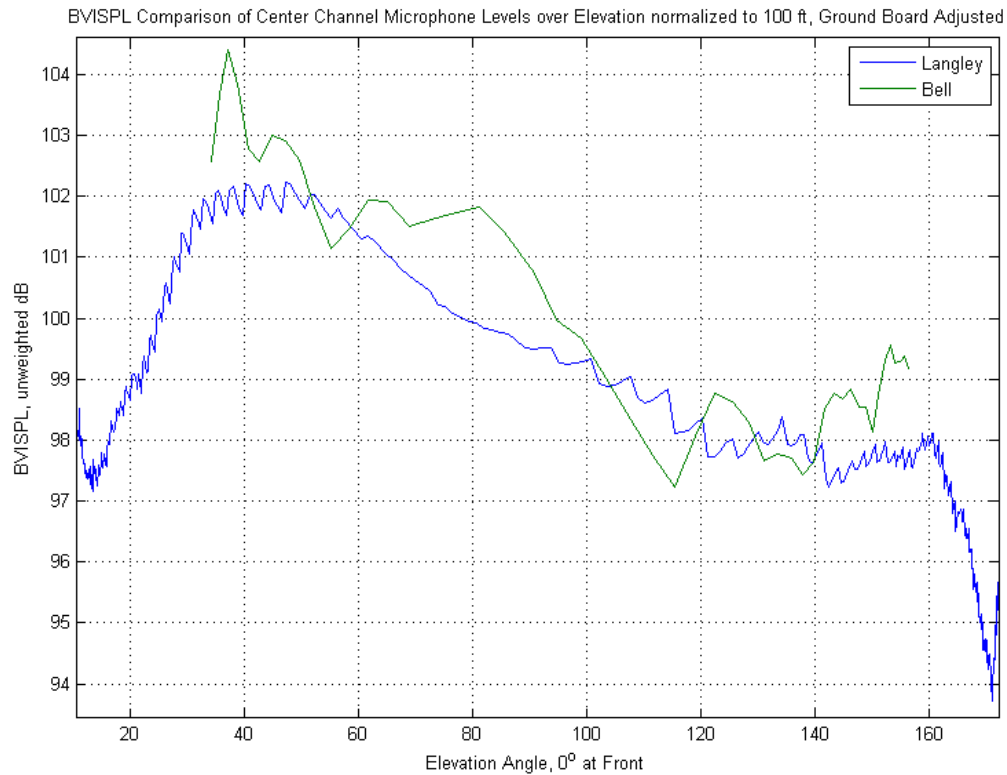
Figure 97: Comparison of Ground Board and 1.2m Microphone Flyover Data

E.2 Oblique Reflections on Rigid Boundaries:

The 2007 1.2 meter microphone data is shown to vary from the ground board microphone data in either direction, depending on the incidence angle of the measurement. Examination of the frequency spectra shows that for any given angle, some of the measured frequencies are augmented and some are diminished in the 1.2 meter microphone signal as compared to the ground board. This suggests that the 1.2 meter microphones are vulnerable to unwanted measurement of the reflected signal for this frequency range. This reflected signal can interfere with the free-field measurement

either constructively or destructively, depending on the frequency and incidence angle of the radiated noise.
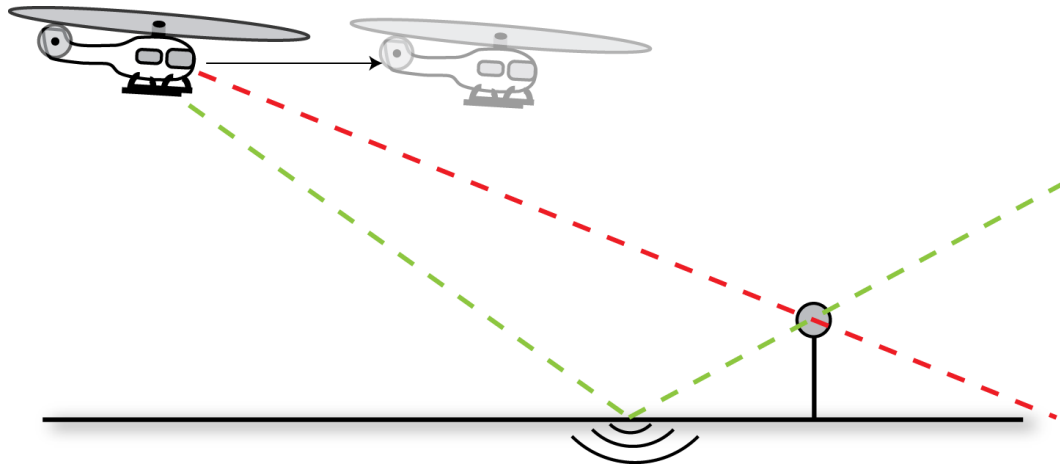
Figure 98: Direct and Reflected Propagation Paths

When the microphone is placed above the ground plane, the reflected signal and the direct signal now travel along different paths. (Fig. 98) In the absence of wind or temperature gradients, the direct path is simply the straight line between the source, at the time of emission, and the microphone at the time of observation.   The reflected path is longer, bouncing off the ground at some point between the source and the observer and then reflecting from this point on the ground back up to the microphone.   Analysis shows that the incidence angle between the ground and the reflected path will be the same on both sides of the reflection.
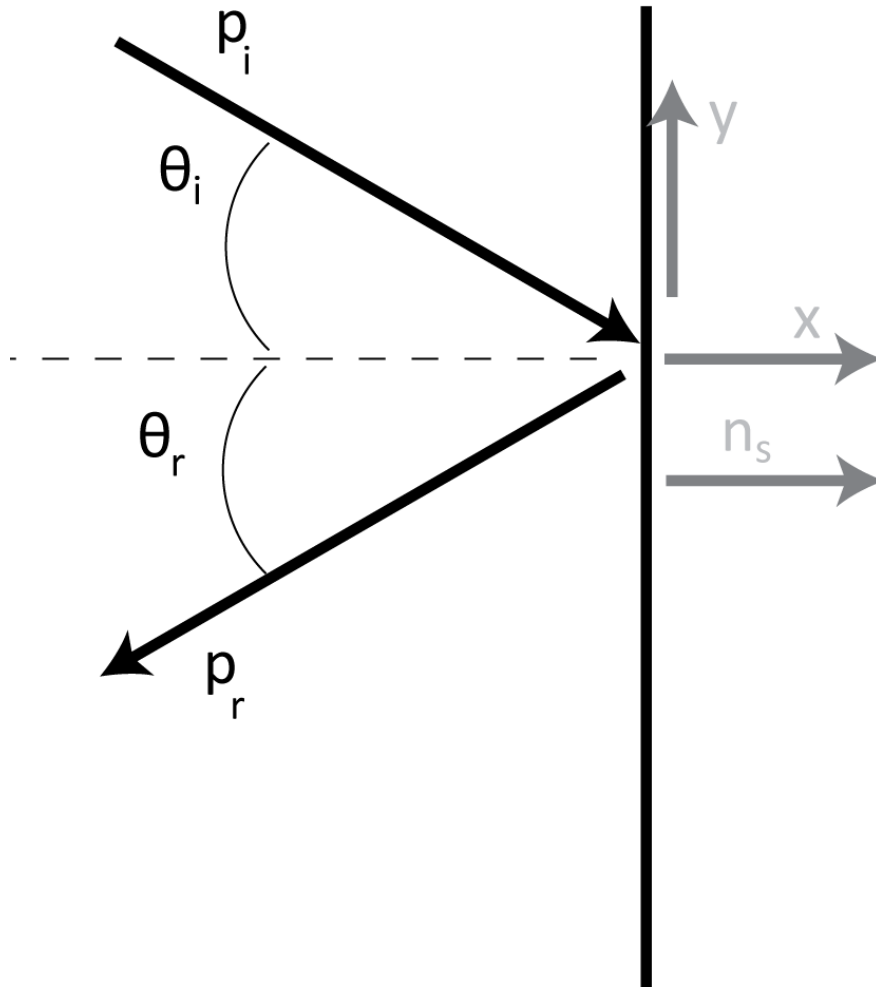
Figure 99: Oblique Reflection on Rigid Boundary

The case of an oblique reflection can again be seen by considering the linearized momentum equation of a fluid element. This time, an incoming wave is considered which is not aligned with the surface normal vector. The pressure of this wave is represented along the direction of propagation by the distance s_i:

$$p_i(x, y, t) = Ae^{i\omega\left(t - \frac{1}{a_0}s_i\right)} \qquad (207)$$

The direction of propagation can be expressed along the surface coordinates by relating it to the angle of incidence:

$$s_i = x \sin \theta_i - y \cos \theta_i \qquad (208)$$

$$p_i(x, y, t) = A e^{i\omega \left(t - \frac{x}{a_0} \sin \theta_i + \frac{y}{a_0} \cos \theta_i\right)} \qquad (209)$$

Similarly, the pressure of the reflected wave can be considered by evaluating the distance along the direction of propagation of the reflected wave:

$$s_r = \hat{n}_r \cdot \vec{x} = x \sin \theta_r + y \cos \theta_r \qquad (210)$$

$$p_r(x, y, t) = B e^{i\omega \left(t + \frac{x}{a_0} \sin \theta_r + \frac{y}{a_0} \cos \theta_r\right)} \qquad (211)$$

For a rigid boundary, the fluid particle attached to the surface will not move in the direction normal to that surface, i.e.:

$$\vec{v} \cdot \hat{n}_S = \vec{v}_i \cdot \hat{n}_S + \vec{v}_r \cdot \hat{n}_S = 0 \qquad (212)$$

Applying the Euler relation for a plane wave yields:

$$\vec{v}_i \cdot \hat{n}_S = \frac{p_i}{\rho_0 \, a_0} \hat{n}_i \cdot \hat{j} = -\frac{p_i}{\rho_0 \, a_0} \cos \theta_i \qquad (213)$$

$$\vec{v}_r \cdot \hat{n}_S = \frac{p_r}{\rho_0 \, a_0} \hat{n}_r \cdot \hat{j} = \frac{p_i}{\rho_0 \, a_0} \cos \theta_r \qquad (214)$$

Substituting the pressure equations into the boundary relation at the incidence location y=0,

$$-\frac{A e^{i\omega \left(t - \frac{x}{a_0} \sin \theta_i\right)}}{\rho_0 \, a_0} \cos \theta_i + \frac{B e^{i\omega \left(t + \frac{x}{a_0} \sin \theta_r\right)}}{\rho_0 \, a_0} \cos \theta_r = 0 \qquad (215)$$

This condition is then satisfied for $\theta_i = \theta_r$ on the boundary, with the resulting pressure at this boundary equal to twice that of the incoming wave, as in the normal incidence case.

E.3 Normal Reflections on Soft Boundaries

In practice, the ground is not well modeled as a rigid surface. Some portion of acoustic waves hitting the ground will be reflected back into the air, but some portion will be absorbed by the ground. In addition to the absorption effect, there is also a phase delay in the ground reflection process. Both the absorption and phase delay can be modeled by considering a complex ground impedance factor.
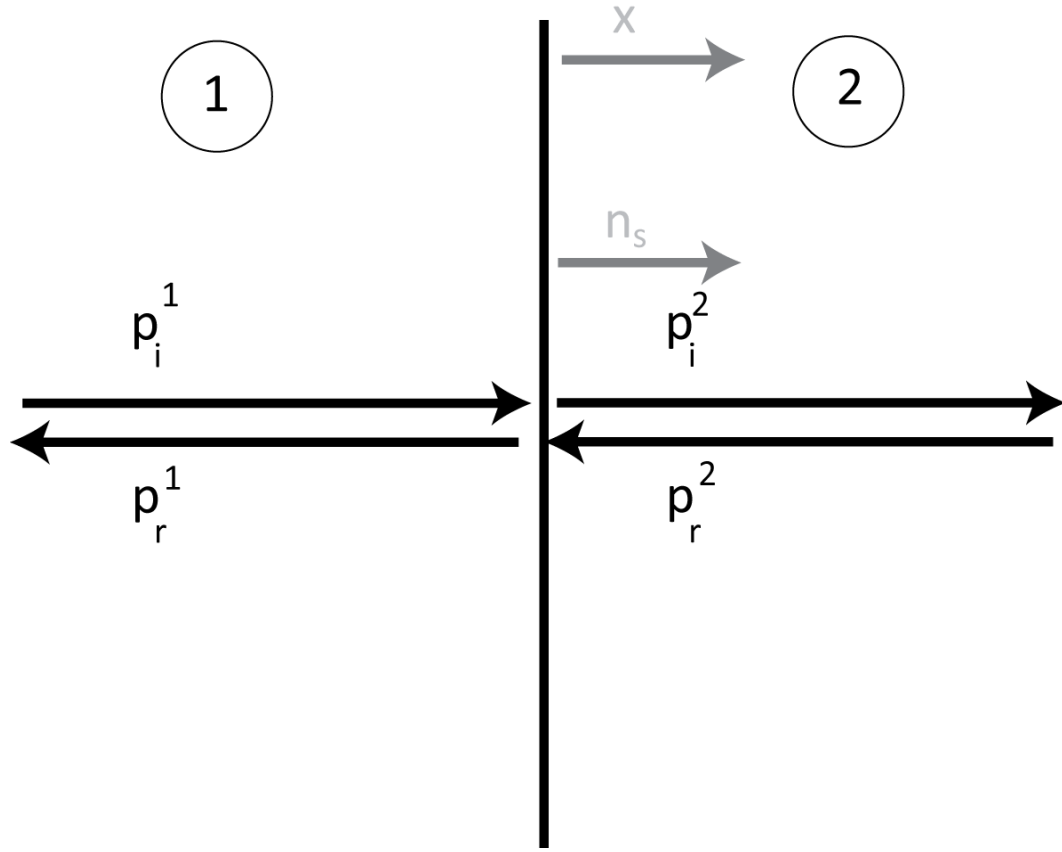
Figure 100: Normal Reflection on Soft Boundary

. The impedance is frequency dependant and defined as the ratio of the acoustic pressure to the particle velocity at some point on the surface:

$$Z(x, \omega) = \frac{\hat{p}(x,\omega)}{\hat{v}(x,\omega) \cdot \hat{n}_S(x)} \quad (216)$$

The impedance is complex: the real component of the impedance is called the resistance and the complex component the reactance. These components are often expressed as:

$$Z = R + i\chi \quad (217)$$

Consider the case of a plane wave consisting of a single frequency crossing from a medium with one impedance characteristic to another normal to the boundary. At this single frequency, the acoustic impedance of the material may be considered as:

$$Z_1 = \rho_1 a_1, \; Z_2 = \rho_2 a_2 \quad (218,219)$$

At the boundary, the particle velocity and pressure boundary conditions still hold – these quantities must be the same on both the left and right sides of the boundary. Again, taking the superposition of the left and right running waves at the boundary x=0, the following equations boundary equations are developed:

$$p_i^1(0,t) + p_r^1(0,t) = p_i^2(0,t) + p_r^2(0,t) \tag{220}$$

$$\Rightarrow A e^{i\omega\left(t-\frac{1}{a_1}x\right)} + B e^{i\omega\left(t+\frac{1}{a_1}x\right)} = C e^{i\omega\left(t-\frac{1}{a_2}x\right)} + D e^{i\omega\left(t+\frac{1}{a_2}x\right)}, x = 0 \tag{221}$$

$$\frac{1}{\rho_1}\left[\frac{\partial p_i^1}{\partial x} + \frac{\partial p_r^1}{\partial x}\right]_{x=0} = \frac{1}{\rho_2}\left[\frac{\partial p_i^2}{\partial x} + \frac{\partial p_r^2}{\partial x}\right]_{x=0} \tag{222}$$

$$-\frac{i\omega}{\rho_1 a_1} A e^{i\omega t} + \frac{i\omega}{\rho_1 a_1} B e^{i\omega t} = -\frac{i\omega}{\rho_2 a_2} C e^{i\omega t} + \frac{i\omega}{\rho_2 a_2} D e^{i\omega t} \tag{223}$$

Next, consider that the sound source lies in the first medium. If the second medium is assumed to extend infinitely there will be no left-running wave in the second medium and D can be set to zero. If the pressure and velocity conditions are now evaluated and combined to relate the magnitude of the incident wave to the reflected wave, the result is:

$$B = \frac{\rho_2 a_2 - \rho_1 a_1}{\rho_2 a_2 + \rho_1 a_1} A \quad (224)$$

178

This ratio is defined as the reflection coefficient, and can be written generally in terms of impedance:

$$Q = \frac{Z_2 - Z_1}{Z_2 + Z_1} \qquad (225)$$

For the interaction between air and the complex impedance of the ground this can be written over a range of frequencies as:

$$Q(\omega) = \frac{Z(\omega) - Z_0}{Z(\omega) + Z_0} \qquad (226)$$

This is often written in terms of the non-dimensional specific acoustic impedance by relating the ground impedance to the characteristic impedance of air:

$$Q = \frac{\frac{Z}{\rho_0 a_0} - 1}{\frac{Z}{\rho_0 a_0} + 1} \qquad (227)$$

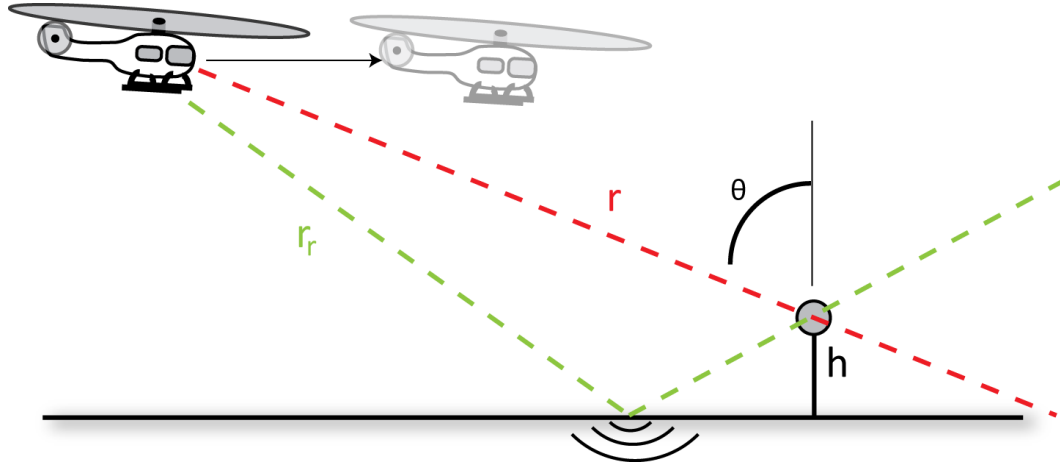## E.4 Oblique Reflections on Soft Boundaries

Figure 101: Flight-Test with Above Ground Microphones, Normal Reflection on Soft Boundary

In a similar manner as to the analysis of an oblique reflection off of a rigid surface, the oblique reflection off of an acoustic medium may be considered. (Fig. 101) This yields a similar expression for the oblique reflection coefficient:

$$Q = \frac{\frac{Z}{\rho_0 a_0} \cos\theta - 1}{\frac{Z}{\rho_0 a_0} \cos\theta + 1} \quad (228)$$

This reflection coefficient is complex and is expressible as a magnitude and phase:

$$Q = |Q| e^{-i\delta} \quad (229)$$

These components of the reflection coefficient can be found from the real and complex parts of the ground impedance through the following relations:

$$|Q| = \frac{\sqrt{[|Z/\rho_0 a_0|^2 \cos^2\theta - 1]^2 + 4(\chi/\rho_0 a_0)^2 \cos^2\theta}}{|Z/\rho_0 a_0|^2 \cos^2\theta + 1 + 2(R/\rho_0 a_0)\cos\theta} \quad (230)$$

$$\delta = \sin^{-1}\left\{ \frac{2(\chi/\rho_0 a_0)\cos\theta}{\sqrt{[|Z/\rho_0 a_0|^2 \cos^2\theta - 1]^2 + 4(\chi/\rho_0 a_0)^2 \cos^2\theta}} \right\} \quad (231)$$

180

E.5 Ground Reflection Interference Correction

If the sound source is assumed to be stationary, omni-directional, and emitting a pure tone, geometry and the retarded time equation can be applied to assess the change in effective pressure amplitude on measured sound due to the interference of the reflected signal on the direct signal. Thomas describes the change in SPL of this pure tone as: [54]

$$\Delta N = 10 \log \left[1 + \left| \frac{r_r}{r} Q \right|^2 + 2 \left| \frac{r_r}{r} Q \right| \cos \left(2\pi \frac{(r_r - r)}{\lambda} + \delta \right) \right] \qquad (232)$$

The applicability of this relation can be extended to random noise inside of a frequency band, as described by Franken.[55] The equation is then modified to describe the change in SPL in the ith frequency band as follows:

$$\Delta N_i = 10 \log \left[1 + \left| \frac{r_r}{r} Q_i \right|^2 + 2 \left| \frac{r_r}{r} Q_i \right| \frac{\sin \left(\mu \frac{(r_r - r)}{\lambda_i} \right) \cos \left(2\pi \frac{\beta (r_r - r)}{\lambda_i} + \delta_i \right)}{\mu \frac{(r_r - r)}{\lambda_i}} \right] \qquad (233)$$

Where the parameters β and μ are defined as:

$$\mu = \frac{2\pi \, \Delta f}{2 f_i}, \quad \beta = 2\pi \sqrt{1 + \left(\frac{\Delta f}{2 f_i} \right)^2} \qquad (234,235)$$

This expression neglects refraction effects and assumes the source is omni-directional and stationary – this is because the signal emitted along the reflected path is assumed to be the same as that sent along the direct path at the time of emission. The omni-directional assumption may be violated so long as the signal emitted along the direct path is similar to that emitted along the reflected path. Likewise, the stationary source assumption may be violated if the helicopter has not changed position significantly

between the time of emission of the reflected path and the time of emission of the direct path for the same time of observation. For a microphone relatively low to the ground, these conditions are met since the geometry of the reflected path is similar to the geometry of the direct path. As the microphone is raised above the ground, the emission angle and retarded time difference between the paths increases and the validity of this correction is reduced. It can also be seen from the equation that as the frequency of the signal is decreases, increasing the wavelength, the sensitivity of the cosine function to the phase delay is increased. This implies that violations of the assumptions of the equation will have a more significant effect on the SPL for lower frequencies versus higher frequency. This method of ground reflection is considered valid for FAA certification microphone heights within the BVISPL frequency range. However, in many cases tower microphones are used for measurement of in-plane noise radiation. Of particular interest in this case are the lower frequency fundamental noise sources of the rotor. The ground correction method described above would not be valid for these conditions. Instead, a more comprehensive method allowing for a moving source with significant directivity would be required. One such approach would be to perform ray tracing of a virtual helicopter flying the test trajectory and identify the emitted rays which intersect with the microphone locations. The time of emission and directivity of these rays could then be matched to an observation time and incidence angle of the intersection of a direct ray with a microphone. By comparing all of the observed signals with their associated direct and reflected path measurements, it should be possible to correct for the reflected signals. However, such a procedure would be very complex and computationally expensive.

The ground reflection interference correction requires knowledge of the ground impedance characteristics. Direct measurement of ground impedance is difficult and provides results specific only to certain points on the terrain at a certain temperature and humidity. For this reason, ground impedance models are often used to estimate the complex ground impedance for a specific terrain type. One commonly used model is that developed by Delany and Bazley. [33] They relate the complex ground impedance function to a single flow resistivity parameter, which is calculated for several terrain types. This empirically derived model is a function of frequency, as shown below:

$$\frac{R}{\rho_0 a_0} = 1 + 9.08 \left(\frac{f}{\sigma}\right)^{-0.75} \qquad (236)$$

$$\frac{X}{\rho_0 a_0} = -11.9 \left(\frac{f}{\sigma}\right)^{-0.73} \qquad (237)$$

The flow resistivity of the ground is defined as the ratio of the dynamic viscosity of the air to the static porosity of the ground – in effect this is a measure of the permeability of the ground. This can be directly measured with special equipment or can be assumed from the known classification of the terrain. For the soft farm field used in the 2007 test, an estimated value for a "cabbage field" of 200 CGS Rayls is assumed. [34]

E.6 Example

A hemisphere was generated from the 2007 data set for a level flight run of the Bell 206 at approximately 60 knots airspeed with 492 foot altitude above ground level. FAA Noise certification microphones were used for all positions except the two endpoints of the array, where UMD ground board microphone measurements were made. The resulting BVISPL noise contours were generated, with spherical spline basis interpolation used to fill in the values between data sites (see interpolation section for detail).

Overall peak values are similar between the corrected (Fig. 103) and uncorrected (Fig. 102) hemispheres, however, as indicated by the microphone trace comparison examined previously, there substantial variation in the levels over the uncorrected hemisphere due to the change in the reflection geometry as the helicopter passes over the array. The uncorrected hemisphere is therefore less smooth and does not reflect the shape of the physical noise contours as well as the corrected sphere.
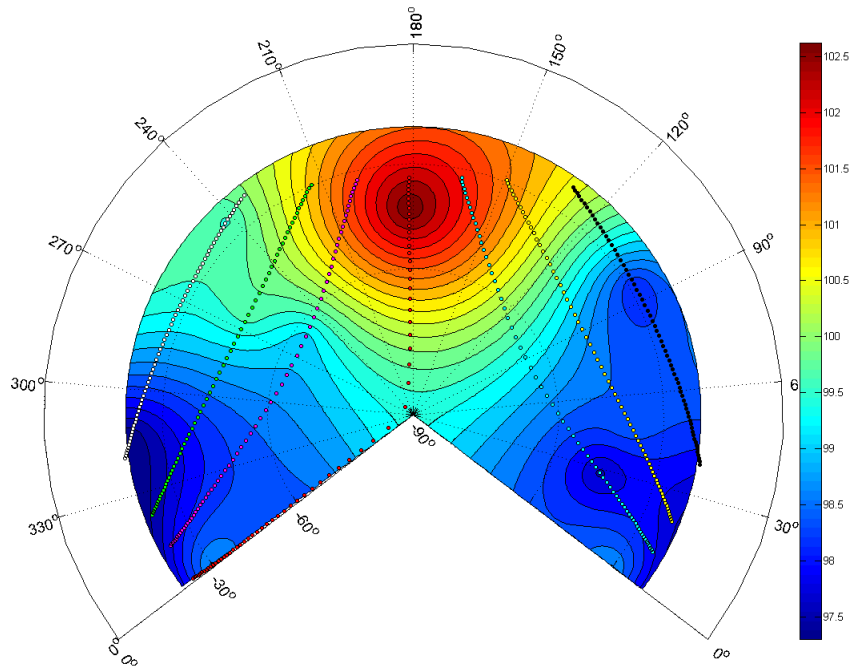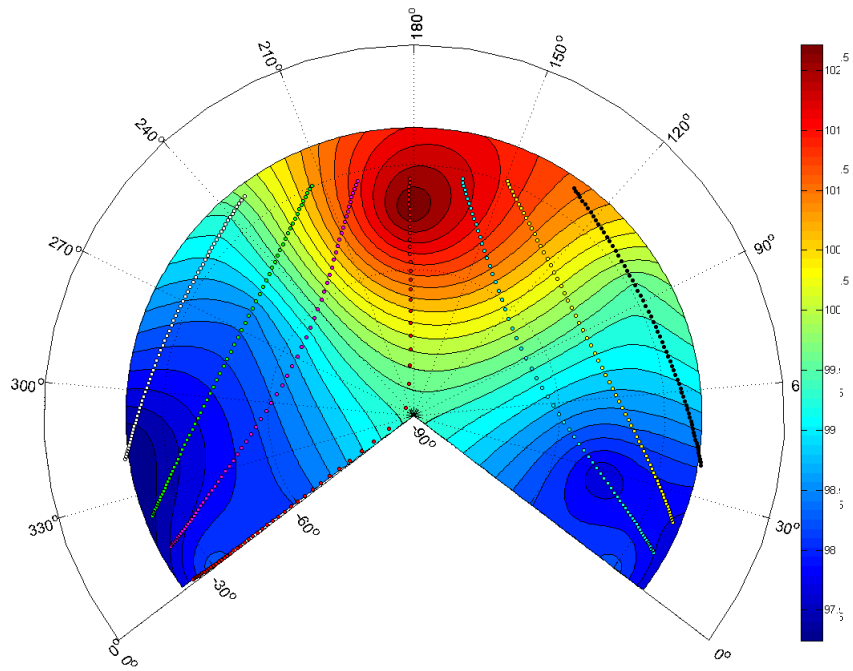
Figure 103: Example Case: Uncorrected Hemisphere

Figure 102: Example Case: Ground Reflection Corrected Hemisphere

Appendix F: Turning Flight Interpolation Comparison

The approaches used previously by RNM are compared against the new radial basis approach for the scattered BVISPL data processed for the 6° descending right hand turn case. The flight condition, and hence the acoustic state of the helicopter, was relatively unsteady over the duration of this run. However, the helical trajectory yields a less sparse distribution of measurements across the hemisphere. Figure 104 shows the results of the triangulation based scheme on this data. Similar to the straight line results, significant distortion is seen due to the skewed interpolation over high aspect ratio triangles.
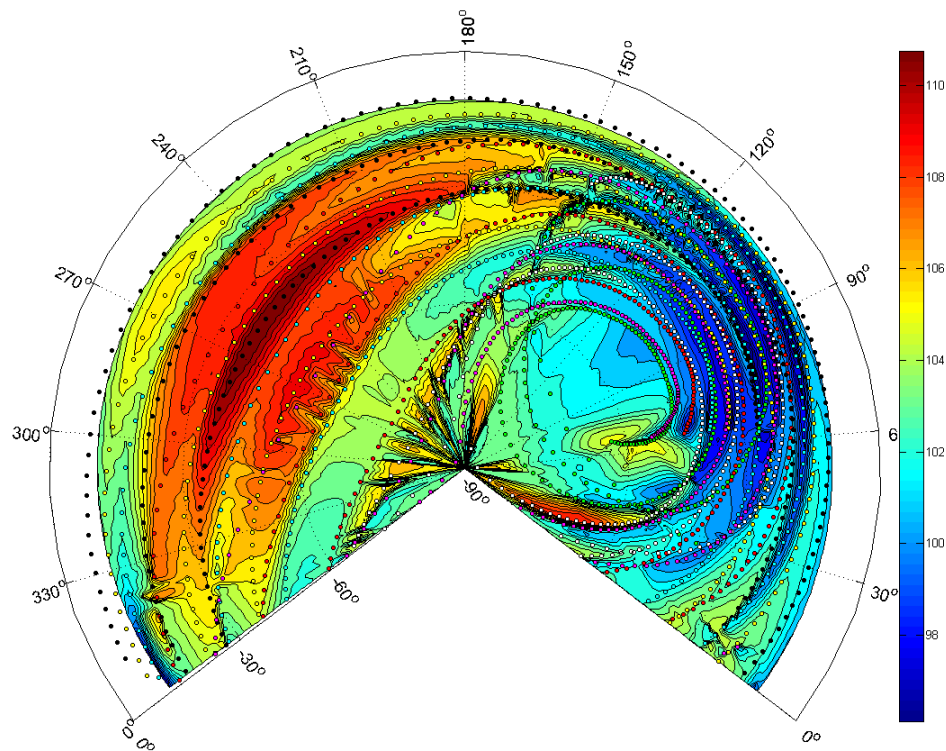

Figure 104: Triangulation Interpolation, 60kts, 6 Degree Descent, Right Hand Turn

Figure 105 shows the interpolated BVISPL contours produced by the spline mesh interpolation scheme. As in the straight line case, this method tends to skew results which align with the mesh of lines of constant azimuths and elevations. Since, in the turning flight case, the microphone measurements traces follow azimuthal lines, significant distortion is seen across the sparse region yielding highly uneven and nonphysical contours – this distortion amplifies the unsteadiness of the acoustics.
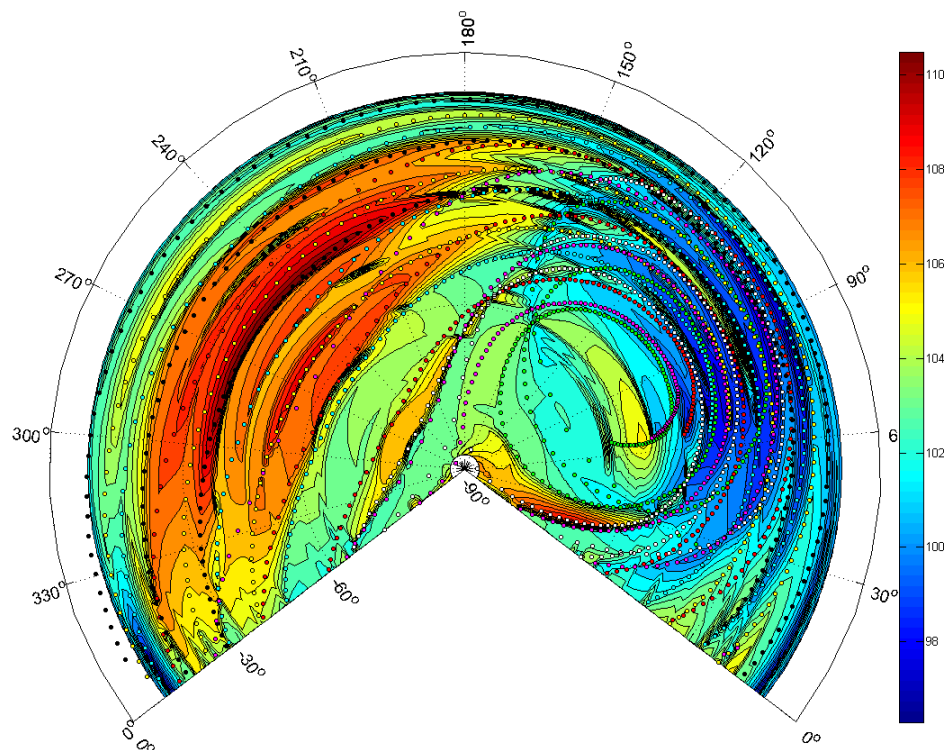

Figure 105: Spline Mesh Interpolation, 60 kts, 6 Degree Descent, Right Hand Turn
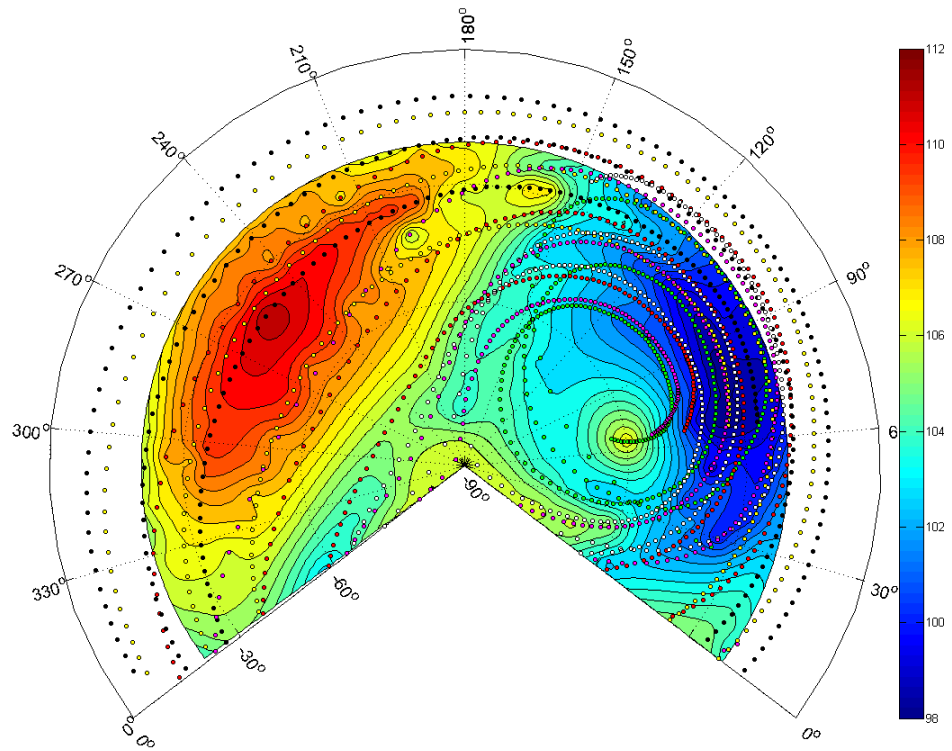
Figure 106: Spherical Spline RBF Interpolation kts, 6 Degree Descent, Right Hand Turn

The radial basis function with spherical splines bases interpolation scheme is displayed in figure 106. The RBF scheme yields smoother contours with no skewing in any direction. The general shape of the BVISPL hotspot on the left-hand side of the horizon-fixed sphere (below the plane of the banked rotor) is now evident. Due to unsteadiness in the flight condition of the helicopter throughout the run, the BVISPL contours are still somewhat uneven. However, the resulting BVISPL contours are markedly smoother and more physical seeming than those produced by the standard RNM interpolation schemes.

188

References

[1] Farassat, F. "Theory of Noise Generation from Moving Bodies with an Application to Helicopter Rotors", NASA TR R-451, December 1976.

[2] Schmitz, F.H., "Rotor Noise," Chapter 2, Ed. Hubbard, H.H., <u>Aeroacoustics of Flight Vehicles, Theory and Practice, Vol. 1: Noise Sources</u>, NASA Reference Publication 1258, 1995.

[3] Connor, A.B. and Martin, R.M. "Correlation of Helicopter Impulsive Noise from Blade-Vortex Interaction with Rotor Mean Inflow", NASA TP 2650, March 1987.

[4] Duque, E., et *al.* "Revolutionary Physics-Based Design Tools for Quiet Helicopters" presented at the 44th AIAA Aerospace Sciences Meeting and Exhibit, Reno, NV, January 2006.

[5] Perez, G. and Costes, M., "A New Aerodynamic & Acoustic Computation Chain for BVI Noise Prediction in Unsteady Flight Conditions", presented at the American Helicopter Society 60th Annual Forum, Baltimore, MD, June 2004.

[6] Forsyth, D.W., Gulding, J., and DiPardo, J.. "Review of Integrated Noise Model (INM) Equations and Processes", NASA CR-2003-212414, May 2003.

[7] Fleming, G.G. *et al.* "Assessment of Tools for Modeling Aircraft Noise in National Parks", FICAN, March 2005.

[8] R.M. Martin, *et al.* "Wake Geometry Effects on Rotor Blade-Vortex Interaction Noise Directivity", NASA TP 3015. November 1990.

[9] Sim, W.C., Schmitz, F.H., "Acoustic Phasing and Amplification Effects of Single Rotor Helicopter Blade-Vortex Interactions," presented at the American Helicopter Society 55th Annual Forum, Montreal, Canada, May 1998.

[10] Schmitz, F.H., and Yu, Y.H., "Helicopter Impulsive Noise: Theoretical and Experimental Status", NASA TM 84390, November 1983.

[11] Conner, D.A., and Page, J.,"A Tool for Low Noise Procedures Design and Community Noise Impact Assessment: the Rotorcraft Noise Model (RNM)", presented at the AHS International Meeting on "Advanced Rotorcraft Technology and Life Saving Activities", Heli Japan, Japan, November 2002.

[12] Conner, D.A., Burley, C.L., and Smith C.D. "Flight Acoustic Testing and Data Acquisition for the Rotorcraft Noise Model (RNM)", presented at the American Helicopter Society 62nd Annual Forum, Phoenix, AZ, May 2006.

[13] Page, J.A., *et al.*, 'Rotorcraft Noise Model (RNM 5.0) Technical Reference and User Manual", Wyle Research Report No. WR 05-02, May 2005.

[14] Fasshauer, G.E. and Schumaker, L.L.,"Scattered Data Fitting on the Sphere", ed. Daehlen, M., Lyche, T. and Schumaker, L.L., <u>Mathematical Methods for Curves and Surfaces II,</u> 117-166, Vanderbilt University Press, Nashville & London, 1998.

[15] Freeden, W., Schneider, F. and Schreiner, M., "Gradiometry – An Inverse Problem in Modern Satellite Geodesy", Ed. Engle, H.W., <u>GAMM-SIAM Symposium on Inverse Problem: Geophysical Applications</u>, 179-239. SIAM, 1997.

[16] Browne, R., *et al.* "Prediction of Helicopter Noise Contours for Land Use Planning", presented at the 10th AIAA/CEAS Aeroacoustics Conference, Manchester, Great Britain, May, 2004.

[17] Putnam, T. "Acoustic Interference by Reflection Application to the Sound Pressure Spectrum of Jets", NASA TTF-14, 185, 1972.

[18] Sim, B.W., *et al.* "Flight Path Management and Control Methodology to Reduce Helicopter Blade-Vortex Interaction (BVI) Noise", *Journal of Aircraft*, Vol. 39, No. 2, 192-205, March-April, 2002.

[19]Schmitz, F.H., "Reduction of Blade-Vortex Interaction (BVI) Noise through X-Force Control", NASA TM-110371, April, 1995.

[20] Ishii, H., Gomi, H., Okuno, Y., "Helicopter Flight Tests for BVI Noise Measurement Using an Onboard External Microphone", presented at the American Institute of Aeronautics and Astronautics Flight Mechanics Conference and Exhibit, SanFrancisco, CA, August 2005.

[21] Chen H.N., *et al.*, "Study of the Aerodynamics and Acoustics of Super-BVI," 62nd Annual National Forum of the American Helicopter Society, Phoenix, AZ, May 9-11, 2006.

[22] Spiegel, P., Buchholz, H., Pott-Pollenske, M., "Highly Instrumented BO105 and EC135-FHS Aeroacoustic Flight Tests Including Maneuver Flights," presented at the American Helicopter Society 60th Annual Forum, Grapevine, TX, June 2005.

[23]Gopalan, G., Schmitz, F.H. and Sargent, D.C., "Q-SAM PRIME", unpublished report prepared September 2008.

[24] Hardesty, M. *et al.* "The Use of GPS Tracking and Guidance Systems for the Chicken Little Joint Project's 'Acoustic Week' Flight Test Program", presented at the American Helicopter Society 60th Annual Forum, Baltimore, MD, June 2004.

[25] Euler, L. "On de Lisle's Geographic Projection and its Use in the General Map of the Russian Empire", originally presented 1777, English translation provided by the Euler Archive: http://www.math.dartmouth.edu/~euler/docs/translations/E492.pdf Accessed on August 10th, 2008.

[26]Snyder, J.P. "Map Projections: A Working Manual", USGS Paper 1395, 1987.

[27] Sutherland, L.C., Bass, H.E., and Evans, L.B., "Atmospheric Absorption of Sound: Theoretical Predictions", *Journal of the Acoustical Society of America*, Vol. 51, Issue 5B, pp. 1565-1574, September 1971.

[28] Greenwood, E., Schmitz, F., Sim, B.W., Gopalan, G., "Helicopter Extenal Noise Radiation in Turning Flight: Theory and Experiment," presented at the American Helicopter Society 63rd Annual Forum, Virginia Beach, VA, May 2007.

[29] Schmitz, F. et al., "Measurement and Characterization of Helicopter Noise in Steady-State and Maneuvering Flight," presented at the American Helicopter Society 63rd Annual Forum, Virginia Beach, VA, May 2007.

[30] Sickenberger, R.D. and Schmitz, F.H., "An Optics- Based Tip- Path Plane Tracking System for Rotorcraft Applications" presented at the AIAA Guidance, Navigation and Control Conference and Exhibit, August 2008.

[31] Moralez III, E. , et al. "In-Flight Assessment of a Pursuit Guidance Display Format for Manually Flown Precision Instrument Approaches", presented at the American Helicopter Society 60th Annual Forum, Baltimore, MD, June 2004.

[32] Willshire Jr., W. "Model Scale Sound Propagation Experiement", NASA TM 100602, April 1988.

[33] Delany, M.E. and Bazley, E.N. "A note on the effect of ground absorption in the measurement of aircraft noise", *Journal of Sound and Vibration,* Vol. 16, Issue 3, pp. 315-322, June 1971.

[34] Jung, S.S. and Hwang, C.H. "A Complimentary to Determine the Effective Flow Resistivity of Flat Ground States", *Journal of the Korean Physical Society*, Vol. 44, Issue 4, pp. 868-874, April 2004.

[35] Bern, M., Eppstein, D., and Yao, F. "The Expected Extremes in Delaunay Triangulation", *International Journal of Computational Geometry and Applications*, Vol 510., pp. 674-685. 1991.

[36] Lattuada, R. and Raper, J. "Applications of 3D Delaunay Triangulation in Geoscientific Modeling", presented at the 3rd National Conference of GIS Research, UK. 1995.

[37] P. Alfeld, M. Neamtu, and L. L. Shumaker, "Bernstein-Bezier Polynomials on Spheres and Sphere-Like Surfaces", *Computer Aided Geometric Design*, Vol 13, pp. 333–349, 1996.

[38] Lyche,T. "Knot Removal for Parametric B-Spline Curves and Surfaces", *Computer Aided Geometric Design*, Vol 4., pp. 217-230, 1987.

[39] Mhaskar, H.N., Narcowich, F.J., and Ward, J.D. "Representing and Analyzing Scattered Data on Spheres", *Multivariate Approximation and Applications*, Cambridge Press, 2001.

[40] Laurent, P.J. and Anselone, P.N. "A General Method for the Construction of Interpolation Smoothing Spline-Functions*", Numerische Mathematik*, Vol 12, Issue 1, August 1968.

[41] Goovaerts, P. "Performance Comparison of Geostatistical Algorithms for Incorporating Elevation into the Mapping of Precipitation", presented at the 4th International Conference on GeoComputation, Fredericksburg, Virginia, July 1999.

[42] Fasshauer, G.E. and Schumaker, L.L. "Scattered Data Fitting on the Sphere", Mathematical Methods for Curves and Surfaces II, Vanderbilt University Press, 1998.

[43] Elman, H., Silvester, D., and Wathen, A. Finite Elements and Fast Iterative Solvers. Oxford University Press, New York, 2005. pp. 68-82, 166-193.

[44] Beatson, R.K., Cherrie, J.B. and Mouat, C.T."Fast Fitting of Radial Basis Functions: Methods Based of Preconditioned GMRES Iteration", <u>Advances in Computational Mathematics</u>, J.C. Baltzer, 1999. pp. 253-270.

[45] Brown, D. *et al.* "On Approximate Cardinal Preconditioning Methods for Solving PDEs with Radial Basis Functions", *Engineering Analysis with Boundary Elements*, Vol. 29, Issue 4., April 2005. pp. 343-353.

[46] Carr, J.C., *et al.* "Reconstruction and Representation of 3D Objects with Radial Basis Functions", presented at SIGGRAPH 2001, Los Angeles, CA, August 2001.

[47] Gopalan, G., Schmitz, F.H., and Sim, B.W., "Flight Path Management and Control Methodology to Reduce Helicopter Blade-Vortex Interaction (BVI) Noise", American Helicopter Society Vertical Lift Aircraft Design Conference, San Francisco, CA, January 2000.

[48] Prouty, R.W. <u>Helicopter Performance, Stability, and Control</u> Kreiger Publishing Co., Malabar, FL. 2005.

[49] Goff, J. A., and S. Gratch, "Low-pressure properties of water from -160 to 212 F", presented at the 52nd annual meeting of the American Society of Heating and Ventilating Engineers, New York, 1946.

[50] Morse, P.M. and Ingard, K.U. <u>Theoretical Acoustics,</u> Princeton University Press, Princeton, NJ. 1987.

[51] Dowling, A. "Convective Amplification of Real Simple Sources", *Journal of Fluid Mechanics*, Vol. 75, pp. 529-546. 1976.

[52] Mueller, A.W. and Preisser, J.S. "Flight Test of a Pure Tone Acoustic Source", NASA TP 1898, October 1981.

[53] Piet, J.F., Elias, G., and Lebigot, P. "Localization of Acoustic Source from a Landing Aircraft with a Microphone Array", 5th AIAA/CEAS Aeroacoustics Conference and Exhibit, Bellevue, WA, May 1999.

[54] Thomas, P. "Acoustic Interference by Reflection Application to the Sound Pressure Spectrum of Jets", NASA TT F-14185, 1972.

[55] Franken, P.A. and Bishop, D.E. "Propagation of Sound from Airport Ground Operations", NASA CR-767, 1967.

[56] Gopalan, G. and Schmitz, F. H., "A Sensitivity Analysis of the Quasi-Static Acoustic Mapping of Helicopter Blade-Vortex Interaction (BVI) Noise during Slowly Maneuvering Flight",9th AIAA/CEAS Aeroacoustics Conference, Hilton Head, SC, May 2003.

[57] Sim, B.W., *et al.,* "In-Flight Blade-Vortex Interaction (BVI) Noise Measurements Using a Boom-Mounted Microphone Array", presented at the American Helicopter Society 60th Annual Forum, Baltimore, MD, June 2004.